TÉCNICO LISBOA

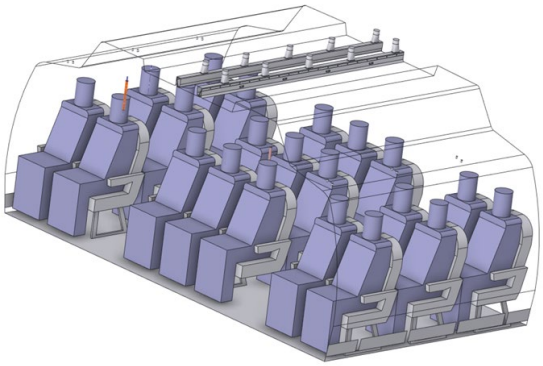

Bioaerosol Transport and Sensor in Passenger Aircraft

Carlos Miguel Loureiro dos Santos Simões Raposo

Thesis to obtain the Master of Science Degree in

Aerospace Engineering

Supervisor: Prof. João Manuel Melo de Sousa

Co-Supervisor: Prof. Taesung Kim

Examination Committee

Chairperson: Prof. Afzal Suleman

Supervisor: Prof. João Manuel Melo de Sousa

Member of the Committee: Prof. José Manuel Chaves Pereira

October 2022

This work is dedicated to all who believe in me

and all who support opening the boundaries to share scientific knowledge.

"If I have seen further it is by standing on the shoulders of Giants"

Sir Isaac Newton

Declaration

I declare that this document is an original work of my own authorship and that it fulfills all the requirements of the Code of Conduct and Good Practices of the Universidade de Lisboa.

Acknowledgements

Firstly, and foremost, I would like to thank my supervisor Professor João Melo de Sousa and his constant insightful feedback, motivation, patience as well as sharing knowledge and experience with me. He also helped me choose the topic, motivated me, and guided me to participate in ICAS conference and have a great experience.

I cannot stress enough how thankful I am for all the love, patience and financial support my family provided me with and the support and energy from my friends namely, my friend Catarina who continuously motivated me to pursue a researching career, my friend Pedro for our chilled times and my friend Jinju who supported and motivated me while I was in South Korea.

I would also like to thank my co-supervisor Professor Taesung Kim for inspiring me to study aerosol transport and the time I stayed in NPTL laboratory in SKKU.

I also would like to thank all researchers who were kind enough to read my e-mails and answer questions, namely Dr. Maher Shehadi, Prof. Byron Jones, and Dr. Seif Mahmoud.

I also would like to thank Raymond Horstman, P.E., for his help and comments in 3D modeling the cabin as well as tips on scaling pictures for engineering purposes.

And of course, I would like to thank the DEM department for providing ICALC workstations and IDMEC for funding my presence at the ICAS conference.

Resumo

Para ajudar a prevenir e mitigar a próxima pandemia, as cabines de avião devem ser continuadamente desenhadas para ventilar eficazmente qualquer contaminante dispersado no ar, e eventualmente detetar cedo um evento de contaminação de patógenos usando sensores de bioaerossóis. Uma simulação RANS, usando uma abordagem modificada k-ε e utilizando geometria do difusor detalhado, foi usada para simular o comportamento complexo dos jatos de ventilação, de uma forma mais precisa, e comparada com resultados experimentais. O modelo de turbulência realizável k-ε foi validado usando métodos quantitativos e qualitativos para metade da cabine.

Subsequentemente, um contaminante foi injetado no centro e no lado da cabine de 3 filas e no fim, conjugado com uso de *gaspers*. Resumidamente, se os *gaspers* estiverem normais às paredes, o efeito conjugado do vórtice de ar húmido com as plumas térmicas cria uma condição de ar estagnado, assim promovendo difusão e diminuindo dispersão. Finalmente, tanto para os *gaspers* ligados ou não, as localizações sugeridas para futuros sensores seria no teto, exatamente acima do passageiro, e na parte de trás do banco da frente.

Palavras-chave: Cabine de avião; dispersão de contaminantes; AVAC; simulação RANS; bioaerossóis.

Abstract

To aid the prevention and mitigation of the next pandemic, aircraft cabins must be continuously designed to ventilate effectively any contaminant dispersed in the air, and eventually allowing the early detection of an event of pathogen spreading using bioaerosol sensors. A RANS simulation, employing a modified k-ε approach and involving a detailed diffuser geometry, was used to accurately simulate the complex behavior of the ventilation jets and compare the results obtained with available experimental data. The modified realizable k-ε turbulence model was validated using quantitative and qualitative methods for a half-row cabin.

Subsequently, a contaminant was continuously injected into the center and side of the 3-row cabin, and ultimately conjugated with the use of gaspers. Briefly, it was found that, if gaspers are normal to the wall, the conjugated effect with the moist air flow vortex and thermal plume creates a condition of still air, thereby promoting diffusion and decreasing dispersion. Finally, either with gaspers turned on or off, the suggested locations for future sensors would be on the ceiling right above the passenger, and in the backseat surface of the front seat.

Keywords: aircraft cabin; contaminant dispersion; HVAC; RANS simulation; bioaerosols.

Contents

List of Figures

List of Tables

Nomenclature

Roman Characters

a	Speed of sound	$\mathrm{m/s}$
a_{th}	Coefficient to compute thermal conductivity	$\mathrm{W\,m^{-1}\,K^{1/2}}$
A_0	Constant to compute C_μ in realizable model	-
A_s	Variable to compute C_μ in realizable model	$\mathrm{s^2}$
b_{th}	Coefficient to compute thermal conductivity	K
B	Constant for gasper diameter calculation	-
B^*	Constant for gasper diameter calculation	$\mathrm{m^2/s}$
c_{th}	Coefficient to compute thermal conductivity	K
C_p	Specific heat capacity	$\mathrm{J\,kg^{-1}K^{-1}}$
C_1	Variable used in realizable ε-equation	-
C_2	Constant used in ε-equation	-
$\mathrm{C_{k2}}, \mathrm{C_{k3}}$	Constants used in k-equation	-
C_μ	Variable to compute turbulent viscosity	-
$\mathrm{C_{\varepsilon 1}}, \mathrm{C_{\varepsilon 2}}, \mathrm{C_{\varepsilon 3}},$	Constants used in ε-equation	-
d	Particle Diameter	$\mu\mathrm{m}$
d_{gasper}	Gasper diameter	mm
D_h	Hydraulic Diameter	mm
E	Energy	J
f	External force per unit volume acting on material volume	$\mathrm{Pa \cdot m^{-1}}$
g	Gravitational acceleration	$\mathrm{m/s^2}$
G_b	Source term in k-equation due to buoyancy	$\mathrm{Pa \cdot s^{-1}}$
G_k	Source term in k-equation due to mean velocity gradients	$\mathrm{Pa \cdot s^{-1}}$
h	Geometric altitude	m , ft
h_A	Airplane pressure altitude	$\mathrm{ft} \times 10^3$
h_C	Cabin pressure altitude	$\mathrm{ft} \times 10^3$
H	Geopotential altitude	m , ft
H_p	Pressure scale height	m
I	Unit tensor	-
J_i	Diffusion flux of species i	$\mathrm{kg\,m^{-2}\,s^{-1}}$
k	Turbulent kinetic energy	$\mathrm{m^2/s^2}$
k_B	Boltzmann Constant	$\mathrm{J/K}$
l	Mean free path	m
L_c	Characteristic Length	m
m	Mass	kg

$\dot{m}$	Mass flow rate	$\mathrm{lb/min}, \mathrm{kg/s}$
M	Mean Molecular Mass	$\mathrm{g/mol}$
N_a	Avogadro number	$\mathrm{mol^{-1}}$
n	Number density	$\mathrm{m^{-3}}$
p	Pressure	$\mathrm{Pa, or\ kPa}$
Pr	Prandtl number	-
Q	Volumetric Flow Rate	$\mathrm{L/s}, \mathrm{L/min}$
$\dot{Q}$	Rate of Heat	W
r	Earth radius	m
R	Specific gas constant	$\mathrm{J\ kg^{-1}K^{-1}}$
R_i	Net production of species i by chemical reaction	$\mathrm{kg\ m^{-3}\ s^{-1}}$
R_u	Universal Gas Constant	$\mathrm{J\ K^{-1}mol^{-1}}$
Re	Reynolds number	-
RH	Relative Humidity	$\%$
S	Sutherland empiric constant for air	K
S_i	Source term in species conservation equation	$\mathrm{kg\ m^{-3}\ s^{-1}}$
S_k	Source term in k-equation, user defined	$\mathrm{Pa \cdot s^{-1}}$
S_ε	Source term in ε -equation, user defined	$\mathrm{Pa \cdot s^{-2}}$
S_{ij}	Rate of strain (deformation) tensor	$\mathrm{s^{-1}}$
t	Time	s
t_i	Celsius temperature of ice point at mean sea level	$℃$
t_0	Celsius sea level temperature	$℃$
T	Temperature	$\mathrm{K\ or\ ℃}$
T_i	Temperature of ice point at mean sea level	K
T_0	Sea level temperature	K
TI	Turbulence intensity	$\%$
u_τ	Friction velocity	$\mathrm{m/s}$
u	Lateral velocity component	$\mathrm{m/s}$
$\vec{u}$	Velocity vector	$\mathrm{m/s}$
U	Velocity magnitude	$\mathrm{m/s}$
U^*	Variable to compute C_μ in realizable model	$\mathrm{s^{-1}}$
$U_{m,0}$	Average velocity at circular face of gasper	$\mathrm{m/s}$
v	Vertical velocity component	$\mathrm{m/s}$
$\bar{v}_p$	Mean particle speed	$\mathrm{m/s}$
V	Volume	$\mathrm{m^3}$
w	Longitudinal velocity component	$\mathrm{m/s}$
W	Variable to compute C_μ in realizable model	-
$\dot{W}$	Rate of Work	W

x	Lateral distance from center plane. Positive in the west side of cabin.	m
x-plane	Plane parallel to the cabin “symmetry” plane	-
X_i	Molar fraction of species i	-
y	Height from cabin floor. Positive above cabin floor.	m
y_P	the distance from the centroid of the wall-adjacent cell to the wall	m
y^+	Dimensionless distance from wall	-
y-plane	Plane parallel to the cabin floor	-
Y_M	Source term in k-equation due to compressibility	$\mathrm{Pa \cdot s^{-1}}$
Y_i	Mass fraction of species i	-
z	Longitudinal distance from south wall. Positive towards cabin north wall.	m
z-plane	Plane parallel to the cabin south wall	-
Z	Collision Frequency	$\mathrm{s^{-1}}$

Greek Characters

α	Thermal Diffusivity	$\mathrm{m^2/s}$
β	Temperature gradient	$\mathrm{K/m}$
β_s	Sutherland empiric constant for air	$\mathrm{kg/(m \cdot s \cdot K^{1/2})}$
γ	Specific weight	$\mathrm{N/m^3}$
δ_{ij}	Kronecker delta	-
Δt	Time step	s
ε	Dissipation rate of turbulent kinetic energy	$\mathrm{m^2/s^3}$
ϵ_{ijk}	Levi-Civita symbol	-
ζ	Bulk viscosity coefficient	$\mathrm{Pa \cdot s}$
η	Variable used to compute C_1	$\mathrm{s^{-2}}$
κ	Ratio of specific heats	-
λ	Thermal Conductivity	$\mathrm{W/(m \cdot K)}$
μ	Dynamic Viscosity	$\mathrm{Pa \cdot s}$
μ_t	Eddy Viscosity	$\mathrm{Pa \cdot s}$
ν	Kinematic viscosity	$\mathrm{m^2/s}$
ρ	Density	$\mathrm{kg/m^3}$
σ	Effective collision diameter of air molecule	m
σ_ε	Turbulence Prandtl number for dissipation rate	-
σ_k	Turbulence Prandtl number for turbulent kinetic energy	-
τ	Viscous or deviatoric stress tensor	Pa
τ_w	Wall-shear stress	Pa

T	Total stress tensor of fluids	Pa
ϕ	Field variable	-
φ	Variable to compute C_μ in realizable model	rad
ω	Specific turbulent dissipation rate	s^{-1}
Ω_{ij}	Rate of rotation tensor in a moving reference frame with angular velocity of ω_k	s^{-1}

Exponents and accents

$( )'$	Fluctuating component
$\overline{( )}$	Mean
$\dot{( )}$	Time derivative
$( )^T$	Transpose
$\overrightarrow{( )}$	Vector

Subscripts

$( )_0$	Standard sea level (SSL) condition
$( )_b$	Body or boundary
$( )_i$	i direction or species i
$( )_j$	j direction
$( )_k$	k direction
$( )_m$	Mixture
$( )_{x,y,z}$	Cartesian component x, y or z
$( )_{\mathrm{CV}}$	Control Volume
$( )_{CO_2}$	Carbon dioxide component
$( )_{He}$	Helium component
$( )_{\mathrm{MV}}$	Material Volume
$( )_{fresh}$	Fresh or outside air
$( )_{\mathrm{gasper}}$	Gasper location
$( )_{\mathrm{inlet}}$	Inlet location
$( )_{slot}$	Slot location
$( )_{total}$	Sum of fresh and recirculated air

Acronyms

ACER	Aircraft Cabin Environmental Research
ACH	Air Changes per Hour
ACRP	Airport Cooperative Research Program
ADSE	Aircraft Development and System Engineering
AERF	Aircraft Environment Research Facility
AMC	Air Mobility Command
APU	Auxiliary Power Unit
ASHRAE	American Society of Heating, Refrigerating and Air Conditioning Engineers
CAD	Computer Assisted Drawing
CATR	Centre for Air Travel Research
CFD	Computational Fluid Dynamics
CFM	Cubic feet per minute
CFR	Code of Federal Regulations
COTS	Commercial Off the Shelf
CSPs	Computer Simulated Persons
DEHS	Di-Ethyl-Hexyl-Sebacat
DES	Detached Eddy Simulation
DLR	German Aerospace Center
DNS	Direct Numerical Simulation
DTU	Technical University of Denmark
DUT	Dalian University of Technology
ECS	Environmental Control Systems
GCAQE	Global Cabin Air Quality Executive
HSA	Hot Sphere Anemometer
HVAC	Heating Ventilation and Air Conditioning
HWA	Hot Wire Anemometer
IBAC	Instantaneous Biological Analyzer and Collector
ICAO	International Civil Aviation Organization
IU	Illinois University
KSU	Kansas State University
LDA	Laser Doppler Anemometer
LES	Large Eddy Simulation
PAO	Personal Air Outlet
PBC	Periodic Boundary Conditions
PIV	Particle Image Velocimetry
PM	Particulate Matter
PRESTO!	Pressure Staggering Option

PU	Purdue University
NBS	National Bureau of Standards
NDIR	Non-dispersive Infrared
NRC	National Research Council
RANS	Reynolds Averaged Navier Stokes
RH	Relative Humidity
RNG	Renormalization Group
SARS	Severe Acute Respiratory Syndrome
SI	International System of units
SIMPLEC	Semi-Implicit Method for Pressure Linked Equations-Consistent
SSL	Standard Sea Level
SST	Shear Stress Transport
SU	Syracuse University
SVOCs	Semi volatile Organic Compounds
TCPs	Tricresyl Phosphates
TI	Turbulence Intensity
TJ	Tianjin University
TWA	Time Weighted Average
UA	Ultra-sonic Anemometer
UDF	User Defined Function
UFP	Ultrafine Particles
USTRANSCOM	United States Transportation Command
VE	Ventilation Effectiveness
VOC	Volatile Organic Compounds

1 Introduction

1.1 Motivation and Objectives

In the year of 2019, the world was hit with the COVID-19 pandemic caused by a coronavirus, later confirmed to be transmissible via aerosols. According to Our World in Data, by October of 2022 there were already 6.56 million of deaths and 624 million of cases. Multiple measures that affected the world were taken like lockdowns, social distancing, mask use, air travel restrictions which had an impact on the world economy and people's physical and psychological states.

The aviation industry was affected by these measures by having an overall reduction of 50% of seats in 2020 and 40% in 2021. In terms of gross passenger operating revenues, there was a loss of 372 billion dollars in 2020 and 324 billion dollars in 2021 [1]. There was a joint effort by the industry and regulators to earn the public trust and several studies and presentations were published [2]. In particular, USTRANSCOM published a report with high quality experimental data done in real airframes that could be used to further improve numerical simulation and its validation. However, the essential data to accurately simulate aircraft remains confidential like the geometry of the diffusers and the air conditions, which are essential because they will define the airflow behavior. This could lead to major limitations and errors in studies of independent researchers creating a gap between the manufacturers and independent researchers either from academia or institutions. In part, this is a safe measure to prevent leaking to public media conclusions that could alarm people unnecessarily, but transparency of data is the key to continue research.

The objective of this thesis is to find suitable locations for bioaerosol sensors inside the aircraft cabin of commercial flight. Therefore, first it was needed to study the airflow behavior using real diffuser geometry, secondly compare with available experimental data, thirdly study contaminants behavior and finally, the locations with higher concentrations would be candidates for bioaerosol sensors.

This thesis can be used for an introduction to the cabin air environment and cabin modeling. This first section focuses on briefly presenting how the cabin air environment works and the needed definitions. The literature review focuses on the previous work compiled in topics and experimental mockups available. The methods thoroughly present the 3D modeling and used computational methods. In September of 2022, a conference paper based on this thesis was presented [3].

To help continue research to be closer to the real aircraft, this study focused on studying the mockup of Boeing 767 in Kansas State University reported to have salvaged diffusers and stating all the steps and assumptions throughout the 3D modeling and choice of turbulence model. The files of the used 3D model will be made available at ResearchGate and researchers are welcome to use and modify them.

The cabin air conditions can vary with pressure and temperature so, on the appendix Air Properties Calculation, the equations to calculate the properties of dry air based on ICAO manual, NBS 564 and the new changes of SI 2019 are presented that can be used to improve the definition of materials in Computational Fluid Dynamics (CFD) software.

1.2 Airline Cabin environment

The airline cabin environment is a high density population enclosed environment which will suffer pressure changes due to climbing altitude.

The aircraft cabin of commercial airflight usually has cylindrical shape and needs to have a environmental control system (ECS) to allow necessary and comfortable conditions for its passengers. The ECS main functions are pressurizing the cabin, controlling thermal environment for human occupation, ventilate and control contaminants concentrations to allowed levels. During flight conditions, on almost every airplane, incoming air of the cabin can come from a compressor stage that is being bled for the air conditioning (bleed air) or, in the case of the Boeing 787, the air is electrically compressed separately. Figure 1-1 Shows the typical components from ECS of Boeing 767 [4].

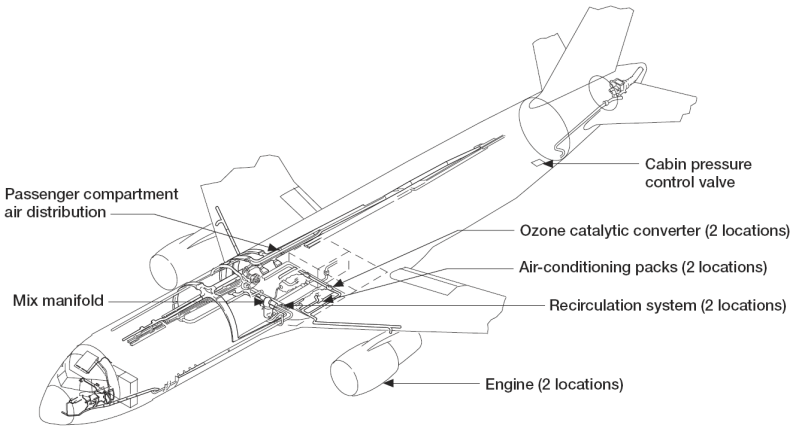

Figure 1-1. Typical components of ECS from Boeing 767 [4].

When in flight, the air path is as follows:

1. The outside low pressure, dry and cold air enters the engine where is compressed. The bleed port can be either at an intermediate stage or a high compressor stage which varies according to engine type. Air from the bleed system will provide all the pneumatic systems which include air conditioning packs, cabin ventilation system, pressurization of potable water, hydraulic reservoir, and cabin; anti-ice protection; cargo heat and air-driven hydraulic pump.
2. At cruise altitudes, ozone concentration from atmosphere is higher, so, to prevent ozone contamination, ozone catalytic converters are used in aircraft to dissociate into oxygen molecules, with a conversion ranging from 95% to 60% at end of life.
3. The air enters air-conditioning packs which are essentially an air cycle refrigeration system where the temperature is the predominant control driver for outside airflow requirements.
4. The air reaches the mix manifold where it is going to mix with a determined amount of recirculated air filtered through high-efficiency particulate air (HEPA) type filters.
5. Then, the air is separated into ducts exiting on overhead outlets distributed to each seating zone and added trim air, i.e., hot bleed air from the pneumatic manifold, to increase the temperature if needed.

6. After circulating in the cabin, the air exits through return air grilles and passes through HEPA filters to enter the mix manifold and the rest is exhausted overboard.

On the other hand, when the aircraft is on ground, pressurization is not required, however the ECS must maintain its function. The air that is supplied is either from ground-based systems available at many airports, which, if conditioned, is delivered directly to the mix manifold or when delivered at high pressure to the air conditioning packs. If the engines are not operating and there is no ground source, it is the auxiliary power unit (APU) which provides hot compressed air to the air conditioning packs [5].

Pressurization in the aircraft is necessary to achieve the partial pressure of oxygen necessary to support life. As the aircraft climbs altitude, the outside air pressure drops from 101 kPa to 17 kPa at 42000 ft altitude. To control the pressure, the cabin pressure control system opens or closes the cabin pressure outflow valve in the lower aft fuselage as needed to meet the airplane cabin altitude schedule predefined. In the appendix 8.3, it is shown the Boeing 767 pressure schedule. Furthermore, the ECS prevents rapid changes in cabin pressure that could cause discomfort to the human body. Moreover, for structural reasons the maximum pressure differential between inside and outside is 55-62 kPa [6].

There are several occupant hazards on the aircraft cabin environment. Related to cabin pressure: hypoxia can occur if there is not enough oxygen present in the blood; there can be ear discomfort due to the sensitivity of the human ear to large changes in pressure. Health problems can also arise from cabin contamination events which can come from several sources including the ECS or from physiological stressors such as fatigue, cramped seats and jet lag or exacerbation of pre-existing conditions for more sensitive people. Low relative humidity (RH) can also cause temporary discomfort symptoms, however, there is an upper limit to protect aircraft fuselage from water vapor condensation on structural elements and the only sources of water vapor are the people and equipment which can be reutilized within recirculated air. Therefore, to increase RH the aircraft needs an active humidification system or reducing the flow of outside air. [7]

Most of the concerns related to this environment are bleed air contamination events and transmission of airborne pathogens inside the aircraft. Regarding bleed air contamination, Michaelis [8,9] have been extensively investigating this subject and publishing results essentially showing that the use of bleed air with no sensors for contaminants or bleed air filtration should be discontinued. Scholz [10] alerts that the engineering assumption where the engine oils and hydraulic fluids operate in closed systems is wrong because systems wear out, seals do not fully prevent leaks and this is all explained by entropy law. As for the cabin air safety regarding pathogens, the cabin environment is often compared to indoor environments and apply the same criteria and statements usually optimistic are released such as: air as clean as hospital, air fully renewed every 2 to 3 minutes; air flows only from top to bottom; seats provide barrier for transmission; passengers that look forward have little facial contact; 6 ft physical distancing minimum without a mask is equivalent to 1 ft distance onboard the aircraft with a mask. These statements are refuted by Scholz in [11] finalizing that this matter is a political issue and for financial reasons flying is considered to be safe, however, we should adhere to moral principles.

1.3 Cabin airflow

The cabin airflow patterns will depend on several factors. The dominating factor will be the position of the air inlets which varies with each cabin design, as well as the design of the diffusers and air properties (flow rate, temperature, pressure). Other factors like the distribution of the passengers and seats, the windows positions, the type of overhead storage bin, and so on, will create either different thermal conditions or physical obstacles to the airflow which in turn influence the cabin pathlines. Figure 1-2 shows several airflow patterns of different cabin designs from several manufacturers references [12] [13] [14].

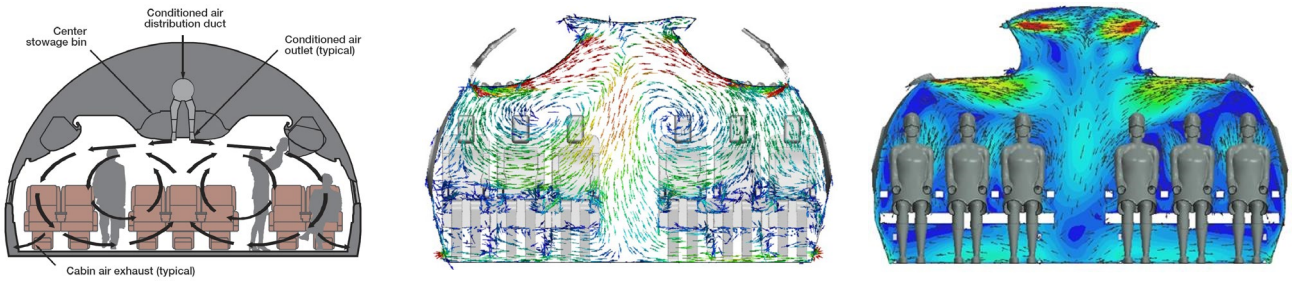

a) b) c)

Figure 1-2. a) Idealized airflow pattern in double aisle from Boeing [12]*, b) CFD airflow patterns of single aisle aircraft of Boeing* [13] *and c) Airbus model* [14].

To improve passenger thermal comfort inside the cabin, there are usually individual outlets available above each seat with an adjustable air supply nozzle known as “gasper” or personal airflow outlet (PAO) [5]. The distribution of the gaspers as well as their design and activation might be an important factor that affect the airflow patterns.

In an enclosed environment there are several mechanisms taking place: the jet flow from the supply air, the impingement, reattachment, separation, circulation and buoyancy [15]. Most indoor environments have mean air velocity usually in the order of 0.2 m/s which leads to low and transitional Reynolds numbers which complicate the airflow turbulence modeling.

Similarly to indoor environments there are different approaches that can be used to ventilate the cabin [16]. Mixing ventilation is the most common used system and the one present in Figure 1-2. This kind of system is designed to create a well-mixed environment by mixing the air from the cabin with new air from the diffusers, thus diluting contaminants throughout the cabin volume and keep the temperature uniform in the cabin. To achieve this, a mixture of outside air and recirculation air with different ratios, is injected from inlets, usually located either at the center of the cabin or near the windows. Then the air circulates through the influence of inertial and viscous forces which will compete with the buoyancy induced by the passenger’s thermal plumes and exit through grilles below the windows.

Other types of ventilation are under-floor displacement and personalized ventilation systems. On the former, the air is supplied vertically from the floor, through perforated or nozzles located near the aisle. This will allow the supply cooled air to heat as it climbs due to the thermal load surrounding the path which added to the thermal plumes from the passengers will create a stratification of temperature and the warm air will exit the outlets at the ceiling. In theory, this system would trap contaminants close to

the ceiling waiting for the new air to push them to the outlets. Furthermore, the supplied flow rate can be decreased due to improved ventilation efficiency. [17] On the latter system, there are multiple different strategies throughout the literature. The principle is to create a micro-environment around the passenger to prevent contaminants from entering. Usually on these systems the air is provided directly to the breathing zone, free from contaminants. Some proposed locations of the inlets are either at the seat armrest or the front seat-back. The main disadvantage of this system besides increasing complexity on the installation and design is the draft risk to the passengers. Figure 1-3 shows a comparison of airflow patterns in between the mentioned systems taken from [16].

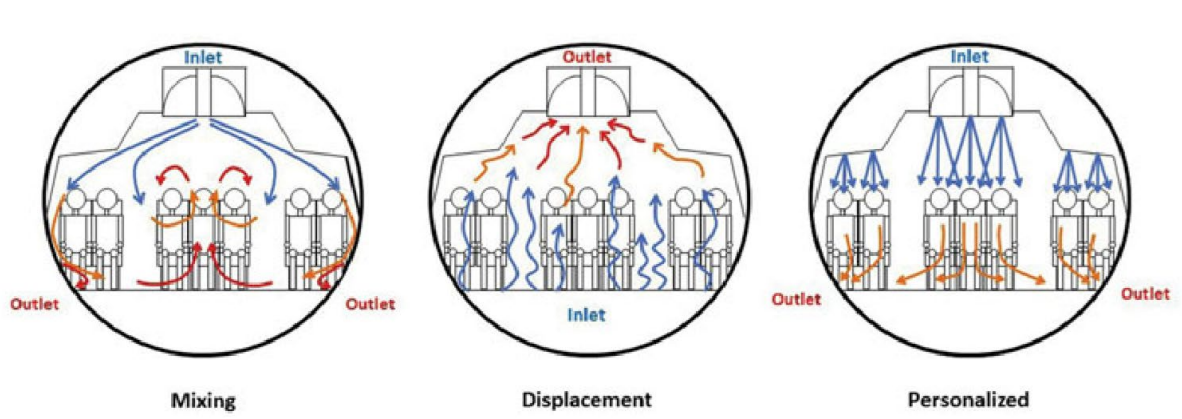

Figure 1-3. Different cabin ventilation mechanisms [16]

1.4 Aerosols and contaminants

Aerosols are two-phase systems consisting in suspension of solid or liquid particles in a gas, and manifest several phenomena such as smoke, fume, mist, fog, haze, clouds, dust.

Aerosols properties depend on particle size, allowing us to understand the physics they are subjected to: particle motion (including settling velocity and relaxation time), interaction between particles, such as Brownian motion and diffusion, coagulation, condensation, evaporation, bulk motion; thermal and radiometric forces, air resistance, electrical properties, optical properties. While gaseous contaminants concentrations are usually referred as mole fraction in parts per million (ppm) or parts per billion (ppb), aerosols concentration are measured in mass concentration expressed in $\mathrm{g/m^3}$ and number concentration being the number of particles per unit volume of aerosol expressed in $\mathrm{number/cm^3}$.

Depending on the properties and origins, we can divide aerosol into several categories: primary aerosols are introduced directly in the air, secondary aerosols are products of chemical reactions of gaseous components, homogenous aerosol where particles are all chemically identical, monodisperse aerosols where particles have same size, polydisperse aerosols have a distribution of particle size [18].

Contaminants are substances that cause discomfort and adverse health effects which can be either gas particles or respirable particulate matter (RPM) – solid/liquid particles with aerodynamic diameter $d < 10\ \mu\mathrm{m}$, including bioaerosols. Airborne contaminants can include carbon monoxide (CO); carbon dioxide (CO_2); ozone (O_3); volatile organic compounds (VOCs) (such as aldehydes; ketones; organophosphates;

carboxylic acids; alkenes, alkanes and aromatics; amines; esters); pyrethroid pesticides; flame retardants [7].

For this text context, there are several definitions worth mentioning as follows. Bioaerosols are aerosols from biological origin including viruses, bacteria, fungi, fungal spores, and pollen. Atmospheric aerosols are particles normally found in the atmosphere from natural or urban sources [18]. Particulate matter (PM) refers to suspended particles do not deform and droplets is when the particles are liquid and phenomena such as deformation, coalescence and breakup could occur [19]. Volatile Organic Compounds (VOCs), as stated by 40 CFR 51.100 [20], are any compounds of carbon excluding CO, CO_2, carbonic acid, metallic carbides or carbonates, ammonium carbonate, that participate in atmospheric photochemical reaction, even if these are determined to have negligible photochemical reactivity like methane and ethane. VOCs can be classified by their boiling points which define their volatility [21]. Very volatile (VVOC) with a boiling point range from 0°C to 50-100 °C , Volatile (VOC) with a range from 50-100°C to 240-260°C, and Semi-volatile (SVOC) with a range of 240-260°C to 380-400°C. Because VOCs can include hundreds of compounds, the concept of Total Volatile Organic Compounds (TVOC) involves measuring the sum of individual VOC concentrations. Particulate matter concentration, usually expressed in $\mu m/m^3$, can also be categorized by size: $PM_{2.5}$ are particles with $d < 2.5\ \mu m$ and PM_{10} are particles with $d < 10\ \mu m$.

As for the sources of these contaminants on the aircraft cabin we can account for bio sources, outside air and the airplane itself. Table 1 shows most sources of cabin air contamination based on ASHRAE Guideline 28 [7]. Cabin contamination can occur either in normal or abnormal operations. Several events can also be potential sources: when engine starts there can be emission of exhaust gases, short time increase of CO_2 after switching off bleed air, thermal degradation, cabin cleaning, traffic from aircraft and cars at the airport [22].

In the special case of bioaerosols, despite behaving physically as other aerosols, they can cause diseases depending on the organism, dose, immunity of the exposed people, durability (inside the person). The size of the particle will define the affected areas on the human body: 8-10 μm are mostly separated and retained by upper respiratory tract; submicron particles with $d < 0.1\ \mu m$ penetrate the lungs and may enter the bloodstream, whereas intermediate sizes deposit in the conducting airways of the lungs but are rapidly cleared or coughed out. Therefore, the main concern are particles smaller than $2\ \mu m$ [23].

1.5 Disease transmission

Throughout the history, there are several confirmed transmission of diseases during flight through several mechanisms [24]:

1. Contact transmission – direct body-to-body contact or indirect contact, i.e., when a person comes into contact with a contaminated intermediate host (fomites). Contact with large droplets ($d > 5\ \mu m$) expelled from contaminated people by talking, coughing, or sneezing are also

considered contact transmission. These droplets will travel shorter distances when expelled due to their inertia.

2. Airborne transmission – This kind of transmission is considered when the large droplets become aerosolized by evaporation containing residues from infectious agents forming the so called droplet nuclei. These are smaller particles which can remain suspended in the air following its pathlines which are greatly dependent on environmental conditions. Examples: Tuberculosis; SARS-CoV-1; SARS-CoV-2; Influenza; Measles.
3. Vehicle Transmission – In this case, it requires a vehicle like food or water to transmit the infection. Examples: food-borne diseases like salmonellosis; staphylococcus; food poisoning; shigellosis; cholera; viral enteritis.
4. Vector borne transmission – Finally, this transmission mode requires either insects or vermin which will spread the disease. Examples: Malaria; Dengue.

The most concerning for air travel are contact transmission by large droplets and airborne transmission through aerosols. Furthermore, it is important to keep the ventilation system operating at all times. While the use of recirculation air is not a primary concern, assuming HEPA filters are well maintained, if the ventilation systems are not operating the air is not being filtered nor renovated. There is evidence that there was an outbreak of influenza due to 3 hours of inoperative ventilation systems while repairs were being done [25].

In 2005, Mangili et al. [24] suggested that transmission inside the cabin is likely due to close proximity with a contagious passenger, i.e., within 2 rows. This is because, in principle, cabin airflow limits longitudinal transport. However, during SARS-CoV-1 outbreak, it was confirmed that people were contaminated seven rows ahead of the index passenger [26]. As for the SARS-CoV-2, most studies reported transmission in the same or within two rows from the index case [27].

To prevent infectious diseases outbreaks within air travel, we need to consider every stage and ideally passengers should postpone air travel when they are sick. One of the problems about airborne transmission is that diseases can have an incubation period up to 3 weeks which makes passengers asymptomatic (like SARS-CoV-2) and unaware of their condition, which also creates difficulties in pinpointing the location of spread and track patients thus, in-flight transmission is likely under reported – lack of evidence does not mean lack of transmission.

Air travel consists of every step from the entry of airport departure until the exit of the destination airport which involves the airport, baggage claim, transport to the airplane like buses or gates, restaurants, screening. Considering this, there was already a report available with mitigation recommendations for building, airplanes and people in the ACRP report of 2013 [28]. Besides cruise flight, there is the boarding, ascent, descent and deplaning, where the air quality is under-ventilated or even failing to meet regulations [29].

In case of SARS-CoV-2, it was shown that the virus remains infectious in bioaerosols for 3 hours and droplets deposited on surfaces (fomites) up to 72-hours on stainless steel and plastic and 84 hours on glass [30]. After imposing mask mandatory use, it was shown that the risk of being infected was

decreased (N95 could reduce infection by 85%), [27]. However, passengers need to take mask to eat, and it cannot be ensured that the use of mask is correct. The COVID-19 workshop reviewed what was done during the pandemic and addresses what should be done in the future [31]. Now it remains the question whether we will implement these measures in time.

	Sources									
Contaminants	**Fuel**	**Oil**	**Equipment Wear**	**Deicing Fluid**	**Hydraulic Fluid**	**Anticorrosion Coating**	**Galley**	**Occupants**	**Pesticides**	**Outside Air**
Carbon monoxide	X	X		X	X					
Carbon dioxide							X	X		
Ozone										X
Ultra-Fine PM	X	X	X		X		X			
$PM_{2.5}$		X	X		X			X		
PM_{10}			X					X		
Aldehydes	X	X			X	X		X		
Organophosphates		X			X				X	
Carboxylic acids		X				X				
Aromatics	X	X				X			X	
Alkanes	X	X			X	X			X	
Amines		X			X	X				
Ketones		X						X		
Esters		X			X					
Pyrethroids									X	
Alcohols	X			X				X		

Table 1. Contaminants of cabin air and their sources [7]

2 Literature Review

2.1 Previous work

This topic has been studied since a long time, and some authors in their studies include referenced material in tables to aid researchers with studies organized by several categories (numerical, experimental, cabin model, presence of manikins, studied data), namely: Shehadi [32] summarized the studies from Aircraft Cabin Environmental Research Laboratory (ACER) from Kansas State University (KSU) from 2001 to 2019; Liu et al. [33] gathered works from 1991 to 2010; Elmaghraby et al. [16] categorized studies from 1999 to 2016 and Li et al. [34] from 1997 to 2013.

Despite our continuous computing power increase, we still cannot use heavier turbulence models (LES; DNS) on industrial applications due to prohibitive costs. Non-intrusive visualization techniques are preferred in experimental measurements to not contaminate data, however, the inlet of the cabin, referred to as diffuser slot, keeps being the most difficult aspect in this research. Some authors, constructed mock-ups just with diffusers [35] to study closely how the flow behaves. Ideally, in CFD simulations, we would have the detailed diffuser geometry and its ductwork, but this would require having a real airplane in hand or disclose confidential manufacturer data. Therefore, the standard approach is to discover how much is the slot width and treat the diffuser geometry as a simple slot diffuser with a uniform velocity boundary condition by dividing the flow rate by the area.

Based on [36] the most reported facilities in the literature were gathered and added dimensions when these were available. Table 2 contains the outline of the facilities, more details can be found in the appendix on Table 32. Despite some of the mockups report to be a specific model, they can have different geometries, diffusers (including slot width), seat layouts, ventilation flow rates and temperatures, which creates difficulties to link the fields of computational and experimental fluid dynamics. The mockups of Boeing 767 from Kansas State University, Illinois University and Technical University of Denmark report to have real diffusers, i.e., taken from the aircraft Boeing 767.

Model	Institute		Resources
Boeing 737	Purdue University	PU-737	[37], [38] [39]
	Tianjin University	TJ1-737	[40] [41] [42] [43] [44], [45] [46]
	Tianjin University (2021)	TJ2-737	[36], [47] [48]
	Kansas State University	KSU-737	[49] [50] [51]
Boeing 767 *Real diffusers	**Kansas State University ***	KSU-767	[52], [53], [54], [51], [55]
	Illinois University *	IU-767	[56], [57], [58], [59], [60], [61], [62], [63]
	Technical University of Denmark *	DTU-767	[64] [65] [66] [67]
	Purdue University	PU-767	[68], [69], [70]
	Dalian University of Technology	DUT-767	[71]; [17]
Boeing 767 scaled	Purdue University	PU-767s	[72],[73]
Boeing 777	Syracuse University	SU-777	[74]
Boeing 747	Aircraft Environment Research Facility in CAMI	AERF-747	[75]. [76]
Airbus 310	FTF at Fraunhofer Institute	FTF-310	[77], [78], [79]
Airbus 320	German Aerospace Center (DLR)	DLR-320	[80], [81]
	Chongqing University	CU-320	[82], [83], [83]
Airbus 380	German Aerospace Center (DLR)	DLR-380	[84]
A380 section	German Aerospace Center (DLR)	DLR-380s	[85], [86]
MD-82	Tianjin University	TJ-MD82	[87], [88], [89], [90], [91]
Half Generic	Kansas State University	KSU-GEN	[92], [93], [94], [95], [96]
Other installations (new or owned by manufacturer)			
Generic	Flexible Cabin Laboratory at CATR	CATR-FCL	[97]
Generic	Modulares Kabinen Mock-Up Göttingen in (DLR)	DLR-MKG	[98]
Boeing 737	Fuselage Laboratory at CATR	CATR-FL	[97]
Boeing 787	Boeing Company	AIC-B787	[99]
Airbus 340	Airbus Company	A340	[72], [100]

AIC – Aircraft Integration Center. FTF – Flight Test Facility. CAMI – Civil Aerospace Medical Institute

Table 2. Facilities with different aircraft cabin mock-up.

2.1.1 Experimental Techniques for measuring aircraft cabin environment

In all experiments there are different challenges to address. In this case, measuring the conditions near the air inlet of the cabin is difficult because of the relatively small slot opening. Experimentalists try to use different methods to measure diffuser conditions, sometimes sacrificing accuracy.

There are several techniques in the industry that allow experimentalists to find results, each with different costs and advantages and disadvantages. Table 3 presents a summary of the available techniques based on review studies [33] and [16]. It is noted that particle velocimetry techniques are very expensive.

Sometimes multiple instruments are used due to their different accuracies and ranges. For example, in Zhang et al. (2008) [70] the diffuser of PU-767 has a slot opening of 25 mm, which is smaller than the

ultrasonic anemometer (UA) sensor span size. So, they used omni-directional hot-sphere anemometers (HSA) to measure velocity magnitude and used smoke visualization to estimate direction. The authors claimed that Laser Doppler Anemometers (LDA) would be an improvement, however, it would take months to complete.

Another example, in 2020, Wang et al. [45] used UA (0 – 10 $\mathrm{m/s}$) to determine the airflow direction from the slot and HSA (0.05 – 5 $\mathrm{m/s}$) to determine the velocity magnitude. In this case, to overcome UA large dimension which create physical constraints, the researchers used a very small thread to make sure the airflow direction does not change from the slot opening to the UA sensor location.

Measured Quantity	**Technique**
Direction and velocity	Particle Image Velocimetry (PIV),
	Particle Tracking Velocimetry (PTV),
	Volumetric Particle Tracking Velocimetry (VPTV)
	Volumetric Particle Streak Velocimetry (VPSV)
	Stereoscopic Particle Image Velocimetry (SPIV)
	Hot-Sphere Anemometer (HSA) Hot-Wire Anemometer (HWA),
	Ultrasonic Anemometer (UA)
	Lase Doppler Anemometer (LDA)
	Fog/Dye Flow Visualization,
Species Transport and concentration	Planar Laser-Induced Fluorescence (PLIF),
	Gas Chromatography,
	Photoacoustic Spectrometry
	Gas Direct Sampling,
Mass concentration	Mass Spectrometry, Proton-Transfer-Reaction Mass Spectrometry (PTR-MS)
Particle Distribution	Interferometric Mie Imaging (IMI), Optical Particle Counting (OPC),
Temperature	Thermocouples (TC), UA, infrared cameras

Table 3. Experimental Techniques.

For onboard experiments, in RP-1262, researchers prepared a carry-on bag with instruments. On pre-boarding they put the bags under the seats and placed the sampling lines in the appropriate locations to do the fixed measurements. To measure profiles throughout the cabin they used a small hand-held that could measure noise, air velocity, temperature. This equipment was treated as personal electronic devices and had electromagnetic emissions acceptable for flight use. Figure 2-1 shows the equipment deployed in one of the flights of the first part of the project [101].

Figure 2-1. Onboard deployed samplers for environmental measurements [101].

2.1.2 Numerical Techniques

Boundary Conditions

Domain

To study the aircraft environment, we need to decide the domain of interest. If longitudinal transport needs to be studied, more rows need to be studied. Ideally, we could model the entire cabin with its galleys and toilets and walls that enclose the cabin. However, resources need to be taken into consideration, so researchers modeled from 1-11 rows in CFD simulations as shown in Table 4. For this, usually in front and back cross section faces of the cabin periodic boundary conditions (PBC) can be considered to act as an infinite long domain or simple wall if there is a mockup available to later validate experimental data. PBC seems to be the best overall, however, compared to adiabatic wall needs to be further underrelaxed increasing the time to converge in steady state solution. [102]

Rows	Boundary Conditions at front and back faces		Reference	
1	Symmetrical		[96]	
2	Front face: $Q = 266.65\ \mathrm{L/s}$ $(w \approx 0.03\ \mathrm{m/s})$, Back face : Constant Outlet flow		[103]	
3	Wall		[67]	
4	Periodic	Walls	[104], [105]	[70]
5	Periodic	Walls	[106], [107]	[108],
7	Periodic		[109], [102]	
9	Periodic		[68], [69]	
11	Wall		[110], [73]	

Table 4. Examples of boundary conditions used at front and back faces of cabins.

To reduce computational domain, on the 2-row simulation Lin et al. [103] did not include the nozzle geometry, thus, the airflow at the interface between the nozzle and the 1-row model was used as an input for the simulation. However, longitudinal results in this study might not be realistic due to the simple condition at front and back faces.

Geometry Modeling

The aircraft cabin can be modeled with several degrees of complexity. Figure 2-2. Cabin Geometry Outline Considerations shows the outline of cabin geometry considerations to be made when modeling this problem. Regarding the 2D cross section, older cabins are more rectangular and newer cabins are more streamlined. For the main manufacturers, the recent cabin designs are Boeing Sky Interior[1] and Airbus Airspace[2].

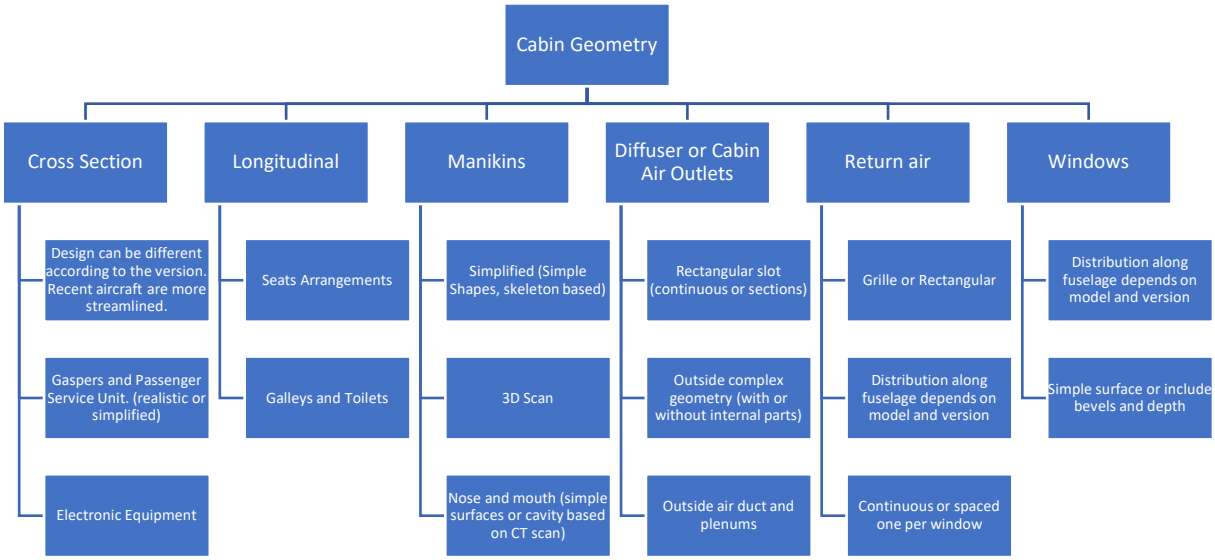

Figure 2-2. Cabin Geometry Outline Considerations

Researchers in literature should be more aware of the geometry modeling of the cabin. For the time being, to know the cabin geometry one can search on the manufacturer's website the cabin cross section in the airport planning manuals. However, these drawings are not fully accurate and do not specify the cabin air outlets geometry or accurate locations. So, one must be aware of the real mockup geometry and what 3D model was used for the numerical simulation in the literature. Furthermore, to better model the longitudinal geometry, the seat arrangement and the layout of galleys and toilets should be accurate. The seats are not always aligned in the same plane (parallel to the cabin cross section). These seat arrangements can also be found in the manuals, and they could be relevant if one wants to study the longitudinal spreading of aerosols.

Only few computational studies modeled a more detailed diffuser. Lin et al. [96] [103] modeled the cabin of Boeing 767 with manikins and the diffuser section without supply nozzles, however, they do not specify the used dimensions. Mazumdar [73] modeled the entire KSU-767 cabin including the diffusers,

[1] https://www.boeing.com/news/frontiers/archive/2009/june/i_ca01.pdf
[2] https://www.airbus.com/en/products-services/commercial-aircraft/cabin-and-comfort/welcome-to-airspace-cabin

supply nozzles, internal parts inside diffuser, and outside ducts. It is not clear if the dimensions of the diffuser slot are exactly the same and Mazumdar also did not put figures with dimensions in his work.

As for other cabin models, Liu et al. [88] measured the air velocity profiles of MD-82 real cabin diffusers using HSAs (Hot-Sphere Anemometers) and found that the profiles were highly non-uniform. Furthermore, in [87] the authors studied the effect of creating a division on the diffuser and compared between a cabin mockup (TJ1-737) and the MD-82, eventually, finding that the difference between the simplified diffuser (single row of slots) and the real cabin (double row of slots) had no significant effect on the airflow.

Mo's [49] studied the cabin air inside KSU-737 equipped with real ceiling diffusers detailed in Fig 6.2 and 6.3 (in [49]). For the numerical simulation, he used inlet velocity boundary condition at the supply duct, constant wall temperature for the manikins, heat flux for heaters and outflow for the flow outlets; additionally, the RNG k-ε model was used for turbulence closure. One of the main conclusions was that while the diffuser was designed to deliver uniform symmetrical velocity profile to the cabin, the CFD results showed otherwise.

Recent research has been developed about multi-slot diffusers. With ceiling and side wall diffusers, on TJ1-737, researchers [111] measured the isothermal air jets from the diffusers using 2D-PIV and concluded that jets went through transition from free jets to wall jets by the Coanda effect and the velocity profiles had a clear Reynolds number dependency. To reduce enhanced soiling effect on the multi-slot supply air nozzles, researchers [112] studied different plenums shapes and chose one that significantly reduce particle deposition and exhibited better supply velocity profile uniformity, less noise and pressure drop. Finally, while studying displacement ventilation, on the new TJ2-737, researchers [36] ensured uniform velocity profile by inserting fiber material with different thicknesses between the duct and cabin. It is unknown if manufacturers do similar procedure to guarantee uniform velocity distribution.

As for the manikin[3] modeling the geometry can be either simple or complex. When global flow conditions are the area of interest, like the global airflow pattern, contaminant distribution and temperature, manikins with simple geometry are sufficient according to Topp et al. [113] and Yan et al. [114]. Furthermore Yan W. et al. [114], using RNG k-ε with logarithmic wall functions with a heat source of $76\mathrm{W}$ and a convection to radiation ratio of 3:7, determined that there is no significant difference for the micro environment and to improve simple geometry results, care should be taken to distribute the heat source at different regions of the manikin. Later, Yan Y. et al [115] using RNG k-ε and uniform heat flux, compared 3 simplified manikins (3D scanned smoothed, skeleton reconstruction, simple solids), with one detailed (3D scanned) and PIV experimental data. They agreed with previous literature about global conditions, however, they showed that the microenvironment is highly sensitive to the geometry of the manikins and the manikin with simple solids generates a significant convective boundary layer.

[3] Also known as Computer Simulated Person (CSP), Computational Thermal Manikin (CTM), in silico human model.

Additionally, the authors hypothesized that the inaccuracy of the airflow field prediction could cause significant errors for contaminant transport when released from the manikin.

Another example can be found in Li et al. [116] that studied the airflow around a non-uniform temperature manikin using 2D PIV system and provided the file for the 3D Scanned model. In their results, they found the convective boundary layer with average thicknesses of 0.042 m in front and 0.033 m in the back. Figure 2-3 and Figure 2-4 show examples of a simple and complex manikin.

Further advancements in thermal comfort have been developed. Murota et al. [117] added 3D scanned clothes on a manikin, including the gap between clothes and the manikin and performed a hygro-thermo-chemical transfer analysis. The manikin temperature was calculated with thermoregulation Fanger's 1-node model [118] and used a Low Reynolds k-ε for turbulence modeling.

Kuga et al. [119] integrated a nasal cavity scanned using computer tomography in a realistic manikin (standing, sitting and lied down) and analyzed the airflow and temperature field, breathing zone under steady inhalation and transient breathing, microgravity effect, re-inhalation ratio. The authors proposed new definitions on the breathing zone for the standing position.

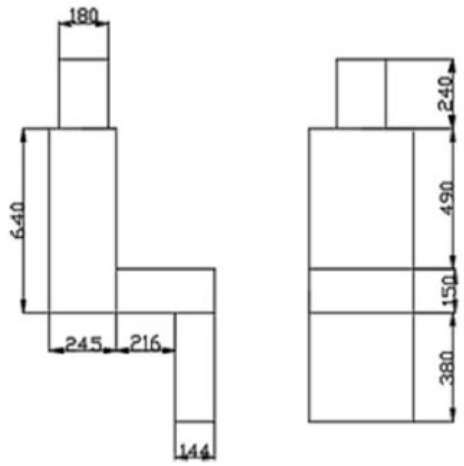

Figure 2-3. Manikin with constant temperature from [36]*. Dimensions in millimeters.*

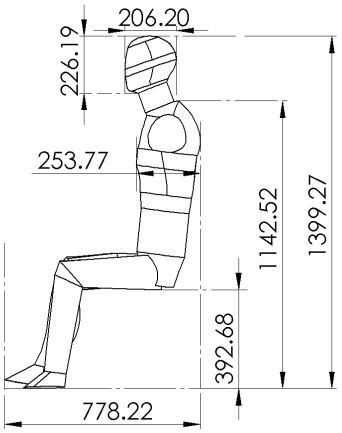

Figure 2-4. 3D Scanned Manikin used in [116] *Dimensions in millimeters.*

Inlet

The flow is dominated by the inlet boundary condition. The official name for our inlet diffuser boundary condition is *cabin overhead air outlets* while the cabin outlets are called exhaust or *return air grilles.*

Regrettably, some authors in the literature do not specify the full used boundary conditions and care should be taken because the values will vary depending on air pressure and temperature. Appendix 8.3 Air Properties Calculation can be used to aid the conversion of air properties. For example, the minimum volumetric flow rate of outside air depending on conditions is shown in Table 31.

In Lin et al. 2005 study [96], it can be seen a cross section from the nozzle section airflow, presented in Figure 2-5 taken from [74]. For this diffuser before the 1.27 mm gap, the airflow is approximately symmetric however afterwards it is not. This type of diffuser geometry is based on the B767 and was used further by the Kansas State University (KSU-767) mockup cabin in experimental measurements.

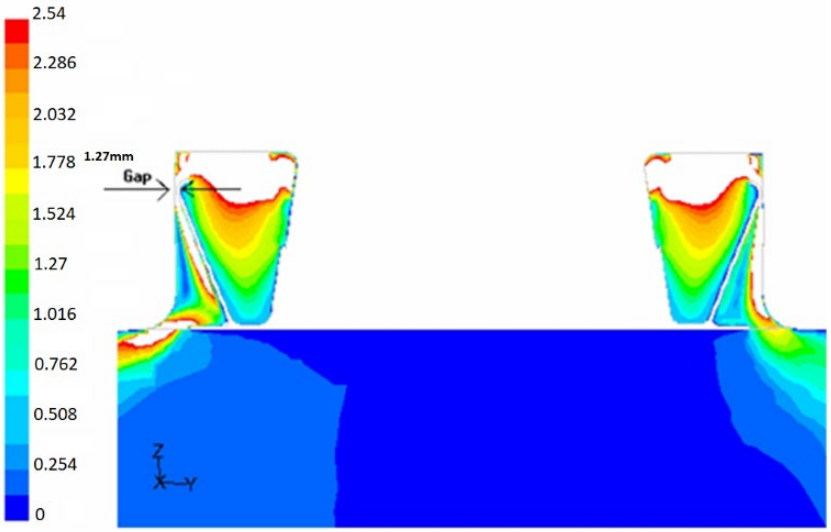

Figure 2-5. Boeing 767 nozzle section velocity distribution in meters per second [74].

In 2009, Mazumdar's thesis [73] used an accurate 3D model of the KSU-767 and its diffusers plus internal parts: spacer buttons and wall connectors, as shown in Figure 2-6 extracted from his work. He concluded the airflow inside the diffuser is governed by the location of the connecting tubes (supply nozzles). Then the spacer buttons and wall connectors will break the jet creating stagnation points in their locations. This internal diffuser geometry will create strong localized longitudinal velocities (1.5 $\mathrm{m/s}$) which are important for aerosol transport, while the measured longitudinal velocity of the diffuser jet overall mean is 0.05 $\mathrm{m/s}$. Furthermore, the diffuser with internal parts had a maximum velocity reaching 7 $\mathrm{m/s}$ against the maximum of 5 $\mathrm{m/s}$ without internal parts. Figure 2-7 shows the velocity profiles in the vertical and longitudinal directions comparing the RANS RNG k-ε CFD results with the experiments, based on the graphs from Mazumdar's thesis. These experimental points were collected using HWA near the centerline of the supply inlets. Moreover, for the diffuser area, the minimum mesh size was 2.5 mm while the cabin maximum mesh size was 50 mm making a total of 10.4 million elements for the 11-row and used standard wall functions for near wall treatment on Fluent software.

In contrast, Zhang et al., [70] used simple uniform boundary condition and concluded that when compared with experiments, the RANS RNG k-ε CFD results do not agree quantitively. CFD results predicted a strong downward movement in the left section and near the right ceiling that was not present in the experiment with the PU-767 mockup. These discrepancies can be seen in Figure 2-8. The authors concluded that the numerical simulation is highly sensitive to the accuracy of the boundary conditions.

However, uniform boundary condition at the inlet can be assumed if procedures in the real mockup are taken in the TJ2-737 mockup, Liu et al. [36], inserted fiber material with different thickness to each

diffuser across the length to ensure uniform air velocity and were able to have $0.64\ \mathrm{m/s}$ mean supply velocity with less than $0.1\ \mathrm{m/s}$ standard deviation.

In summary, for the diffuser boundary condition, we can divide the levels of complexity as shown in Table 5. Furthermore, the supply airflow rate can be steady or unsteady, using a periodic flow rate of ON and OFF cycles. This kind of behavior was studied by Wu et al. [120][121] and they concluded that this can have the same benefits as increasing the airflow rate by 10% with improvements shown on distributions of CO_2, temperature and mean age of air.

Level	Description
1	Simple Rectangle with the same area as the diffuser would have, uniform airflow velocity
2	Simulate the main diffuser geometry by specifying the inlet in the connecting tubes (supply nozzles)
3	Include internal details of the geometry like spacing buttons and joints between diffusers
Supply Flow	Steady or Periodic

Table 5. Complexity levels of inlet boundary conditions.

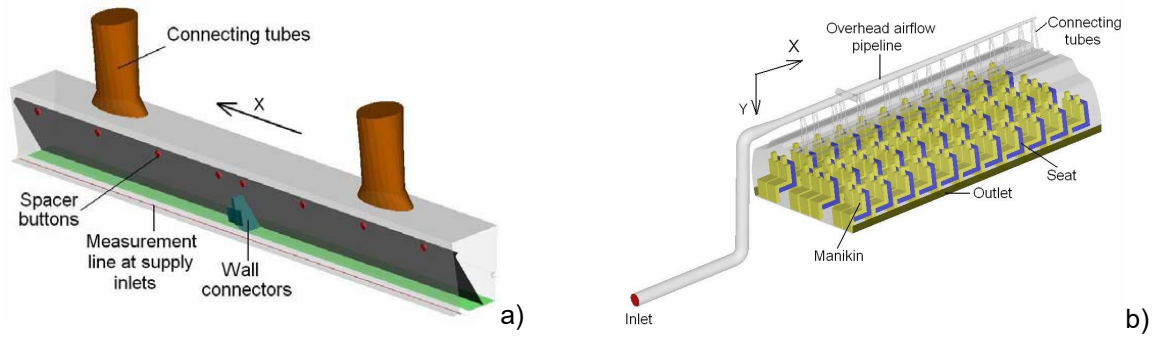

Figure 2-6. a) 3D model of diffuser and internal components, b) 11-row 3D model with ducts [73]

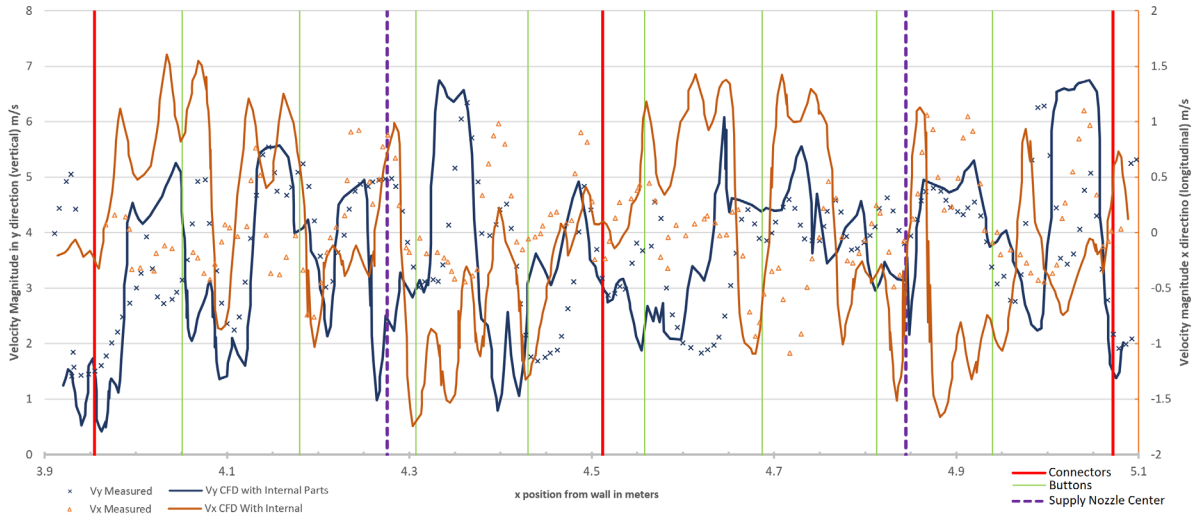

Figure 2-7. Velocity profiles of diffuser with internal geometry with CFD vs. experiment based on literature [73].

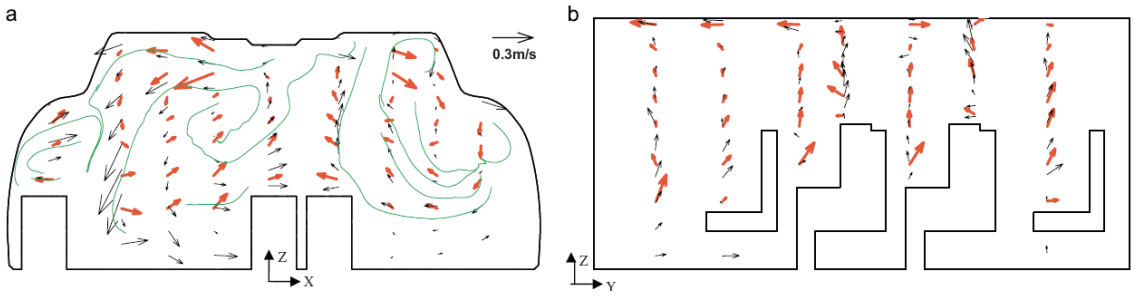

Figure 2-8. Comparison between CFD (black) and experimental results (red). Green lines is the computed airflow path [70].

Turbulence Models

In 2005, Lin et al. [96] [103] numerically simulated with a modified RANS k-ε model and LES the flow field of a 1-row Boeing 767 cabin model[4] and compared it with experimental data from a simplified cabin. Figure 2-9 shows the steady state flow field of the cabin, even though the geometry and boundary conditions are symmetrical, the inherent unsteadiness of this type of flow results in asymmetrical airflow. The LES half cabin model (KSU-GEN) (Width, Height, Length = 2.134 m) [5] was made by rectangular blocks and used for simulation and measurements because the curvature could add uncontrolled instability and further numerical approximations and wall functions changes. In this simplified cabin it was assumed an inlet of 53.34 mm with a velocity magnitude of 0.6096 $\mathrm{m/s}$ and a time step $\Delta t = 0.05$ seconds.

[4] The supply nozzle geometry dimensions are not revealed. From the Reynolds 31417 the nozzle diameter would be 31.94 mm diameter which is about half the KSU supply nozzle.
[5] KSU-GEN Geometry details can be found in [94] [95].

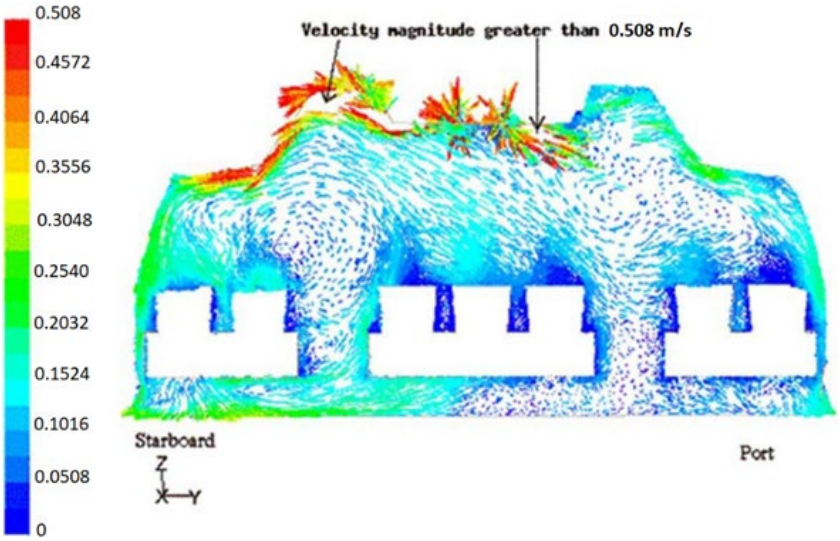

Figure 2-9. Boeing 767 Steady-state velocity flow field in meters per second [74].

Regarding the accuracy of the turbulence models, the authors concluded that RANS standard k-ε model underpredicted the turbulence intensity by eight times, when compared with LES and experimental measurement $k_{LES} > 8\, k_{RANS}$, and velocities by 35.5%, especially around the breathing area because the movement of large eddies of the cabin would not be resolved. According to the authors this would make RANS unable to accurately predict disease spreading because turbulent fluctuations are an important factor in particle dynamics. Therefore, they decide to adjust the RANS model by doing a subroutine and adding a new constant $C_{k2} = 0.77$ to reduce the negative source strength of dissipation in the k-equation and increasing $\sigma_\varepsilon = 1.67$ to enhance the dissipation in the ε-equation[6], while maintaining the overall effective viscosity. To implement these adjustments, they plotted $|\overline{U}|_{RANS}$ against $|\overline{U}|_{LES} \pm |u'|_{LES}$ and realized in the steady-state simulation, especially for lower speeds ($|\overline{U}| < 0.254$ m/s), the velocities fluctuations $|u'|_{LES}$ ranged from 30% to 200% from their counterpart $|\overline{U}|_{RANS}$.

Zhai et al. (2007) [15] [122] compared experimental and computational results from several turbulence models for predicting airflows in different enclosed environments: natural convection in a tall cavity (A); forced convection in a room with partitions (B) ($\mathrm{Re}_{\mathrm{inlet}} = 4000$), mixed convection in a square cavity (C) ($\mathrm{Re}_{\mathrm{inlet}} = 684$), and strong buoyant flow in a fire room (D) . For this dissertation, the forced convection case is the most similar scenario, where all the turbulence models predicted well the jet flow near the ceiling ($TI = 1.6\%$). In summary:

- The standard k-ε has been widely used in indoor air applications providing acceptable results with good computational-accuracy balance. However, it should not be used for high buoyancy effects or large temperature gradients.
- The RNG k-ε was the best overall model for the 4 cases. It underpredicted the fluctuating velocity in the lower part of the room in case D and the overall production of kinetic energy in case A.

---

[6] k – equation: $\rho u \frac{\partial k}{\partial x} + \rho v \frac{\partial k}{\partial y} = \frac{\partial}{\partial x}\left[\left(\mu + \frac{\mu_t}{\sigma_k}\right)\frac{\partial k}{\partial x}\right] + \frac{\partial}{\partial y}\left[\left(\mu + \frac{\mu_t}{\sigma_k}\right)\frac{\partial k}{\partial y}\right] + \mu_t\left[2\left(\frac{\partial u}{\partial x}\right)^2 + 2\left(\frac{\partial v}{\partial y}\right)^2 + \left(\frac{\partial u}{\partial x} + \frac{\partial v}{\partial y}\right)^2\right] - C_{k2}\,\rho\,\varepsilon$

ε – equation: $\rho u \frac{\partial \varepsilon}{\partial x} + \rho v \frac{\partial \varepsilon}{\partial y} = \frac{\partial}{\partial x}\left[\left(\mu + \frac{\mu_t}{\sigma_\varepsilon}\right)\frac{\partial \varepsilon}{\partial x}\right] + \frac{\partial}{\partial y}\left[\left(\mu + \frac{\mu_t}{\sigma_\varepsilon}\right)\frac{\partial \varepsilon}{\partial y}\right] + C_{\varepsilon 1}\,\mu_t\,\frac{\varepsilon}{k}\left[2\left(\frac{\partial u}{\partial x}\right)^2 + 2\left(\frac{\partial v}{\partial y}\right)^2 + \left(\frac{\partial u}{\partial x} + \frac{\partial v}{\partial y}\right)^2\right] - C_{\varepsilon 2}\,\rho\,\frac{\varepsilon^2}{k}$

- The SST k-ω model has predicted a reversed velocity profile leading to wrong circulations in case B, exhibiting problems for low turbulence flows. Modifying the blending functions could improve the accuracy because even outside the wall area, the model worked as a k-ω model.
- The v2f-dav model performed even better than RNG k-ε, however, requires more computing time.
- LES-Dyn provides more accurate results, but it requires large resources, and the accuracy is not always the best.
- DES-SA provides poorer accuracy than LES for the same computational grid and does not save computing time.

Zhang et al. (2013) [123] evaluated the performance of RNG k-ε with standard wall functions in 3 different ventilation modes (mixing, displacement and personal) inside a B767 cabin while comparing with experimental data from DUT-767. The diffusers were modeled as simple slots imposing uniform velocity in the surfaces. CO_2 is modeled as a discrete species with an Eulerian approach and solved after the flow and temperature variables are frozen. The turbulence model is found to underestimate significantly the turbulent mixing, as pointed out by Lin et al. [96]. The combined effect of low velocities and high levels of turbulence, and the effects of forced convection with natural convection may characterize a flow outside of the capabilities of steady RANS models. The authors pointed out that it was difficult to accurately model the boundary conditions near the slot diffusers. Despite this, the model predicted well the temperature and tracer gas concentration profiles for the displacement mode and the near-body flow along with the temperature distribution of the personal model.

Further advancements on turbulence modeling allow researchers to create new models to overcome the limitations of standard ones. You et al. (2017) [38] developed a hybrid RANS model to use standard k-ω near the wall and RNG k-ε far from the wall using a blending function to gradually switch according to the region. This model was validated using experimental data from PU-737 and TJ-MD82 and performed better than RNG k-ε while being similar to SST k-ω.

On a recent study Cao et al. (2022) [48] compared experimental data from TJ2-737 mockup with displacement ventilation against the performance of several RANS models with Enhanced Wall Treatment. Between the standard k-ε, realizable k-ε, RNG k-ε and SST k-ω models, it was the realizable model that provided overall best results.

Multiphase particle modeling

There are two main approaches that may be followed to model particle transport. We can consider the Lagrangian approach, where particles are individually tracked and added to the fluid. In the Eulerian approach, the particles are modeled as a scalar where their concentration satisfies the diffusion equation with a Fickian diffusivity. Each of these approaches has different equations to manage numerically. On the Lagrangian approach the details of the carrier medium, or continuous phase, will determine the drag, lift and other forces which could significantly change their trajectory, whereas for the Eulerian approach, these effects will be neglected and provide a statistical averaged information like particle velocity and concentration field. In terms of equations, the Lagrangian method uses Newton second law of motion to

apply a force balance on the particle. To link Eulerian particle phase with fluid phase models can be used, like the mixture, Volume of Fluid, and two-fluid Eulerian-Eulerian model [19].

There are three ways to computationally link the equations: one-way coupling (Eulerian-Lagrangian) where fluid properties are passed as forces in the particle equation; two-way coupling (Eulerian-Lagrangian) where besides the former treatment, the particles properties are additional sources terms in the fluids equations and full coupling (Eulerian-Eulerian) where fluid and particle equations are coupled by the influence of different flow phases on each other and the volume fraction – the amount of occupied space of each phase [19].

In terms of advantages, the Eulerian approach is computationally more economical and able to manage both dilute and dense flows, whereas the Lagrangian has results of individual particle details like locations, residence time and deposition while able to handle different particle sizes and properties. As for the disadvantages, in Eulerian these different particle sizes would be treated as different phases and interaction between each phase is difficult to adjust, while for Lagrangian, turbulence dispersion is idealized and not practical for large discrete phase volume fractions [19].

Chen et al. (2005) [104] compared both of these approaches on an environmental chamber with experimental results available and concluded that the Lagrangian approach is more useful for multiple scale studies and track every particle while Eulerian method only gives concentration information and uses an empirical diffusion coefficient. However, both can predict particle distribution with reasonable accuracy.

2.1.3 Experimental work by KSU

In order to compare data with an airframe experiment, there is a need to accurately model the airflow. The KSU mock-up cabin can be used to directly compare because it has real salvaged parts of the diffuser from Boeing 767. A summarized review of studies of ACER laboratory can be found in [32].

Beneke (2010) [55] studied small diameter particle dispersion of talcum showing that regions close to the source had a high level of exposure. In a similar experiment, Shehadi (2010) [53] investigated optimal particulate sensor locations in the cabin. On the other hand, Trupka (2011) [124] studied the impact of a beverage cart on contaminant dispersion. Anderson (2012) [52] studied the effect of gaspers using tracer gas on the cabin and used a more advanced thermal manikin.

Ebrahimi (2012) [93] employed Large Eddy Simulation (LES) to study the airflow and tracer gas and particle dispersion on a generic cabin (KSU-GEN), moreover used RNG k-ε in the simulation of the 11-row cabin by adjusting turbulence parameters at the diffuser slot, modeled as a rectangular opening with uniform velocity boundary condition. Using a tracer gas, Madden (2015) [125] experimentally studied the effects of passenger (full or half) loading and ventilation air (on or off) on KSU-767. On other hand, Patel (2017) [50] studied the ventilation effectiveness in KSU-767 and KSU-737, by supplying CO_2 upstream the diffusers, and the dispersion of tracer gas (mixture of CO_2 and He) inside KSU-737 with ventilation ON and OFF.

In another study, using smoke visualization, Shehadi (2015) [126] proposed flow patterns inside the cabin that indicated three large vortices along the cabin, namely one in the aft section, one to the middle section and one at the forward section, and studied experimentally the airflow distribution and turbulence in the longitudinal direction [127] [128]. Details are given below:

- Flow visualization by smoke – smoke injected at a height from the cabin floor $y = 1.10$ m in 18 different locations was captured by camera using a laser sheet at $y = 1.23$ m.
- Tracer gas results – a mixture of 7.1 L/min of CO_2 and He was injected at $y = 1.25$ m by a 25.4 mm diameter copper tube. The CO_2 was measured using a sampling tree connected to Non-dispersive infrared (NDIR) or Edinburgh Gascard sensors at $y = 1.23$ m. The tracer gas was released at 8 different locations and sampled 3 rows in front and 3 rows to the back.
- Airflow speed results – measured using HSA at a height of $y = 1.23$ m in seats B, D and F with heated and unheated manikins. Moreover, they allowed to analyze the turbulent kinetic energy (k) and turbulence intensity (TI) inside the cabin mockup. It was concluded the east side had higher k and TI in the front section than the center and west side. The integral length scale was determined to be 2.1 m, while the Kolmogorov length 1.05 mm.
- Figure 2-10 shows the path lines of flow behavior using different methods.
- The time to achieve steady state conditions on the cabin is estimated to be 300 seconds.

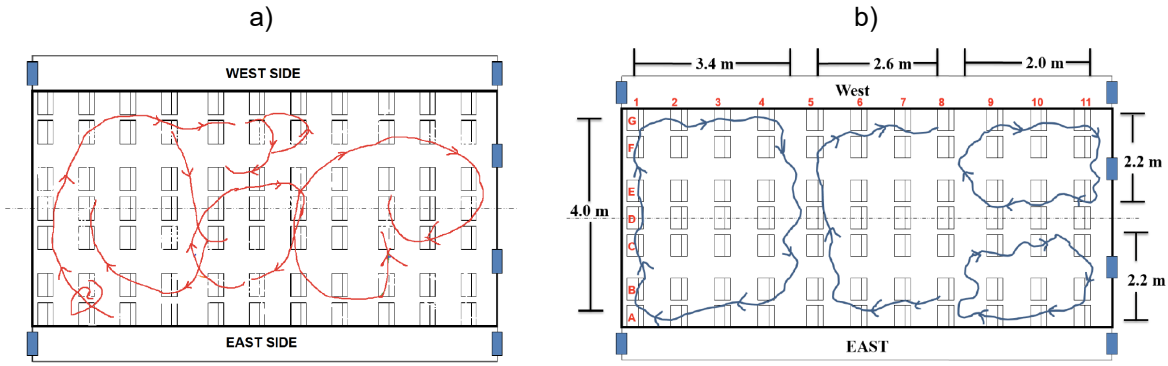

Figure 2-10. Proposed flow behavior of KSU-767 based on a) smoke visualization, b) tracer gas method [127].

These asymmetrical trajectories of the flow in the cabin were further explored by Keshavarz [129] with an added supplementary fan. Later on, an expedient passenger isolation system (ISOPass) was developed and found to be highly effective when deployed [130] [131]. Finally, Mahmoud [51] also studied experimentally aerosol dispersion using tracer gas in several situations, i.e. continuous injection point source, and a coughing manikin, both with ISOPass deployed and undeployed, in the B737 mockup, the B767 mockup and the same B767 mockup using a different ventilation system more alike to airbus cabins.

Table 6 shows a summary of tracer gas studies conditions using KSU-767. The height is from the cabin floor.

Reference	Q_{CO_2} (L/min)	Q_{He} (L/min)	Q_{total} (L/min)	Injection Height (m)	Sampled Height (m)
Mazumdar [73]	7.1	0	7.100	1.2192	1.5240
Trupka [124]	7.0	4.22	11.22	0.7900	1.2195
Anderson [52]	7.5	4.50	12.00	1.2070	1.2070
Madden [125]	7.0	4.21	11.21	1.2000	1.2195
Shehadi [126]	7.1	4.28	11.38	1.2500	1.2300
Patel [50]	15.0	0	15.0	Supply Air	1.0795
Mahmoud [51]	5.00	3.07	8.07	1.2500	1.2500

Table 6. Tracer Gas Experimental Studies using KSU-767.

2.2 Cabin air environment

2.2.1 Regulations

There are several regulations laws that can be examined. Here it is summarized the ventilation laws contained in the Code of Federal Regulations CFR 25.831 and CFR 25.841 [132]. It is stated that, "*Under normal operating conditions and in the event of any probable failure conditions of any system which would adversely affect the ventilating air, the ventilation system* ***must be designed to provide a sufficient amount of uncontaminated air*** *to enable the crewmembers to perform their duties without undue discomfort or fatigue* ***and to provide reasonable passenger comfort.*** *For normal operating conditions, the ventilation system must be designed to provide each occupant with an airflow containing at least 0.55 pounds of fresh air per minute*."

	14 CFR Regulations	***ASHRAE 161-2018***
Ventilation	Minimum of 0.55 lb/min (≈ 0.249 kg/min) of **fresh air** per person **Fresh Air** volumetric flow conversion: SSL 3.512 L/s Cabin altitude=8000ft 4.728 L/s	Minimum of 3.5 L/s of **outside air** per person if VE ≥ 1, Minimum of 7.1 L/s of **total air** per person
Cabin Pressure	Not more than 8000 ft (≥75.3 kPa) at maximum operating altitude	Same as CFR 25.841
Carbon monoxide *concentration*	50 ppm	9 ppm TWA 10 min 50 ppm 1-min peak
Carbon dioxide *concentration*	5000 ppm (SSL)	-
Ozone *Concentration*	100 ppb TWA 3h > FL270 250 ppb any time > FL320	100 ppb TWA 3h 250 ppb any time

Table 7. Cabin Air Regulations Summary [132] [5]

Table 7 shows the summary of CFR regulations and the corresponding ASHRAE 161 [5]. On the table SSL is Standard Sea level equivalent conditions which are 25 °C (298.15 K) and 760 mm Hg of pressure (101325 Pa), TWA is time weighted average, VE as stated in the standard is ventilation effectiveness

defined as the fraction of the outside air delivered to the space that reaches the breathing zone. In addition, ASHRAE 161 standard presents requirements for cabin temperature, local air speed, temperature spatial variations, maximum surface temperature differential for seated occupants and galleys, adjacent to doors. At the time being, CFR regulations still do not regulate the cabin temperature range.

The air recirculation ratio and number of air exchanges per hour can be inspected for several aircraft models in table 2-1, page 48 in [6], being the most common 50 % of outside air and 50 % recirculation air. This would mean that for SSL conditions, the total air per passenger according to CFR 25.831 is 7.024 L/s.

In the appendix 8.3 Air Properties Calculation, the air properties and conversions of mass flow rate to volumetric flow rate are presented.

2.2.2 Air Quality and comfort of cabin air

In 2021, Chen et al. [133] [134] published a review article regarding cabin air quality. They analyzed the different standards in the industry for aircraft as well as general indoor environment air quality, and summarized data regarding contaminants data and air properties measurement such as temperature, relative humidity, and ventilation rate. Using the information available, the quantities of O_2, CO_2, temperature and relative humidity were extracted to Table 8.

	unit	Min	Average	Maximum
O_3 concentration based in 11 studies	ppb	0	38 ± 30	275
CO_2 concentration based in 7 studies (with pressure corrections)	ppm	410-874	1315 ± 232	1485-3374
Temperature based in 14 studies	°C	17.4-24.6	23.5 ± 0.8	25.4-31
Relative Humidity based in 17 studies	%	0.9-15	16 ± 5	13-77

Table 8. Summary of measured quantities in Chen et al. [133] *study.*

Brief analysis of ASHRAE Research Project 1262

In 2004 the American Society of Heating, Refrigerating and Air-Conditioning Engineers (ASHRAE) started the research project RP-1262 due to the consequences of the National Research Council (NRC) in 2002 [6].

The first part of the report [101] they developed carry-on instrument packages and measured pressure, temperature, humidity, sound, motion, light, air velocity, carbon monoxide, carbon dioxide, ozone, PM, VOCs and SVOCs. Furthermore, a survey to the passengers and crew members was tested and validated on four commercial flights. Additionally, bleed air was monitored for a few minutes during each flight by turning off recirculation air for 5-15 minutes during cruise flight and measuring the air from the gasper. Regarding bleed air there were significant differences in the carbon dioxide and ozone

concentrations because they were close to the atmospheric values (CO_2 = 400 ppm, O_3 = 190 ppb) as expected. VOC concentrations, $PM_{2.5}$ and carbon monoxide concentration were not significant.

In 2018, the second part of the RP-1262 [135] was a gathering of result of 130 surveyed flights with passenger and flight crew surveyed about comfort and health; 80 flights with environmental data. Generally, when cabin air is of low quality there is a trend to report discomfort for passengers, as for cabin crew, the noise and air quality had a greater effect on comfort. It is noted that a better model for air changes per hour (ACH) was developed as a function of current air parameters on measured flights and reported to be significantly less than the traditional model.

Table 9 shows data processed from selected parameters from table 8 of the RP-1262 part 2, organized in passengers and crew members. Each first line of category has the total number of people. For the construction of Table 10, stuffy and drafty air is considered uncomfortable, warm, and cold temperature is uncomfortable.

		Passengers		Crew members	
Category	**Answer**	**Total number**	**Uncomfortable (and very)**	**Total number**	**Uncomfortable (and very)**
Air movement	Stuffy	24% of 5909	37% of 823	30% of 1014	47% of 123
	Drafty	14%	18%	17%	26%
	Neither	62%	45%	53%	27%
Air Quality	Poor	03% of 5906	10% of 813	20% of 987	44% of 116
	Not poor	97%	90%	80%	55%
Freshness of Air	Dissatisfied	8% of 5952	22% of 826	40% of 1020	70% of 123
	Not dissatisfied	92%	78%	60%	30%
Humidity of air	Dissatisfied	10% of 5963	19% of 829	36% of 1022	60% of 124
	Not dissatisfied	90%	81%	64%	40%
Temperature	Warm	14% of 5982	27% of 823	11% of 1024	20% of 124
	Cold	14%	27%	25%	39%
	Comfortable	72%	46%	65%	41%
Odor	Dissatisfied	06% of 5927	15% of 826	23% of 1019	39% of 122
	Not dissatisfied	94%	85%	77%	61%

Table 9. Air quality parameters review by passengers and crew members.

Category	**Answer**	**Every passenger**	**Uncomfortable passengers**	**Every Crew**	**Uncomfortable Crew**
Air movement	Uncomfortable	**38%**	**55%**	47%	73%
	Neither	62%	45%	53%	27%
Air Quality	Uncomfortable	03%	10%	20%	45%
	Not poor	97%	90%	80%	55%
Freshness of Air	Dissatisfied	**08%**	**22%**	40%	70%
	Not dissatisfied	92%	78%	60%	30%
Humid air	Dissatisfied	**10%**	**19%**	36%	60%
	Not dissatisfied	90%	81%	64%	40%
Temperature	Uncomfortable	**28%**	**54%**	35%	59%
	Comfortable	72%	46%	65%	41%
Odor	Dissatisfied	**06%**	**15%**	23%	39%
	Not dissatisfied	94%	85%	77%	61%

Table 10. Air quality parameters focused on comfort by passengers and crew members.

Table 10 shows that from the total number of surveyed passengers (from 5906 to 5982) 38% were uncomfortable with the air movement of the cabin, 28% with the temperature, 10% with humid air, 8% with freshness of air, 6% with the odor and 3% with the air quality. Regarding the uncomfortable and *very uncomfortable passengers* (from 813 to 829) *more than 50% were unhappy with temperature and the air movement*, 22% with the freshness of air, 19% with the humid air and 15% with the odor. In addition, the air tends to be more stuffy than drafty. Additionally, the authors of the report stated that the primary reason for a passenger to be very uncomfortable was the seat comfort.

Regarding passengers' health, more than 25% of the passengers had symptoms from ear, nose, throat, eye, and mouth. The most common symptoms were nasal stuffiness; pain/pressure/blockage in ear; dry, irritated, and itchy eyes; dry mouth.

As for the crew, the total number of surveyed crew members (from 1014 to 1024) 47% were uncomfortable with the air movement of the cabin, 35% with the temperature, 36% with humid air , 40% with freshness of air, 23% with the odor and 20% with the air quality. Regarding the uncomfortable and *very uncomfortable crew members* (from 116 to 124) *more than 70% were unhappy with air movement and the freshness*, more than 50% with temperature and humidity, 45% with the air quality and 39% with the odor. In addition, the air tends to be more stuffy than drafty.

Regarding crew members' health, more than 50% of the crew members had symptoms from ear, nose, throat, eye, and mouth. The most common symptoms were nasal stuffiness (24%); dry/irritate/sore throat (17%), runny nose (15%), hearing loss/decreasing (11%); dry eyes (50%), irritated/itchy eyes (14%); and dry mouth/lips (51%).

Using Power BI and table 11 of RP-1262 [135], from Figure 2-11 it can be deduced that in this study, health and age do not correlate, despite common sense, on a sample of 5796 people where, 20% are less than 30 years old, 21% are 30-39 years old, 23% are 40-49 years old, 20% are 50-59 years old and 16% are over 60 years old.

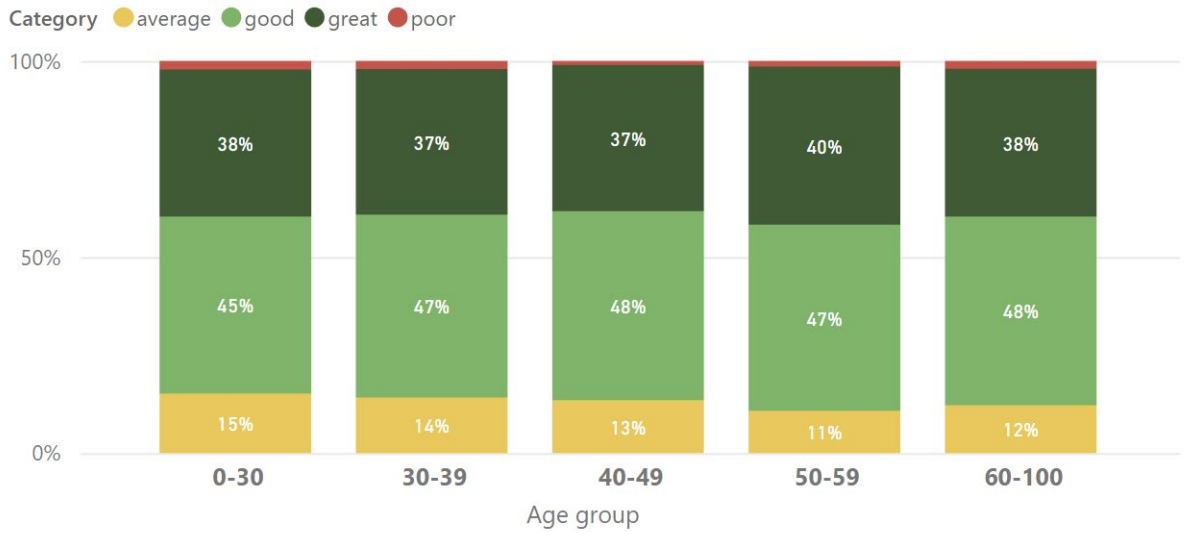

Figure 2-11. Health condition reported by passengers grouped by age groups.

A logistic regression analysis by the authors suggested that with increased cabin temperature, there is an increase incidence of poor health and discomfort; with increased number of air changes per hour, there is an increase of ear pain and general discomfort; with increased humidity reduced nasal stuffiness. A positive correlation was found between ACH and outcomes like pain/stiffness, ear pain/pressure and itchy/irritated eyes. A negative correlation was found between cabin pressure and the former outcomes plus respiratory outcomes.

Ultrafine particles (UFP, $d < 0.1$ μm) were correlated with respiratory outcome indication, making maximum UFP concentration a parameter that predict health outcomes. Tricresyl phosphates (TCPs) were not found above analytical detection limit in all flights. Similarly, several SVOCs were detected in negligible percentages. Measurements of carbon monoxide, carbon dioxide and ozone did not show significant concentrations to relate with health outcomes.

Based on table 19 of the report several values were extracted to Table 11 with data from 56 to 80 different flights.

	unit	minimum	mean	maximum
CO	ppm	0	0.018	0.1
CO_2	ppm	562	1351.8	2051.0
Ozone	ppb	0	15.8	115.6
# particles	/cc	0	617.4	24600
UFP # particles	/cc	0.1	25564	382000
Cabin temperature	ºC	19.22	24.38	31.29
Cabin Relative Humidity	%	1.7	10.74	41.15
Cabin Pressure	kPa	76	79.56	86.80

Table 11. Summary of collected environmental factors of ASHRAE Report 1262 Part 2 [135].

Suggestions

Due to quantity and variety of flights, more statistic surveys should be made to passengers and flight crew. This kind of survey now can become more practical with the use of modern powerful data analysis tools like the Microsoft Power BI and integrated to the entertainment system at landing. This can provide real time and continuous analysis without being expensive. Each airline can have their data for each flight on different planes and if this becomes standard, could upload it to a large global database which could provide valuable intel to the manufacturers.

The adverse effects of cabin environment might not be well known among passengers. If someone become sick after flight and air travel was the reason, they might be not aware, and airlines will not be able to help passengers. Flight measurements are still not able to detect accurately contamination events, so, with this survey, analysts could cross check with health reports and identify possible contamination sources (either biological or cabin).

2.3 Cabin Contamination

2.3.1 Transport of Contaminants

As shown in Numerical Techniques, diffuser accurate modeling is important to predict the velocities in the longitudinal direction and an approach to evaluate the disperse phase needs to be chosen and evaluate their strengths and weaknesses. To study cabin contaminants experimentally several approaches are available: tracer gas like CO_2 can be used to represent a contaminant with a settling velocity, particles injection to study dispersion of small droplets with low settling velocities, aerosolization of bacteria to study bioaerosol dispersion and subsequent growth on agar plates [63].

As previously stated, researchers apply simple boundary conditions for the inlet which is commonly identified as a source of errors. Zhang et al. (2007) [68] first use the Eulerian approach to study a tracer SF_6 contaminant, then on the 2009 study [70] used the Lagrangian approach as well to track $0.7\ \mu m$ Di-Ethyl-Hexyl-Sebacat (DEHS) particulate contaminant after that compared the performance of the CFD methods concluding that both approaches in these conditions, have similar accuracy. Hence, small particles behave like a passive tracer gas. However, for the position near the source, particle concentration was significantly higher than the tracer concentration which could be due to slower turbulent dispersion of the particles. The authors also noted that even though the steadiness of the boundary conditions, the cabin airflow is highly unsteady, arising the question if the time elapsed on the averaged numerical simulations and experimental measurements is sufficient. On Cao et al. (2022) [48] study, the authors agreed that the steady Eulerian method gives reasonable results for the concentration field.

It remains the question of the impact of the boundary conditions accuracy on contaminant transport. This was addressed by Mazumdar [73] in his thesis when comparing the effect of modeling the diffuser as a simple rectangle or as the complex shape with and without its internal parts. He concluded the current complex design promotes longitudinal mixing, enhancing transmission risk of contaminants along the cabin length. To experimentally verify this, CO_2 was injected into the cabin at a height of $1.22\ m$, while sampled at $1.52\ m$ and being numerically simulated as a species on the 11-row KSU-767 mockup. In Figure 2-12 it can be seen there is a significant impact of the inlet boundary conditions on the concentration of CO_2 along the cabin.

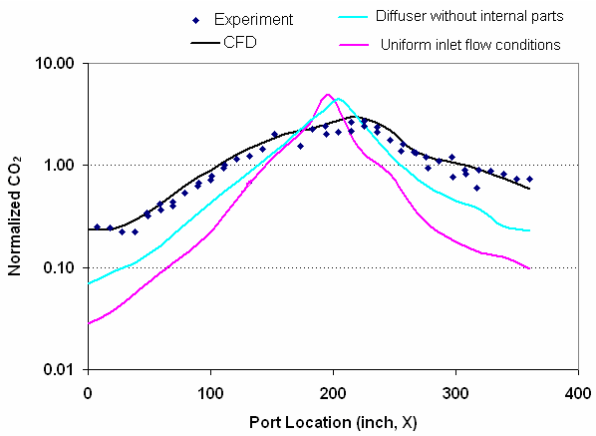

Figure 2-12. Contaminant transport in the 11 row KSU-767 comparing the inlet modeling with contaminant release from the left injection port [73].

In 2020, to respond to the COVID pandemic, a team organized by USTRANSCOM and AMC [136] performed experimental tests both on ground (also with gaspers ON) and in flight conditions on the airframes of Boeing 777-200 and 767-300, leading to a peer reviewed article in 2021 by Kinahan et al. [137]. The injection of the aerosols was made through a nebulizer attached to a mannequin head. The DNA-tagged 3 μm particles (measured with aerosol sampler and surface coupons) were aerosolized for 5 minutes and the fluorescent $1\ \mu m$ (measured by IBAC sensors) for 1 minute on a breathing pattern with or without mask. On average, there was a 15.6% reduction in particle counts at all sensors when

masked were used. However, the fit of the mask could make particles redirect instead of filtering the particles. In summary, the authors conclude that there is a low aerosol exposure risk, however, on average rows in front and behind the index patient have the highest risk and depend on location through the cabin.

The aforementioned experimental results were compared in a computational study by Olson et al. [13] for a Boeing 737, where a manikin coughed polydisperse aerosols. Supply air flow rate had a significant impact on the 95% particles removal time: $4.6\ \mathrm{min}$ for 55% flow rate and $2.4\ \mathrm{min}$ for 100% flow rate. However, this did not increase the maximum exposure. The particle exposure was measured by creating a breathing zone around the manikin head and integrating the inhaled mass over the course of simulations. With this cabin configuration, when the index patient is at the window seat there is a lower risk of exposure. Regardless, in the study, the maximum mass inhaled was 0.3% hence the risk of exposure even for the nearest neighbor is low.

In all the studies so far, the conditions are basically the same where passengers are static, and the cabin is fully occupied. However other factors can influence the contaminant transport such as seats, galleys and toilet arrangement [138] or when a cabin crew is moving a cart along the aisle. Using a small scale model (KSU-767s) for experimental validation, Mazumdar et al. (2011) [139] concluded that the wake by cart movement could have transported the SARS-CoV-1 pathogen from the infected passenger to other passengers seated seven rows away. Additionally, the shape of the moving body affects the contaminant transport, and the movement of the object could carry a contaminant from its source until the place where the object stops.

2.3.2 Recent advances in Cabin Air Quality

Now we are in a condition to better specify the objectives of this dissertation. The Workshop on future Cabin Air Quality Research [140] was conducted in 2020 and briefly presented the state of art on cabin air quality by several researchers and companies. Here are several remarks from the workshop.

- To monitor air quality, we can recur to sensors and human-based surveys. Sensors need to be suitable for the cabin, so they need to be cheap, light, easy to read and clean. Recent developments of sensors have developed sensor networks and e-noses; commercial off-the-shelf (COTS) sensors; miniaturization and digitization. As for the surveys, they should be standardized and be consistent and reliable.
- VITO suggests measures for methodological needs and data assessment needs. The proposed methodology suggests a recruitment strategy to check routine workers and post incidents people; use human biomarkers to test for neurotoxicity and check urinary and breath for hazard compounds; have routine screening and follow-up incidents with a dedicated cabin air quality monitoring. These methods need to be calibrated and validated experimentally, so, a gas generation system within the cabin should be tested. As for the data, it needs to be compiled with existing data of previous and suspected incidents which would require collaboration in aircraft industry and handling confidential data. In summary, the data needs to organized, people should comply with routine medical examination, instantaneous assess when an event

occurs and follow up people who report the incident. If this is achievable, it will be easier to identify, quantify and differentiate contamination events; people will have more confidence avoiding development psychosomatic symptoms and further study might allow identification of mitigation strategies.

- The global cabin air quality executive (GCAQE) noted that while EASA states that chemicals measured below exposure standards, there are no published exposure standards for heated engine oils. GCAQE believes that there is sufficient data to regulate the introduction of bleed air filtration and cabin air quality sensors.
- On the workshop, multiple entities recommend mitigation strategies. ADSE proposed enhanced flight testing by measuring simultaneously outside air, supply air from ECS packs and cabin/cockpit air so the contamination source can be found. Additionally, for engine testing the oil path must be taken into account and to either test the engine at test stand or use a separate compressor that reaches engine bleed air conditions. Mateo et al. proposed the introduction of a de-oiler system before the air goes to overboard vents, managing to improve brush seals and draw conclusions on the breather performance. PALL Aerospace presented their progress on developing sensors smaller than a pencil tip taking to account several requirements and consequences of measuring oil vapors and UFPs because they can coat the surfaces affecting accuracy and life, as well stick to other surfaces generating false positives, moreover, to be aware of aircraft background levels to do not generate false positives due to aircraft age, temperature and ECS state.
- Finally, Honeywell proposed improve the treatment of bleed air to filtrate combined hydrocarbon and ozone, and introduction of air quality sensors in several spots of the air path: bleed air before the converter, bleed air after A/C packs, ground card air, mixed air after the mixer, air inside cabin, recirculated air after the fan.

2.3.3 Contaminants Sensors

According to ASHRAE guideline 28 [7], measurements and contaminant identification can be categorized into three main topics: episodic event, when a person detects odor or irritation that would not otherwise occur; nonepisodic or routine measurements, to characterize the cabin environment; and trend monitoring, to monitor a contaminant expected to change over time like O_3 and CO. On these 3 categories, nonepisodic measurements have been studied the most and published. This report presents several guidelines to aid researchers such as steps to determine the source of odors during episodic events; steps prior to measurements; steps to measure aircraft ventilation rate (total and outside). Furthermore, standard D6399-18 [141] has details about selection instruments and methods specifically designed for aircraft cabins.

There are already several commercial sensor technologies for several cabin contaminants, as shown in Table 12 adapted from [142]. Furthermore, any chosen sensor will be subject to the change of ambient conditions, so the calibration needs to be assured. Further details of cabin air quality investigation can be found in [143], [144] and [145].

Contaminant	*Commercial Sensor Technology*
Engine Oil aerosols and	Light scattering photoelectric detectors
Ultrafine smoke particles	Ionization detectors
CO	Electrochemical cell sensor;
CO_2	Non-dispersive Infrared (NDIR)
Unburned hydrocarbons	Catalytic bead sensor
	Photoionization detectors (PID)

Table 12. Sensor technology for several contaminants

2.3.4 Bioaerosol Sensors

Bioaerosol sampling have three phases: inlet efficiency, either isokinetic or still air; collection or deposition of particles into a collection medium and biological analysis to identify and quantify the bioaerosol particles [18]. Bioaerosol measurements need to sample the particle without changing the physical characteristics or viability of the organism, hence, parameters such as sampling efficiency, collection efficiency and biological efficiency need to be evaluated.

For air sampling we can use inertial impactors, impingers, filters, cyclones, electrostatic and condensation-based samplers. In case of viruses, most air sampling mechanisms may damage sampled viruses either physically or biologically, therefore, techniques like nucleic-acid-based should be used because they do not require intact surface proteins [146].

Bioaerosol sampling can be categorized as active and passive sampling. While active methods allow quantifying bioaerosol concentration, they can be expensive and need air mover and require power. In contrast passive sampling is easy to use but needs to be treated as qualitative. For passive sampling, we can rely on aerosol deposition by gravity or electrostatic forces into a collection medium. Examples of this method include the settling agar plates, electrostatic dust fall collectors and Rutgers Electrostatic Passive Sampler [147].

After being collected, to quantify the state of the organisms techniques can be used such as: culture of Colony-Forming Units (CFUs), direct microscopy, genetic amplification (like PCR), immunochemical and chemical analyses [7].

The key characteristics of bioaerosol sensors are collection time and method, airflow rate, enrichment method, detection method and time, target analyte, limit of detection (LOD), state of organism, and generic characteristics like size, weight, power, cost, portability. There is still no one-fit-for-all solution. A very recent review study by Breshears et al. [148] has an overview of the latest developments in biosensors. For the sampling and detection of SARS-CoV-2 most studies used impactor or impingers air samplers combined with nucleic acid amplification detection. It is noted that there are already some portable sensors to detect bioaerosols on the literature [149–152].

In 2011, Hwang et al. [153] used CFD to assess the feasibility of having a COTS sensor inside a 767 cabin at steady-state conditions for several scenarios. It was concluded that bacteria concentrations

would be high enough when one infected passenger would breathe and sneeze, while breathing alone failed to generate enough bacterial particles for detection, furthermore, there was no scenario where sufficient viral particles would be detected.

2.3.5 Sensors Location

As for the location of the sensors, several authors discussed the possibilities. Mazumdar et al. (2008), using uniform inlet boundary conditions, numerically studied the effect of contaminant release from near the mouth, hand, leg and seat back in front of the passenger, in different seats and 4 different seating patterns in a 4-row mockup and a full cabin model [138]. The following conclusions could be drawn:

- If only one sensor can be put, the best place is the center of the cabin ceiling. The detection time can be reduced if two sensors are placed at the return air grills.
- A multipoint sampling sensor system along the ceiling center collecting air from each location and then average the contaminant concentration would be less sensitive to the local effects caused by galleys, however, increasing extraction points does not guarantee increased performance.

Overfelt et al. (2012) [142] in the KSU-767 mockup experimentally applied a custom wireless sensor network of 12 sensors uniformly distributed across the cabin length. These sensors were placed on top of seatbacks and could measure CO_2, temperature, humidity and pressure. The authors claimed that this network was capable of characterizing in real time the environment of the cabin.

In 2010, Shehadi et al. [154] experimentally studied the placement of sensors in KSU-767 mockup by aerosolizing talcum powder particles from $0.5 - 5\ \mu m$ near manikins lap. A noticeable asymmetry was noticed in the particle distribution behavior in the lateral direction. In this case, if only one sensor could be placed, in the lateral direction the best place would be the centerline of the cabin floor and if one more is available it could be placed near the side wall of seat G. When studying the longitudinal placement by releasing powder at row 2 and row 6 while collecting at the center line of the cabin on adjacent rows, it was concluded that a sensor can be used at the same row of release or ±1 row adjacent.

Then Shehadi, on 2015, after his extensive work on the KSU-767 [127] analyzing turbulence characteristics and realizing that there are multiple circulations across the cabin length, which could be more if the cabin length is longer, suggested installing sensors in low turbulence level regions due to their probable destination for high turbulence energy flow, which could carry contaminants with it.

Furthermore, the cabin HEPA filters can be used to detect virus [155] and bacterial communities [156]. These long sampling periods could be used to characterize a snapshot of the pathogen causing diseases and alert public healthcare authorities.

3 Methods

As stated earlier, the main goal of the thesis is to find suitable locations on an aircraft cabin to implement a bioaerosol sensor that can analyze in a short term period whether airborne pathogens are present at some point of the flight. This would indicate that there is at least 1 infected person with those pathogens.

To find about this, the plan for the thesis was decomposed in three main phases, as follows:

- Phase 1 – Computer Assisted Drawing (CAD) of aircraft cabin and the necessary elements to perform the simulation.
- Phase 2 – Simulation of the single-phase fluid flow (air).
  - Simulation of the west portion of 6^{th} row
  - Simulation of the west portion of rows 5^{th}, $6^{th,}$ and 7^{th}
- Phase 3 – Simulation of contaminant species (moist air components)
  - Simulation of the west and east portion of rows 5^{th}, 6^{th} and 7^{th}
  - Addition of gaspers on rows 5^{th}, 6^{th} and 7^{th}

3.1 3D Modeling

The aircraft that was chosen to perform the simulation was Boeing 767-300ER because it was the aircraft cabin with most documented data, including the geometry of the diffuser inner geometry. Usually, the original dimensions are measured in inches and feet, therefore, when converting the exact factor should be applied ($1\ \text{in} = 25.4\ \text{mm}, 1\ \text{ft} = 0.3048\ \text{m}$).

Due to company confidentiality reasons, it was impossible to obtain a genuine CAD of the aircraft cabin. Several authors tried to simplify the design and use the dimensions that are known from the manufacturer such as cabin height, seat width, cabin width. These can be found at Airplane Characteristics for airport planning documents available at manufacturers' website [157].

The most critical dimension is the width of the diffuser's slot, i.e., the gap on the cabin ceiling where the air is allowed to enter. This width can be used to model the inlet as a simple rectangular opening with a uniform jet with a specified direction. Unfortunately, in the pictures of the manuals, this dimension is not referred, but sometimes can be extracted using extrapolation with known measures and software like Adobe Photoshop or GeoGebra, and cabin pictures from websites can help to verify this measure.

3.1.1 KSU-767 Mockup

Kansas State University researchers have documented the full geometry of the cabin of Boeing 767 (KSU-767), including the geometry of the diffuser before the air arrives to the slot. The diffuser parts were salvaged from real aircraft and used on the cabin. In the literature, it is reported that real diffusers are also used on the Illinois University cabin and on the Technical University of Denmark cabin.

The KSU-767 cabin is composed of ducting, diffuser, storage bin and seats. Before the air arrives to the cabin it passes through a HVAC Air filter, blown to desiccant dehumidification wheels and then an air conditioning system composed of three loops, subsequently proceeding to an electric heater, and finally

arriving to the cabin ductwork. The cabin is composed of 11 rows with seats following the layout of the economy section (2-3-2) of a Boeing 767-300 aircraft, with the mixed class configuration type A door (24 first class seats and 224 economy seats) [110] [157].

The seats in the mock-up are filled with manikins wrapped with electric wire to create a thermal output of 100W. For the contaminant study, the injector is made of a copper tube with $25.4\ \text{mm}$ diameter. Gaspers were installed in 2012 in rows 5, 6 and 7 [52]; they are kept at a pressure of $498.18\ \text{Pa}$ providing a flow rate of $1.6\ \text{L/s}$ when fully opened; each gasper centerline or Personal Air Outlet (PAO) is separated $3\ \text{in}\ (76.2\ \text{mm})$ from each other. The air from the gasper is extracted from the main supply duct.

The dimensions of the mockup cabin are documented in several KSU's research. Most of the measurements were based on [55], [53], [124] and [52]. Some of the measurements are not consistent among documents or were found to be ambiguous, thus, some assumptions had to be made and extrapolations for clarification.

For example, the 3 seats width is reported to be $53.25\ \text{in}\ (1.353\ \text{m})$ however, in Fig 3-2 of Shehadi Thesis [53] the 3 seats length is $62\ \text{in}$, which is the same length as the airport planning manual. To assess this, on Figure 3-1, a real picture from the mockup (Fig 3.17 from Patel thesis [50]) was used to extrapolate dimensions. The average distance of the seat's width was 8.99 units, and their real measure is $18\ \text{in}$. Using scaling, MN distance is calculated to be $57.5\ \text{in}$, while the armrest width is $1.73\ \text{in}$. The total width of 3 seats can be computed as $MN + 2 \times armrest\ width$ giving a total of $60.93\ \text{inches}$ which is closer to $62\ \text{in}$ than $53.25\ \text{in}$, thus, the 3 seats width was computed as $62\ \text{inches}$.

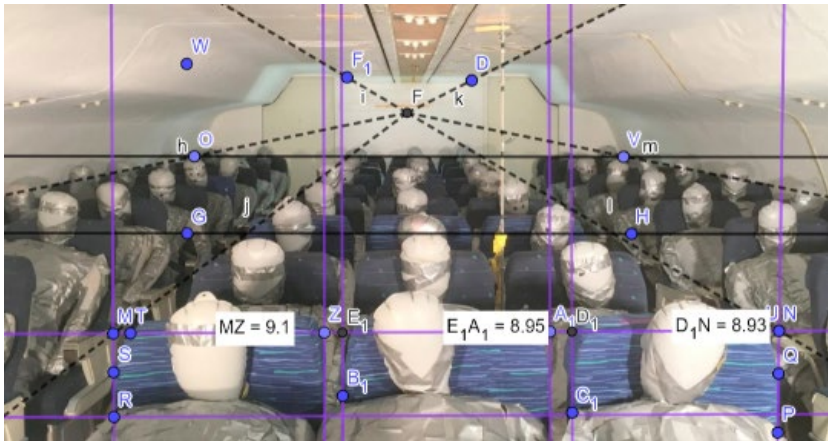

Figure 3-1. 3 seats width scaling and extrapolation from KSU-767 mockup [50].

3.1.2 Final Geometry

To aid future research, all the files related to 3D modeling will be made available. By default, dimensions are in inches because the original referenced documents used inches. The dimensions inside brackets are given in millimeters.

Seats and manikins

Seats were modeled based on Shehadi's Thesis [53] and changing the width of 3 seats abreast to 62 in (1.5748 m), as mentioned earlier; the dimensions can be seen in Figure 3-2 . The manikins shown in

Figure 3-3 were modeled with simple shapes based on [36] and adjusted to perfectly fit the seats, so they were inclined, otherwise the gap between the seat and the back of the manikin would create mesh generation issues.

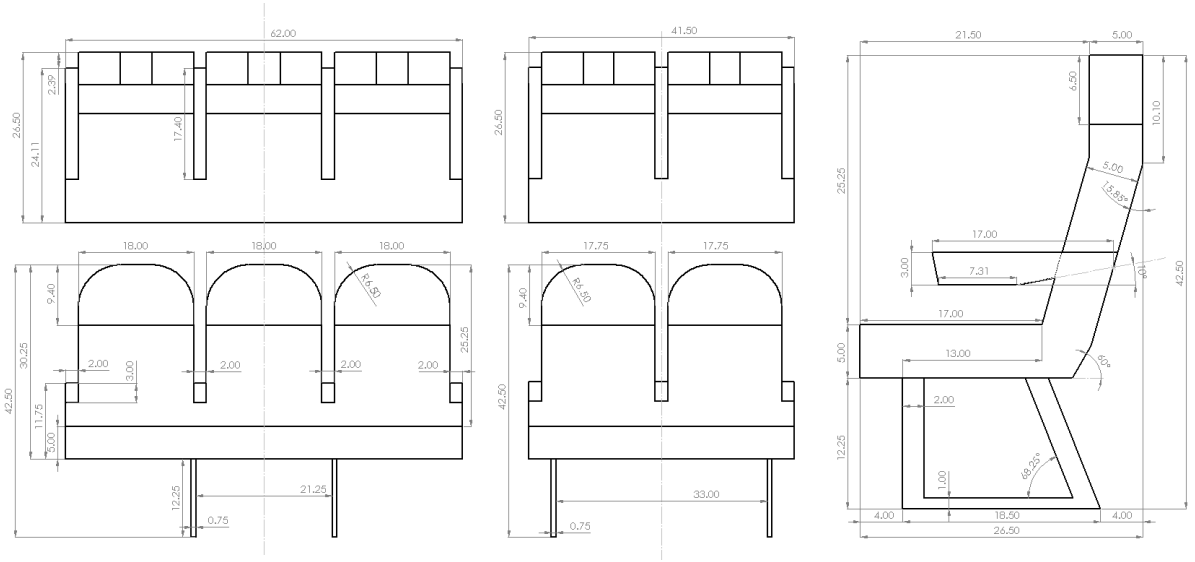

Figure 3-2. 2D Drawings with dimensions of seats. Dimensions in inches.

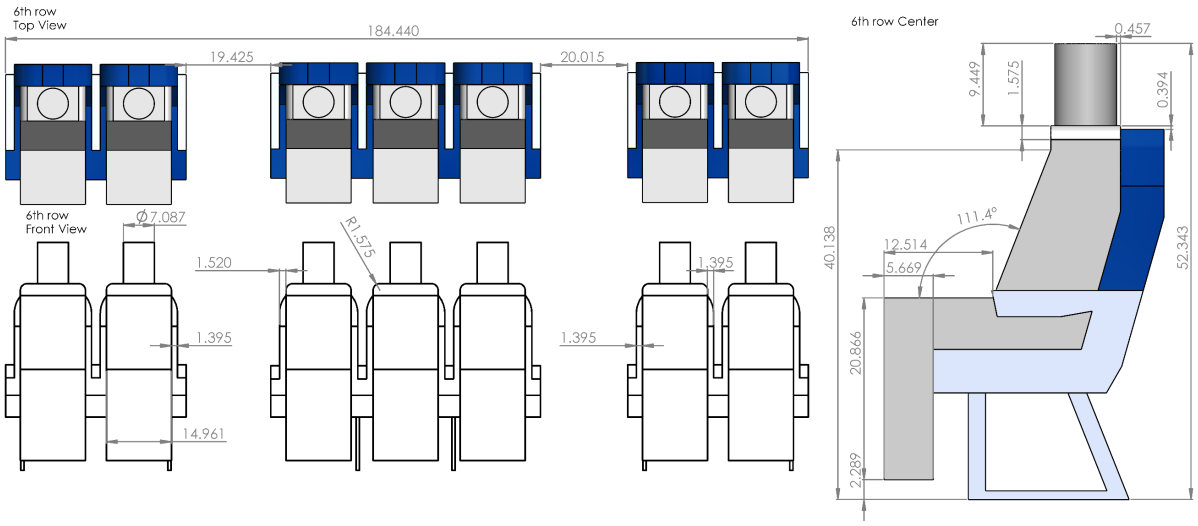

Figure 3-3. 2D drawings of manikins seated in seats of the 6th row. Dimensions in inches.

Cabin Front Section

To construct the cabin front section. Figure 2.10 from [55] was used as background in SolidWorks and some of the known measures were used. The curved surface that connects the sidewall to the ceiling was modeled as an ellipse. Table 13 shows the relevant points to draw the cabin with a precision of 8 numbers. The measures with an asterisk "*" are directly extracted from the references. Figure 3-4 shows the 2D drawing front cross section of the mockup used in this study with the ellipse detailed in Figure 3-5. The reference axis XY is shown, the origin of the reference frame is at the intersection of the "symmetry" plane ($x = 0$) (the cabin is not actually symmetric), the cabin floor ($y = 0$) and the south

wall ($z = 0$). This results in z positive from south wall to north wall, y positive from the floor to the ceiling, and x positive when it is at the west portion and negative when is at east portion.

To construct the cabin front section the following steps were taken:

1. Build the cabin circle C0 with radius of 93 inches.
2. Built the main structure using the points A, B, C, D, F, G, H, I, J, K
3. Build the ellipse using C1 and semimajor and semiminor axis. Then make it tangent to the circle and line passing through FG
4. Point E is where the ellipse is tangent with the circle C0.
5. Add the fillets using the radius R2, R3, R4 and R5.

The maximum width of the cabin is $186\ \text{in}\ (4.7244\ \text{m})$ and the height of the diffuser tip is $78\ \text{in}\ (1.9812\ \text{m})$, while the maximum height is $82.5\ \text{in}\ (2.0955\ \text{m})$.

	X	***Y***
Point A	0.00000000	0.00000000
Point B	*90.50000000	0.00000000
Point C	92.86430894	*14.75000000
Point D	*93.00000000	19.77186859
Point E	83.46283480	60.79488189
Point F	78.35456709	64.16338583
Point G	59.23251050	68.02772122
Point H	49.44767688	82.04245128
Point I	26.15687332	*82.50000000
Point J	*24.75000000	*78.00000000
Point K	0.00000000	*78.00000000

Conic Properties		
Semiminor axis	1.51930046	
Semimajor axis	4.00000000	
Points	***X***	***Y***
Center C1	80.05842465	61.87452599
Focus F1	83.27746583	60.04983424
Focus F2	76.83938346	63.69921773
Center C0	0.00000000	19.77186859

Fillets	***Radius***	***X***	***Y***
C2	2.48984225	60.70315397	70.27069327
C3	2.01567039	48.39634349	80.02720858
C4	*0.75	24.19867971	*78.75000000
C5	*0.75	*7.87500000	*78.75000000

Table 13. Dimensions details of the cabin front section.

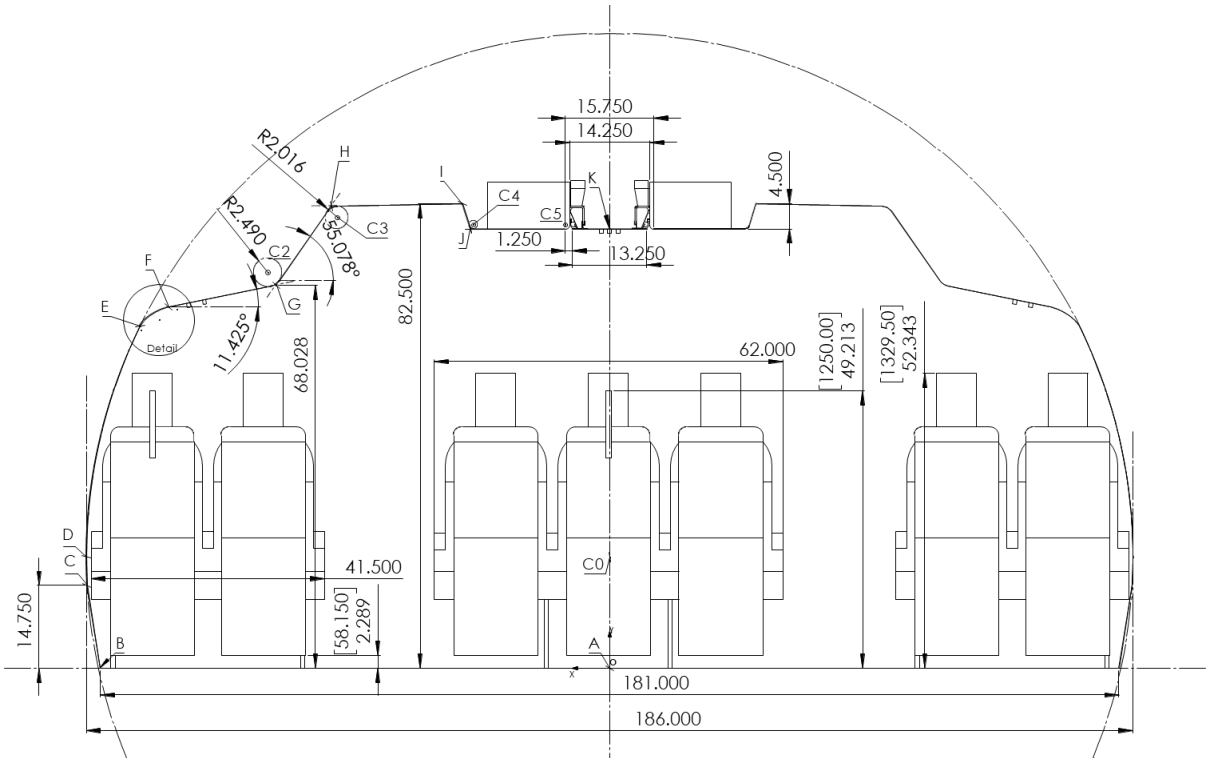

Figure 3-4. 2D Drawing of cabin cross section and dimensions in inches and [millimeters].

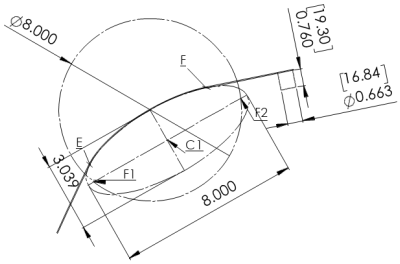

Figure 3-5. 2D Drawing of ellipse detail and dimensions in inches and [millimeters].

Diffuser Cross Section

The internal geometry of the diffuser is complex to model so several assumptions were made based on the references. The diffuser slot gap, i.e., the area between the edge of the radius of the stowage bin and the tip of the diffuser at the ceiling, is assumed to be the sum of the radius of the storage bin 0.75 in with the gap between the tip of diffuser and the end of the storage bin 0.5 in, summing to 1.25 in (31.75 mm), which can be seen shaded in Figure 3-6. The spacing from the cabin centerline to the diffusers tip is 6.625 in (168.275 mm). The distance between the center of the circular hose and the stowage bin is 1.5 in (38.1 mm).

The rest of the dimensions of the frontal area of the diffuser were extrapolated from available images and conjugated with available dimensions, however the pictures were not taken normal to the surface. The thickness of the diffuser metal sheets was assumed to range from 0.05-0.08 inches (1.016 to 2.032 mm), and the angle between the sheet and the ceiling 66.8°. The final result is shown in Figure 3-7.

Diffuser Internal Parts

Figure 3-6 shows the main components of the internal parts of the diffuser in 3D. The spacer buttons are cylinders with 0.375 inches diameter and 0.125 inches length. In this work they were extruded until the metal angle to avoid mesh generation problems. Figure 3-7 shows the resulting 2D cross section modeled in this work. The parts with most uncertainty were the front of the connector and the front of the end cap shown in Figure 3-8 and Figure 3-9. The first iteration of the connector was to model just a small column connecting the two rectangular parts. After analyzing the diffuser's available results, it was deduced that connectors should be wall like to be able to block the flow at that region and create higher velocity maximums. The end cap joints should have a more bevel like structure. However, that would create problems in meshing near the tangent spots.

The layout of supply hoses, connectors and space buttons is detailed explained in appendix 8.1.2.

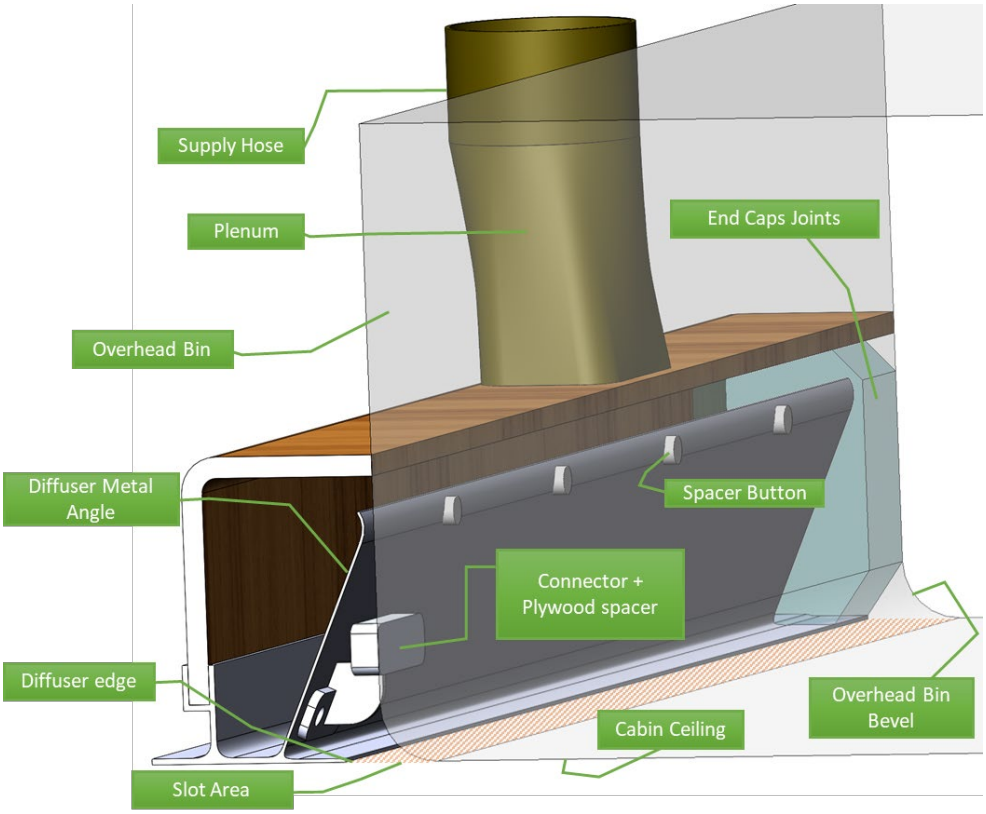

Figure 3-6. Main components of diffuser assembly.

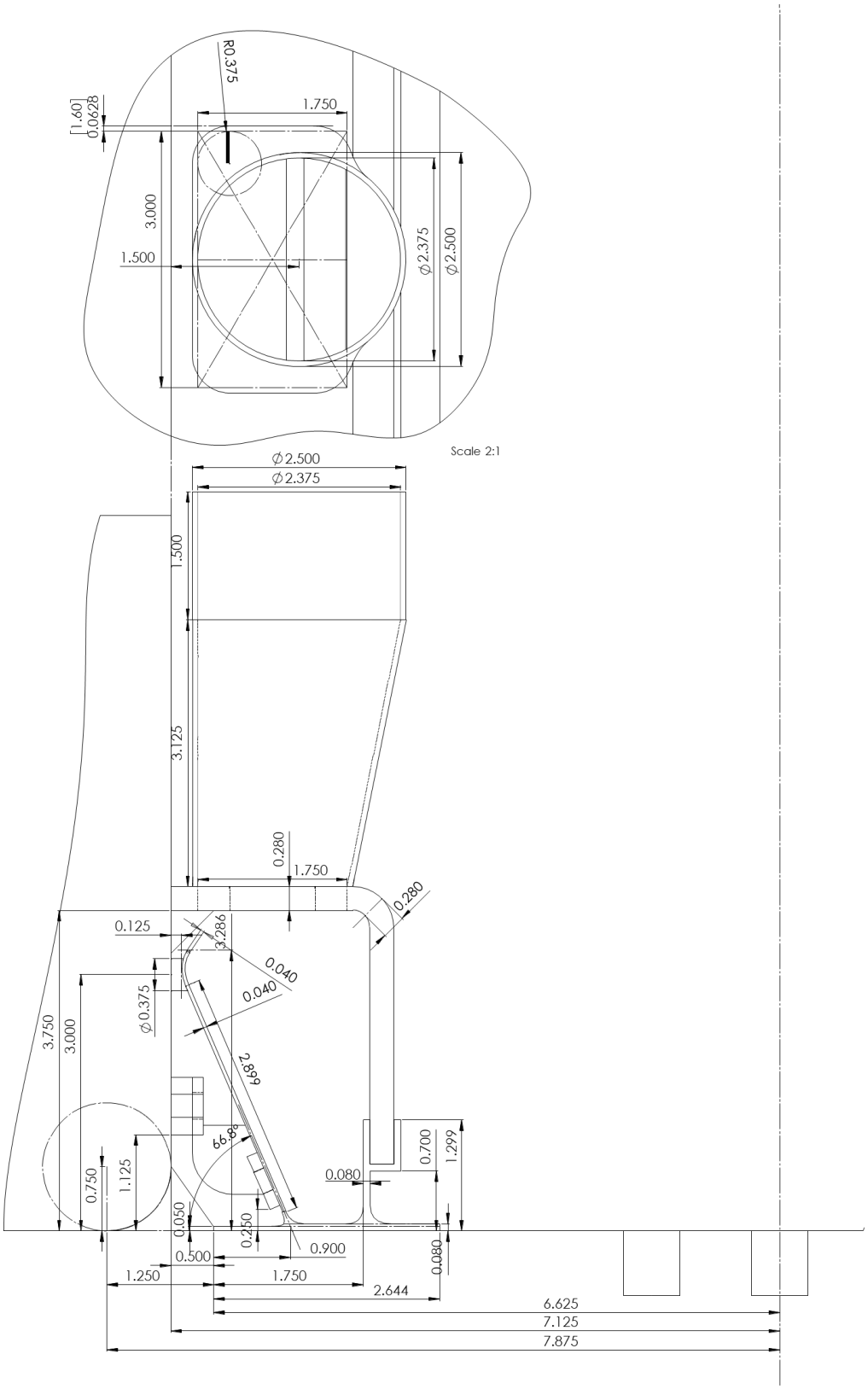

Figure 3-7. 2D Drawing of diffuser frontal cross section with internal parts. Dimensions in inches.

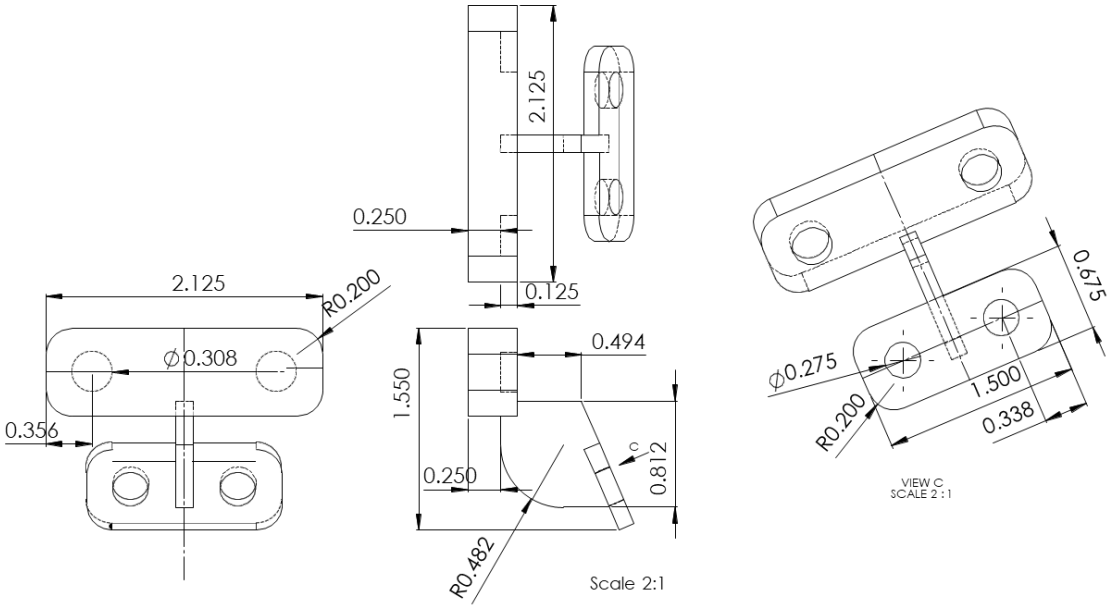

Figure 3-8. 2D Drawing of connectors. Dimensions in inches.

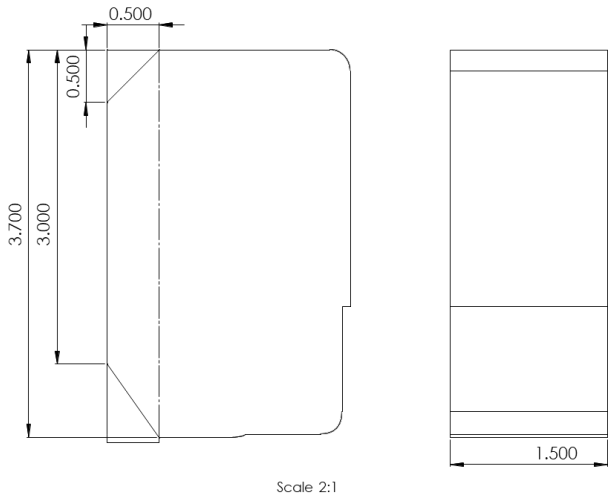

Figure 3-9. 2D Drawing of end cap joints. Dimensions in inches.

Outlets and Seats Layout

According to the reference material [51], the ventilation gaps are 23.5 × 7 inches (575.75 × 177.8 mm). Furthermore, in figure 3.9 of [51], it can be seen that there is a wood baseboard higher than the aluminum channel of the seats' mounting frame. It was assumed that there are 15 outlets on each wall, with a pitch of 25.0375 inches and a spacing of 1.5375 inches. The layout is shown in Figure 3-10.

The seats layout is based on the mounting points distances to the cabin center plane and south wall that can be found in [54]. Further details can be found in the appendix in 8.1.1 - Seats Mounting.

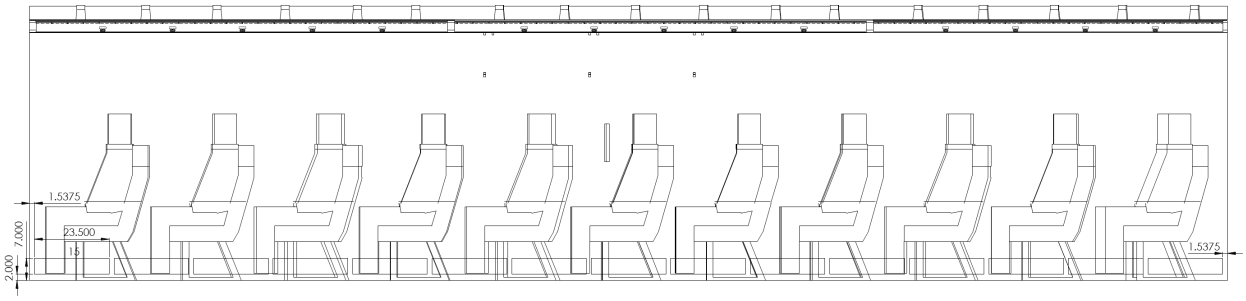

Figure 3-10. Cabin Mockup Outlets layout 2D drawing. Dimensions in inches.

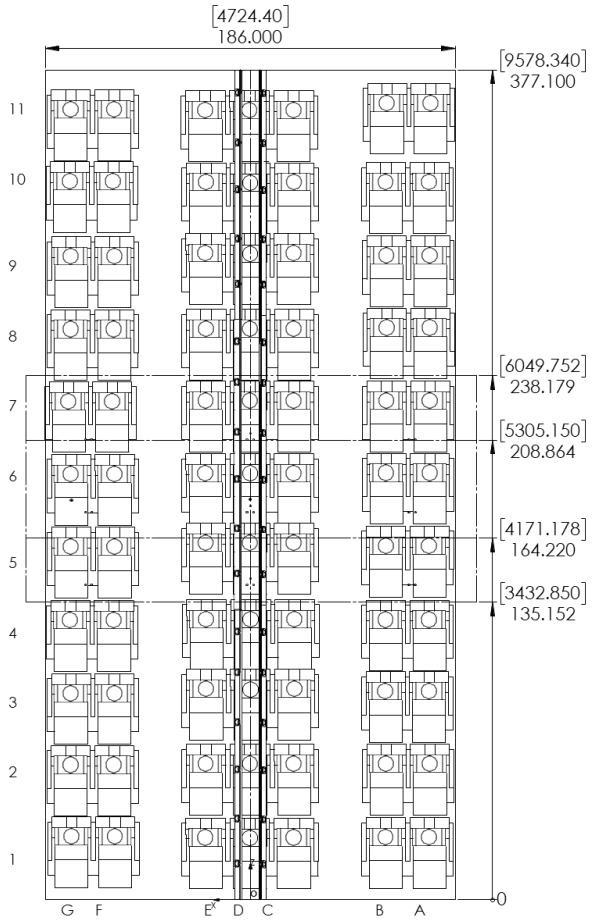

Figure 3-11. Cabin mockup seats layout and sections used as domain in CFD. Dimensions in inches.

Gaspers and Injectors

Gaspers were modeled as simple cylinders directed normal to the surface they were in; the diameter and velocity were computed using relations from the literature [91], assuming they were the same as the referenced paper. This way, the same empirical relations can be used to determine the equivalent cylinder diameter (1) and average velocity (2) . By considering $B = 6.2$, $B* = 0.75$ m^2/s and applying the volumetric flow rate Q =1.6 L/s used in KSU, the equivalent diameter d_{gasper} results 16.84 mm, and the average velocity at the circular face $U_{m,0}$ is 7.183 m/s. The length of the gasper is 19.3 mm.

$$d_{gasper} = \frac{4QB}{\pi B^*} \quad (1)$$

$$U_{m,0} = \frac{\pi}{4Q}\left(\frac{B^*}{B}\right)^2 \tag{2}$$

The accurate location of gaspers and injectors are not mentioned on the literature, so by inspecting Anderson thesis' [52] figures the gaspers were placed in front of the manikins. The distance of the longitudinal direction are as follows: for the side columns, the gaspers are $13.5 - 13.7$ inches from the face of the manikin, for the center column, the closest gasper to the manikin is $11.2 - 12.6$ in, while the other 2 gaspers are 2.6 inches in front of the closest gasper. On the 3-gasper cluster, the centerlines of the cylinders are distanced 3 inches from each other while on the 2-gasper they are 2.88 inches[7]. The lateral distance of nearest gasper to the symmetry plane is 72.074 inches ($x = 1830.68$ mm).

The injectors are modeled as 1 in $(25.4$ mm$)$ diameter cylinder with a length of 11.811 in $(300$ mm$)$. Both of injector's centerline is 8.268 inches $(210$ mm$)$ in front of the corresponding manikin face edge. The lateral distance of G6 to the cabin center is 81.265 in ($x = 2064.131$ mm), while the injector D6 is 0.215 in ($x = 5.46$ mm). Both injectors are at a height of 49.213 in ($z = 1.25$ m) from the floor.

The principal measures using the reference frame of gaspers and injectors can be seen in Figure 3-12. Other dimensions can be extracted using the DWG files or by opening the 3D files on CAD software.

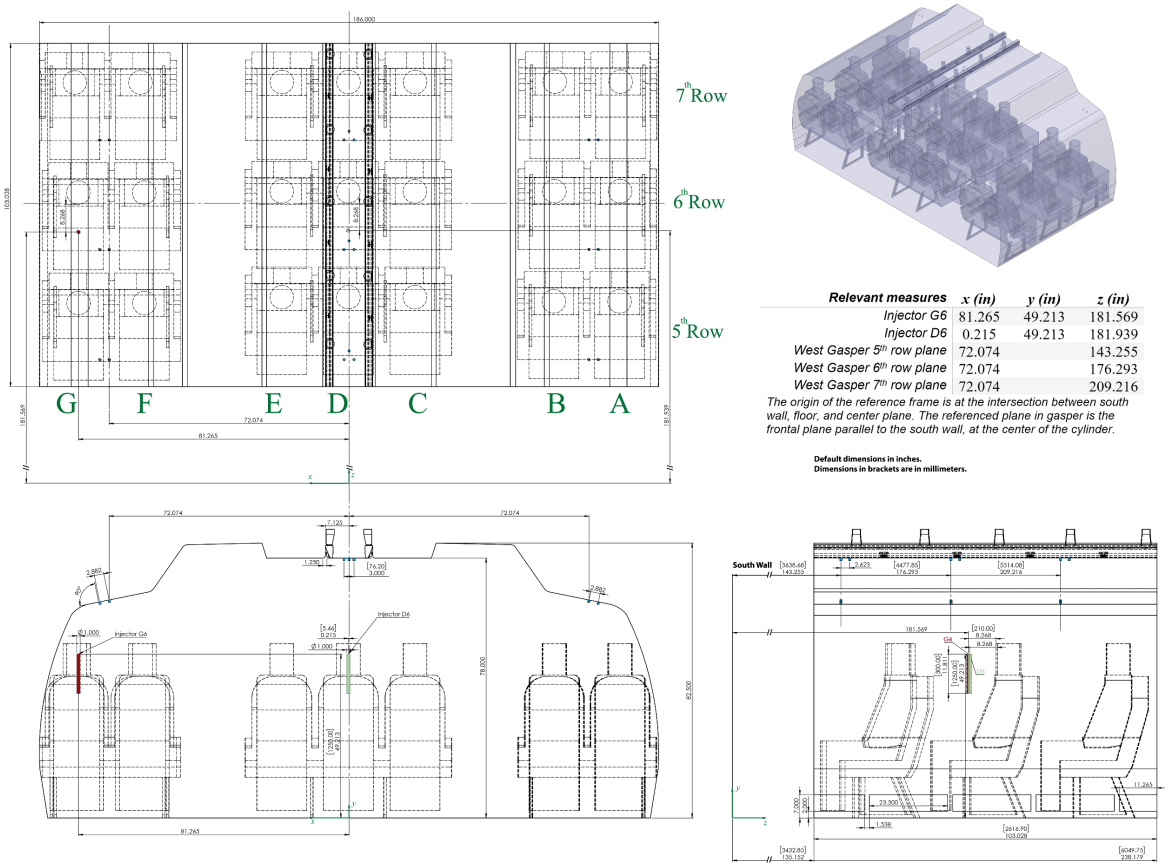

Figure 3-12. Drawings of the 3-row domain used for the final simulations.

[7] This was a minor mistake. In the real mockup it is 3 inches apart.

3.1.3 Mockup vs. real airplane

After validating the CFD methods to study the airflow using experimental data from a mockup, one may choose to simulate the cabin closer to reality. Simulating a mockup have some limitations, namely: the domain is shorter and the walls might have a more profound effect creating large vortex on the top plane [53] [127]; the pressure of the air will be lower depending on the cabin pressure schedule; the seats are arranged in different layouts, which could affect local longitudinal velocities; the design of the walls is outdated. Furthermore, a similar design to the diffusers used on this work can be seen in Figure 3-13 from Aero 15 magazine [158] which depicts a diffuser near the side wall.

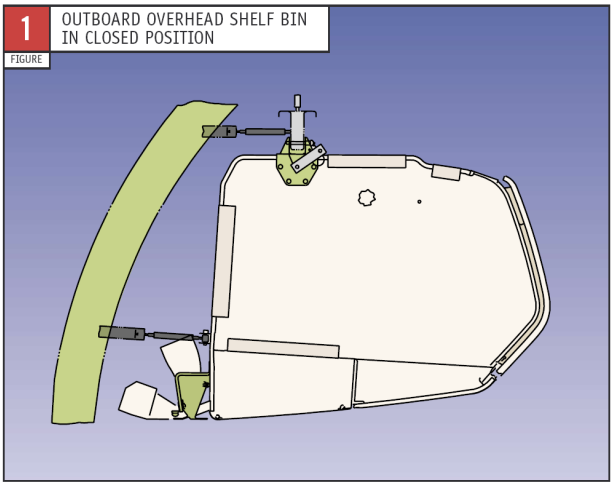

Figure 3-13. Diffuser near fuselage [158].

Figure 3-14 was made combining the pictures of [110] [157] and [159] with the 3D model. One can use this information to model the windows location relative to the cabin.

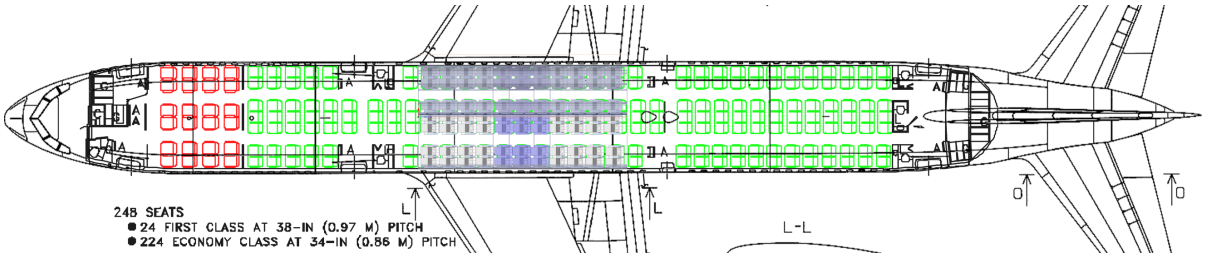

Figure 3-14. 3D Cabin overlay with Boeing 767 drawing.

The layout of windows and seat positions might be relevant if one decides to improve the model and the impact of the thermal conditions imposed by windows. In the case of the Boeing 767, Roskam book [160] has useful drawings of the 767-200 inboard profile and fuselage structural and its said that windows are 10×14 inches. Determining outlets dimensions is more challenging. It can be seen in figure 3.59 in the book – fuselage structural – that each window is between 2 frames. Using image scaling, 5045 px $= 1859.5$ in, so each frame is separated by 22.2 in. Assuming this is true for the 767-300, using

a real image[8] of the outlet and vanishing point tool from Photoshop and the reference length has 22.2 in, the outlet measures about 18.2 inches in length and a spacing of 4 in. With a similar process, using the height of the cabin 82.5 inches as reference and other real image[9], the height of the outlet is 6.74 in from the ground. Using Figure 3-14 and these measures, and knowing that there is one outlet beneath each windows, Figure 3-15 shows the locations as if they were on the KSU-767 mockup.

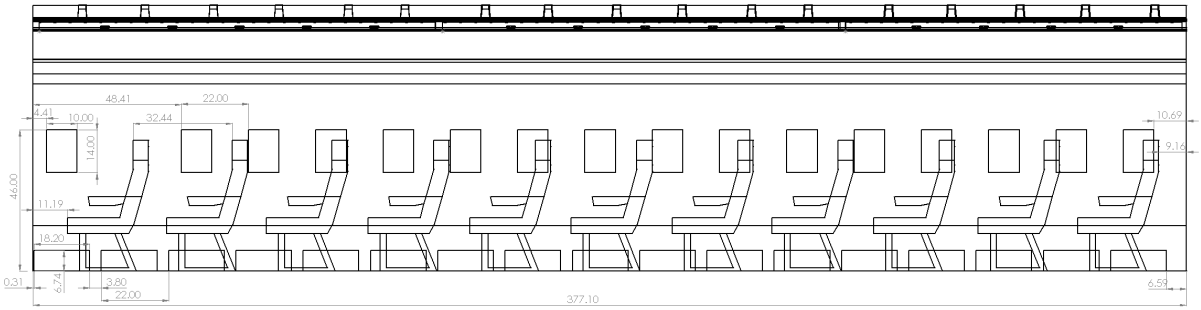

Figure 3-15. Real windows and outlets locations on the cabin section. Measures in inches.

Finally, the design of the cabin interior has been updated over the years. Figure 3-16 a) depicts the oldest design, which is similar to the KSU-767. In May of 2000[10], Boeing announced that 767 will have the "Boeing Signature Interior" to give a more modern look 777-style interior, this can be seen on Figure 3-16 b). Afterwards, in some aircraft the design of the sidewalls and overhead bins changed as well as seen in Figure 3-16 c) [11].

a) 2003. b) 2005. c) 2018.

Figure 3-16. Boeing 767 Cabin Interior taken on different years.

[8]Image P9080054.jpg https://thepointsguy.com/2017/09/where-to-sit-united-767-economy/ by Zach Honig.
[9] Image B767-33A/ER https://www.airliners.net/photo/Ethiopian-Airlines/Boeing-767-33A-ER/0565982/L taken by Raimund Stehmann.
[10] News from Boeing media room website: https://boeing.mediaroom.com/2000-05-16-New-Look-Interior-to-give-Boeing-767-300-a-777-Feel
[11] Images of Figure 3-16 are taken from: https://www.jetphotos.com/photo/109879#modal-large-photo, https://www.jetphotos.com/photo/469824, https://www.jetphotos.com/photo/8977978

3.2 Computational Methods

3.2.1 Computational Domain

The CFD domain used in the simulations for 3 rows was $135.152 < z < 238.179$ inches ($3432.850 < z < 6049.752$ mm) and for 1 row was $164.220 < z < 208.864$ inches ($4171.178 < z < 5305.150$ mm), as shown in Figure 3-11. The domain was cut in Spaceclaim software and the seats that do not belong to the domain in question were removed. The extracting volume tool was applied on the cabin and care was taken because Spaceclaim was not directly used to model the geometry and conversion errors could occur and result in small faces or bad edges; for example, the buttons had to be redone.

The following changes had to be made, namely: as mentioned earlier, the spacer buttons were extruded until the next metal sheet and the manikins should area was pulled to avoid merging the face with the seats. Figure 3-17 shows the domain used in half 1 row simulations, the dimensions of the outlet for the half cabin model were slightly different from the dimensions used afterwards. Figure 3-18 shows the domain used in the final simulations.

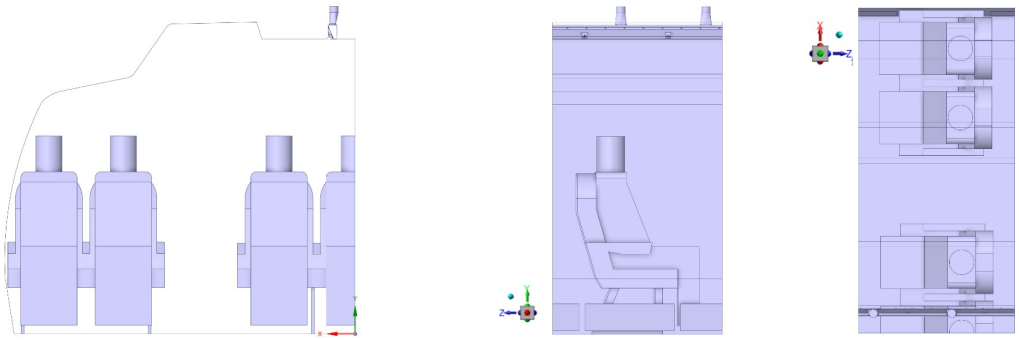

Figure 3-17. 3D model of the extracted volume of half 6th row.

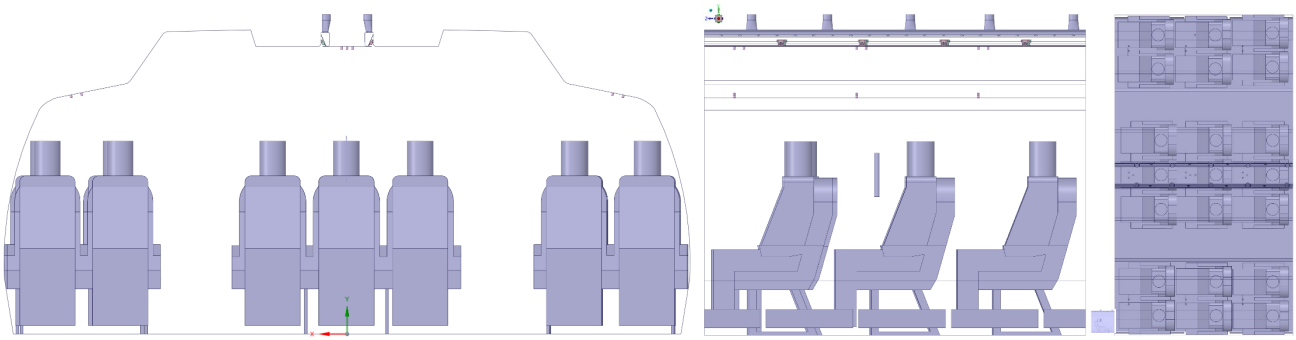

Figure 3-18. 3D model of the extracted volume of rows 5, 6 and 7 with gaspers and injectors.

3.2.2 Governing Equations

To apply CFD to the present problems we must first state the governing laws governing fluid dynamics, which are the conservation of mass, the balance of momentum, and the conservation of energy. These combined represent the transport of mass, momentum and energy as well as phenomena like diffusion, convection, boundary layers and turbulence [19]. However, these laws only apply over a local region and must be formulated according to either Lagrangian (material volume) or Eulerian approach (control volume). To obtain the governing laws applied to control volumes one can apply the Reynolds Transport Theorem. One of the applications of this concept is the transformation of material derivative into local derivative by applying the chain rule. For a field variable $\phi\left(t,\vec{x}(t)\right)$ the material derivative is given by [161]:

$$\underbrace{\frac{D}{Dt}}_{\substack{material\\derivative}}\phi = \underbrace{\frac{\partial}{\partial t}}_{\substack{local\,rate\\of\,change}}\phi + \underbrace{\vec{u}\cdot\nabla\phi}_{\substack{convective\,rate\\of\,change}} \tag{3}$$

where $\vec{u}$ is the velocity vector and ∇ is the gradient operator.

From a Lagrangian point of view, the governing equations of conservation of mass, momentum and energy are, respectively:

$$\left(\frac{dm}{dt}\right)_{MV} = 0 \tag{4}$$

$$\left(\frac{d(m\vec{u})}{dt}\right)_{MV} = \left(\int_V \vec{f}\,dV\right)_{MV} \tag{5}$$

$$\left(\frac{dE}{dt}\right)_{MV} = \dot{Q} - \dot{W} \tag{6}$$

In this section, the transformation of mass and momentum conservation is shown briefly. On a control volume, the continuity equation is valid for compressible and incompressible flows and can be written as:

$$\frac{\partial}{\partial t}\rho + \nabla\cdot(\rho\vec{u}) = 0 \tag{7}$$

If the flow is incompressible, the density ρ does not change with time, i.e., each fluid element will keep the original density along a streamline, which translates mathematically to $D\rho/Dt = 0$, then:

$$\nabla\cdot\vec{u} = 0 \tag{8}$$

After applying the Reynolds Transport Theorem for the conservation of momentum, the conservative form can be written as:

$$\frac{\partial}{\partial t}(\rho\vec{u}) + \nabla\cdot(\rho\vec{u}\vec{u}) = \vec{f} \tag{9}$$

where $\rho\vec{u}\vec{u}$ is the dyadic product and $\vec{f}$ is the external force per unit volume acting on the material volume. For further development, we need to divide the force term in body and surface forces. Body forces typically are gravity, centrifugal, Coriolis and electromagnetic forces. In most cases, only gravitational forces are considered then the body forces are $\vec{f_b} = \rho\vec{g}$, where $\vec{g}$ is the gravitational

acceleration vector. In the case of surface forces, they can be described as a combination of pressure, normal and viscous stresses. So, the total stress tensor of fluids can be decomposed into $\mathrm{T} = -pI + \tau$, where τ is the viscous or deviatoric stress tensor and p is the pressure which represents the negative of the mean of the normal stresses. On a cartesian reference frame, the latter is given by $p = -\frac{1}{3}(\tau_{xx} + \tau_{yy} + \tau_{zz})$. Applying the divergence theorem to the surface forces gives:

$$\int_V \vec{f_s} dV = -\nabla p + [\nabla \cdot \tau] \tag{10}$$

Most fluids, including air and water, can be considered Newtonian fluids, where shear stress is proportional to the time rate of strain (velocity gradients). Then, the viscous stress tensor can be written as eq. (11), where μ is the molecular viscosity coefficient, ζ is the bulk viscosity coefficient where the Stokes hypothesis $\zeta = -2\mu/3$ is considered, as follows:

$$\tau = \mu\{\nabla\vec{u} + (\nabla\vec{u})^T\} + \zeta(\nabla \cdot \vec{u})I \tag{11}$$

For further reference, in index notation the viscous tensor can be further described as:

$$\tau_{ij} = 2\mu S_{ij} - \frac{2}{3}\mu\delta_{ij}\nabla \cdot \vec{u} \tag{12}$$

where $S_{ij} = \frac{1}{2}(\partial u_i/\partial x_j + \partial u_j/\partial x_i)$ is the rate of strain (deformation) tensor.

Thus, considering incompressible flow, Newtonian fluids, the final momentum equation can be written as follows:

$$\frac{\partial}{\partial t}(\rho\vec{u}) + \nabla \cdot (\rho\vec{u}\vec{u}) = -\nabla p + \nabla \cdot \tau + \overrightarrow{f_b} \tag{13}$$

Equations (8) and (13) are commonly known as incompressible Navier-Stokes equations.

3.2.3 Turbulence Modeling

Ansys Fluent uses the Finite Volume Method for the discretization of equations. To get the Reynolds Averaging of the Navier Stokes (RANS), the flow variables need to be decomposed into mean (denoted by a bar $\bar{}$) and fluctuating components (denoted by an apostrophe ‘) [162].

Hence, in tensor notation the instantaneous velocity component u_i is expressed by:

$$u_i = \bar{u}_i + u_i' \tag{14}$$

As for the scalar quantities ϕ such as pressure, temperature, energy, and species concentration, one writes:

$$\phi = \bar{\phi} + \phi' \tag{15}$$

After substituting on (7) and (13), we get the RANS equations in the Cartesian tensor form:

$$\frac{\partial}{\partial t}\rho + \frac{\partial}{\partial x_i}(\rho\bar{u}_i) = 0 \tag{16}$$

$$\frac{\partial}{\partial t}(\rho\bar{u}_i) + \frac{\partial}{\partial x_j}(\rho\bar{u}_i\bar{u}_j) = -\frac{\partial \bar{p}}{\partial x_i} + \frac{\partial}{\partial x_j}\left[\mu\left(\frac{\partial \bar{u}_i}{\partial x_j} + \frac{\partial \bar{u}_j}{\partial x_i} - \frac{2}{3}\delta_{ij}\frac{\partial \bar{u}_k}{\partial x_k}\right)\right] + \frac{\partial}{\partial x_j}\left(-\rho\overline{u_i'u_j'}\right) \quad (17)$$

where the term $\left(-\rho\overline{u_i'u_j'}\right)$ represents the Reynold stresses, which must be modeled for closure of eq. (17). To achieve this, the common approach is to model it based on the Boussinesq's hypothesis, in an analogy with Newtonian flows assuming that the Reynolds stress are a linear function of the mean velocity gradients, yielding:

$$-\rho\overline{u_i'u_j'} = \mu_t\left(\frac{\partial \bar{u}_i}{\partial x_j} + \frac{\partial \bar{u}_j}{\partial x_i}\right) - \frac{2}{3}\left(\rho k + \mu_t\frac{\partial \bar{u}_k}{\partial x_k}\right)\delta_{ij} \quad (18)$$

where k represents the turbulent kinetic energy defined as:

$$k = \frac{1}{2}\overline{u_i'u_i'} \quad (19)$$

and μ_t represents the turbulent eddy viscosity. The main disadvantage of this approach is that this quantity is assumed as an isotropic scalar quantity, which usually works well for shear flows such as boundary layers, jets, and mixing layers.

To model the turbulent eddy viscosity using Boussinesq's hypothesis several models have been developed, such as algebraic models, one-equation models, two-equation models, and second-order closure models. Alternatively, the Reynolds Stress Model (RSM) solves each term of the Reynolds stress tensor, which would be more costly computationally.

In previous work [96] [73], this kind of geometry was simulated using a modified k-ε model and a standard RNG k-ε model employing standard wall functions. As shown in the former review of turbulence models, RNG k-ε model behaves well in this kind of flow. In the appendix 8.4, the calculation of the Reynolds number of the slot area and the nozzle area is performed. It is shown that the flow around in the slot area has a transitional Reynolds number. Chen et al. (2009) [163] analyzed the performance of various turbulence models in this region. Again, the RNG model had a good performance, and the report shows the potential of other models. The realizable k-ε model is more consistent with the physics of turbulent flows by following certain mathematical constraints resulting in a better prediction for the spread of planar and round jets, swirling flows, separation, and adverse pressure gradients, as well as showing good results for contaminant particle transportation.

The two equation family $k-\varepsilon$ model include the standard model, the Re-Normalization Group (RNG) and realizable models. On these models, the transport equations for k and ε are similar. However the method to calculate the turbulence viscosity, turbulence Prandtl numbers and the generation and destruction terms in ε equations are different. The realizable model is validated for a wider range of flows and is more consistent with physics of turbulent flows as well as resolving the round-jet anomaly.

The final chosen turbulence model is a modified version of the realizable k-ε model, by changing the source term S_k in the turbulent kinetic energy k-equation and changing the turbulence Prandtl number for the turbulent dissipation rate σ_ε [96].

Below is presented the original realizable k-ε model implemented in Ansys Fluent 2021. In this model, the turbulent eddy viscosity is computed in eq. (20) linearly, where ε represents the rate at which turbulent kinetic energy is converted into thermal internal energy [164].

$$\mu_t = \rho C_\mu \frac{k^2}{\varepsilon} \tag{20}$$

$$\varepsilon = \nu \overline{\frac{\partial u_i'}{\partial x_k}\frac{\partial u_i'}{\partial x_k}} \tag{21}$$

The final k-equation is shown in eq. (22) and the ε-equation in eq. (23). For simplicity the overbar was omitted.

$$\frac{\partial}{\partial t}(\rho k) + \frac{\partial}{\partial x_j}(\rho k u_j) = \frac{\partial}{\partial x_j}\left[\left(\mu + \frac{\mu_t}{\sigma_k}\right)\frac{\partial k}{\partial x_j}\right] + G_k + G_b - Y_M + S_k - \rho\varepsilon \tag{22}$$

$$\frac{\partial}{\partial t}(\rho \varepsilon) + \frac{\partial}{\partial x_j}(\rho \varepsilon u_j) = \frac{\partial}{\partial x_j}\left[\left(\mu + \frac{\mu_t}{\sigma_\varepsilon}\right)\frac{\partial \varepsilon}{\partial x_j}\right] + C_{1\varepsilon}\frac{\varepsilon}{k}(C_{3\varepsilon}G_b) - C_2\,\rho\frac{\varepsilon^2}{k+\sqrt{\nu\varepsilon}} + S_\varepsilon + \rho C_1 S\varepsilon \tag{23}$$

In eq. (23) $C_1 = \max\left[0.43, \frac{\eta}{\eta+5}\right]$, where $\eta = Sk/\varepsilon$ and $S = \sqrt{2S_{ij}S_{ij}}$ is the modulus of the mean rate of strain tensor.

In the case of the realizable k-ε model, C_μ, unlike in standard and RNG models, is no longer constant. It is a function of the mean strain and rotation rates, the turbulence fields k and ε, the angular velocity of the system rotation, while recovering 0.09 for an inertial sublayer in an equilibrium boundary layer. In the definitions eq. (24)-(26), $\overline{\Omega_{ij}}$ is the mean rate of rotation tensor viewed in a moving reference frame with the angular velocity of ω_k. Further details about the model can be found in Ansys Fluent Theory Guide [162] and [165].

$$C_\mu = \frac{1}{A_0 + A_s\frac{kU^*}{\varepsilon}}, \tag{24}$$

$$A_0 = 4.04; A_s = \sqrt{6}\cos\varphi;\ \varphi = \frac{1}{3}\cos^{-1}\left(\sqrt{6}\,W\right),\ W = \frac{S_{ij}S_{jk}S_{ki}}{\tilde{S}^3},\ \tilde{S} = \sqrt{S_{ij}S_{ij}},\ S_{ij} = \frac{1}{2}\left(\frac{\partial u_j}{\partial x_i} + \frac{\partial u_i}{\partial x_j}\right) \tag{25}$$

$$\begin{gathered} U^* \equiv \sqrt{S_{ij}S_{ij} + \widetilde{\Omega}_{ij}\widetilde{\Omega}_{ij}}, \qquad \Omega_{ij} = \frac{1}{2}\left(\frac{\partial u_i}{\partial x_j} - \frac{\partial u_j}{\partial x_i}\right) \\ \widetilde{\Omega}_{ij} = \Omega_{ij} - 2\epsilon_{ijk}\omega_k, \\ \Omega_{ij} = \overline{\Omega_{ij}} - \epsilon_{ijk}\omega_k, \end{gathered} \tag{26}$$

In eq. (22) and (23), the default constants are $C_{1\varepsilon} = 1.44$; $C_2 = 1.9$, $\sigma_k = 1.0$, $\sigma_\varepsilon = 1.2$. The option to include the rotational term $-2\epsilon_{ijk}\omega_k$ was enabled because neither sliding meshes or multiple reference frames were used in this study.

To implement the turbulence model modification, source terms of the k-equation used in Fluent were compared with the one used in the literature to integrate the previous applied constant in [96] $C_{k2} = 0.77$, a new constant had to be created $C_{k3} = 1 - 0.77 = 0.23$ and integrated in the User Defined Function (UDF) (see Appendix 8.2), as shown in eq. (27). The term $(S_k - \rho\varepsilon)$ is from eq. (22) while the term $(C_{k2}\rho\varepsilon)$ arises from the k-equation in [96] [footnote 6].

$$\begin{cases} S_k = C_{k3}\rho\varepsilon \\ S_k - \rho\varepsilon = C_{k2}\rho\varepsilon \end{cases} \rightarrow C_{k3}\rho\varepsilon = (1 - C_{k2})\rho\varepsilon = 0.23\rho\varepsilon \quad (27)$$

The turbulent Prandtl number for the turbulent dissipation rate was directly implemented in the dialog box σ_ε=1.67 in Ansys Fluent.

Near-wall modeling was handled with Menter-Lechner functions to provide y^+ insensitive wall treatment and avoid drawbacks from using the turbulent Reynolds number for selecting the flow regime, such as treating low k regions with near-wall formulas despite being far away from the wall and problems with convergence in coarse regions. This near-wall treatment is based on the idea of adding a source term in k-equation to account for near-wall effects, which will be active only in the viscous sublayer, and accounting for low-Reynolds number effects.

Furthermore, for reference, in Ansys Fluent, the dimensionless distance from the wall y^+ is defined as follows:

$$y^+ = \frac{\rho u_\tau y_P}{\mu} \quad (28)$$

where $u_\tau = \sqrt{\tau_w/\rho}$ is the friction velocity, y_P is the distance from the centroid of the wall-adjacent cell to the wall and τ_w is the wall-shear stress.

3.2.4 Contaminants modeling

For the species transport, the Eulerian approach was chosen. The conservation equation of a species i is treated using the transport of mass fraction of each species Y_i taking the form:

$$\frac{\partial}{\partial t}(\rho Y_i) + \nabla \cdot (\rho \vec{u} Y_i) = -\nabla \cdot \vec{J}_i + R_i + S_i \quad (29)$$

where R_i is the net rate production of species i by chemical, which will be zero here because these are non-reacting species, S_i is the rate of creation by addition from the dispersed phase plus other user defined sources, and $\vec{J}_i$ is the diffusion flux of species i arising from gradients of concentration and temperature.

Mole fraction X_i is related to mass fraction Y_i using molecular weights of the species M_i and mixture M_m with the following equation:

$$X_i = Y_i \frac{M_m}{M_i} = \frac{Y_i}{M_i}\left(\frac{\rho RT}{p}\right) \quad (30)$$

The options of Diffusion Energy Source and Thermal diffusion options were enabled. Nitrogen was defined as the last species in the species dialog box of Ansys Fluent.

3.2.5 Materials and operating conditions

When the flow was simulated without species, the material that was considered was moist air. When species were turned on, there were 6 different species: nitrogen N_2, oxygen O_2, water vapor H_2O, argon Ar, carbon dioxide CO_2 and helium He. In Ansys Fluent, the materials were defined as follows in Table 14.

	Single Phase	Mixture	Species
Material	Dry air	Moist air	N_2, O_2, H_2O, Ar, CO_2, He
Density	Ideal gas	Ideal gas	-
Specific Heat Capacity	Constant = 1006.13 $J \cdot kg^{-1} \cdot K^{-1}$	Mixing Law	Constant
Thermal Conductivity	Polynomial	Ideal gas mixing law	Kinetic theory
Viscosity	Sutherland's law	Ideal gas mixing law	Sutherland's law
Molecular Weight	Constant = 28.96495 g/mol	-	Constant
Mass Diffusivity	-	Kinetic Theory	-
Thermal Diffusion Coefficient	-	Kinetic Theory	-

Table 14. Materials Definition.

The operating conditions were the same for every simulation. The Boussinesq's temperature was chosen to be 21°C because at steady state conditions the average temperature is known to be between 21°C and 22.5°C. The operating pressure was the same as inside the mockup, set to 98882.53193 Pa, and the local gravity acceleration evaluated at Seaton Hall in KSU (latitude, longitude, mean sea level height) = (39.18916,-96.58260,1070 ft) [166], resulting in -9.79958 m/s^2 on the y-direction [167].

3.2.6 Solution Methods

For the single-phase simulations, the coupled method with default pseudo-transient explicit relaxation factors was used for the pressure-velocity coupling, and changed to the Semi-Implicit Method for Pressure Linked Equations-Consistent (SIMPLEC) when species transport was activated. The discretization of pressure was used with the Pressure Staggering Option (PRESTO!). The summary of applied methods can be seen in the Table 15. All the simulations assume steady state.

	Single Phase	Species transport
Pressure-Velocity	Coupled	SIMPLEC, skewness correction = 2
Spatial Discretization		
Gradient	Least Squares Cell Based	Least Squares Cell Based
Pressure	PRESTO!	PRESTO!
Density, momentum, turbulent kinetic energy, turbulent dissipation rate, species, energy	Second Order Upwind	Second Order Upwind
Additional	Warped-Face gradient correction, High order term relaxation factor of 0.25 all variables For the Coupled method - Pseudo transient, time factor = 1	

Table 15. Chosen methods for pressure-velocity coupling and discretization.

To start the solution, hybrid initialization was employed. Then for the diffuser region ($y > 1.9812$ m) temperature was set to 15.6 °C and 21 °C for everywhere else to speed up convergence. When species were modeled, the domain was patched with the same molar fraction as the inlets. Residuals were also monitored. For the single-phase, continuity residuals were kept below 1×10^{-2}, for velocities under 1×10^{-5}, for turbulent kinetic energy and dissipation rate under 1×10^{-5}, and for energy under 1×10^{-7}. For the species simulation, residuals of He and CO_2 were kept below 1×10^{-5}, and for Ar, H_2O and O_2 below 1×10^{-7}. To ensure convergence, multiple physical quantities were monitored, as presented in Table 16.

Monitor quantities	
Turbulent kinetic energy	inlets, slot, outlets, z-plane of row 6, y-plane of breathing area at $y = 1.25\text{m}$
Temperatures	Volume average temperature of all domain, floor, slot, manikins, z-plane row 6, y-plane of breathing area
Turbulence intensity	Slots, inlets, outlets, z-plane of row 5,6,7 and y-plane of breathing area
Mass flow rate	Inlets, slots, outlets, periodic faces, z-planes of rows 5,6,7 and y-plane of breathing area
CO_2 molar fraction (when species were active)	Monitored at different points to match experimental results; surface average in inlet, exit and volume average of domain

Table 16. Monitored physical quantities.

3.2.7 Mesh Generation

The mesh was composed of prism layers and polyhedral elements. Special care was taken in the region of $1 < y^+ < 5$, so a local face size was chosen near the small parts of the diffuser (0.2 mm in the buttons). The surface mesh was set to have a minimum of 0.5 mm and maximum of 50 mm. The generated volume mesh had 2.51 million (M) elements with a minimum orthogonal quality of 0.122 and a maximum aspect ratio of 508. The high aspect ratio cells are formed on the areas with a high face size and a small prism layer height. This was a compromise to not increase more the number of elements. It is noted that the diffuser region ($y > 1.9812$ m), i.e., above the slot, contains 89% of the total number of cells. The mesh domain for the half of the 6th row is between $4.17114\text{ m} < z < 5.305198\text{ m}$, $0 < y < 2.201037\text{m}$ and $0 < x < 2.362186\text{ m}$. The final volume mesh for the half 6th row can be seen in Figure 3-19.

A mesh with similar parameters was generated for the 3 rows with injectors and gaspers. Smaller local face sizes were defined at the injector and gasper faces when the domain simulated changed. The domain for 3 rows with both sides without gaspers contained 5.78M elements, and with gaspers it was formed by 6.51M elements. The longitudinal domain without gaspers was $3.43285\text{ m} < z < 6.049770\text{ m}$ and with gaspers $3.432836\text{ m} < z < 6.049788\text{ m}$. Near the slot area the mesh is more refined, and the details of the internal parts are depicted in Figure 3-21. The resulting wall y^+ is shown in Figure 3-20.

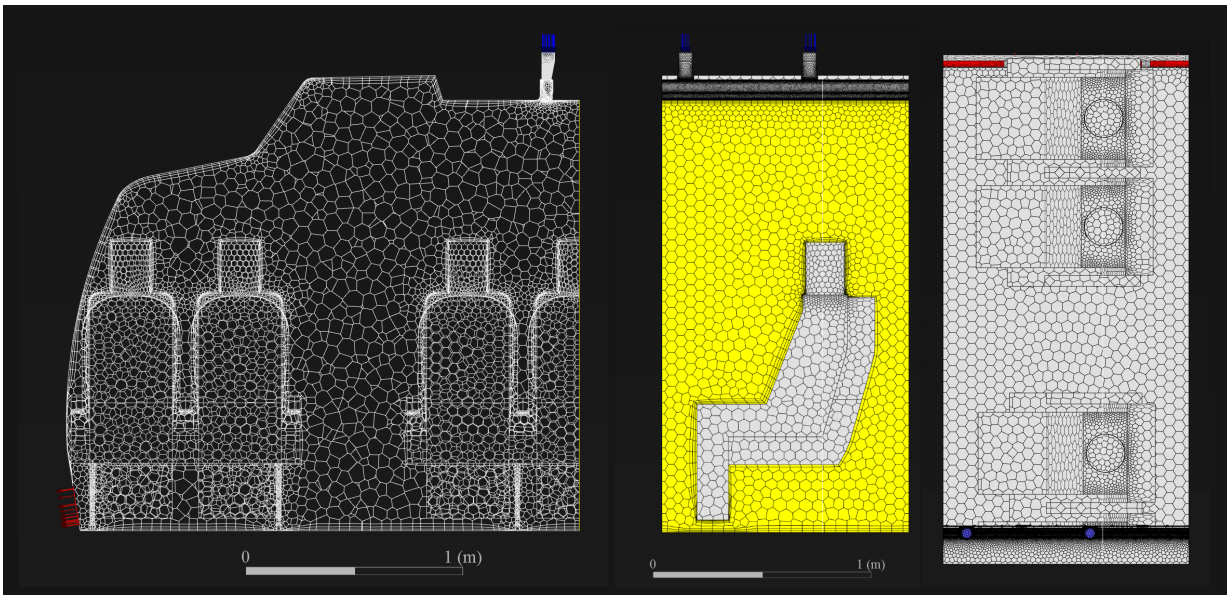

Figure 3-19. Volume mesh for the west portion of the 6th row.

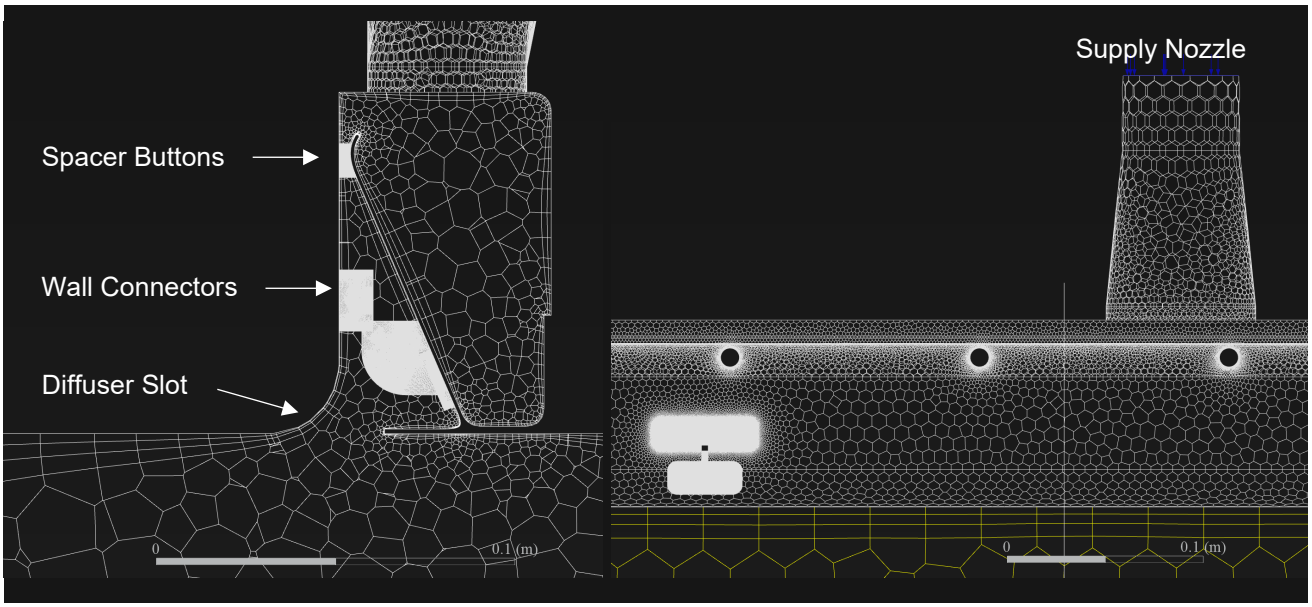

Figure 3-21. Zoom-in of the mesh near the diffuser slot.

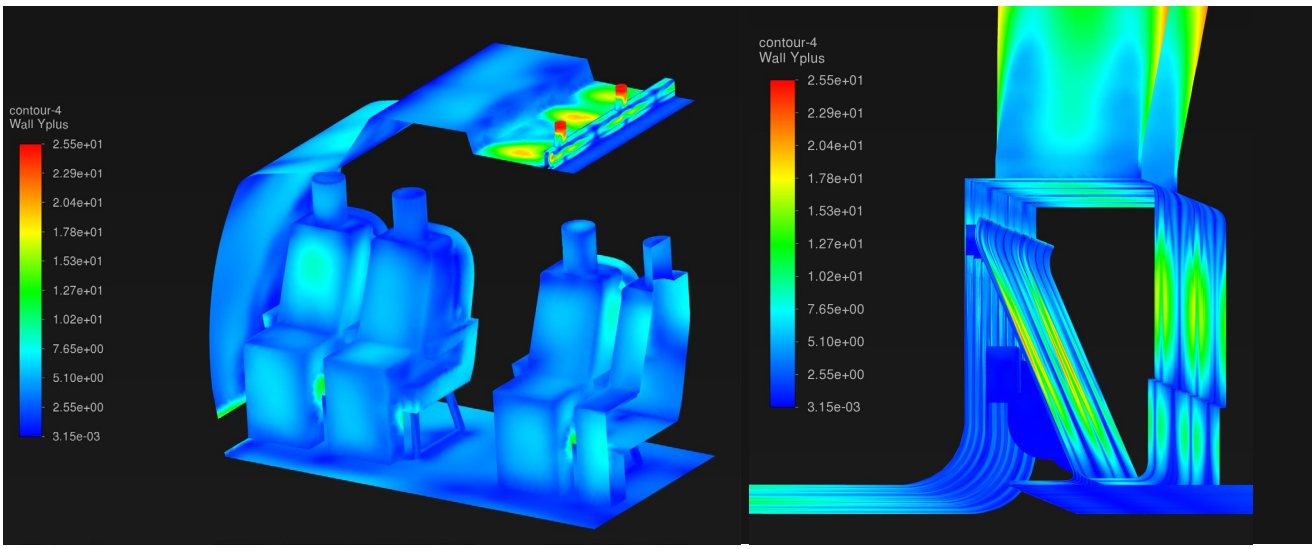

Figure 3-20. Wall y^+ of the west portion of 6th row.

3.2.8 Boundary Conditions

As mentioned earlier, our goal was to simulate the same conditions as those in the mock-up of KSU. The inlets were the supply nozzles that feed the diffuser, with a diameter of $60.325\ \text{mm}$, with a flow rate of $1400\ \text{CFM}\ (660.73\ \text{L/s})$ distributed through 34 nozzles. This defines an average inlet velocity to be $6.799\ \text{m/s}$ and at a static temperature of $15.6\ °\text{C}$. The outlets were allowed to have reverse flow and prescribed at a temperature of $22\ °\text{C}$. To better simulate the physical behavior of the flow, translational periodic boundary conditions were defined at the front and back faces of the domain with flow defined for the z axis, with a pressure gradient of $0\ \text{Pa/m}$ and $21°\text{C}$ for the backflow. When just the west portion of the domain was simulated, a symmetry condition was applied to the plane $x = 0$. The temperature of the manikins is not mentioned in the literature, so the output of 100W was divided by the manikin surface area, which resulted in a heat flux of $52.82\ \text{W/m}^2$.

When gaspers were added, the flow rate directed to the supply nozzles was adjusted. There were 21 gaspers, totaling $33.6\ \text{L/s}$, thus, $627.13\ \text{L/s}$ were directed to the 34 nozzles giving an average inlet velocity of $6.453\ \text{m/s}$.

Physically, there is just one injector at the simulated cabin domain, therefore, after convergence, the profiles of velocity, temperature, turbulent kinetic energy and turbulent dissipation rate were extracted and applied at the front and back faces. This way, it was possible to specify the species molar fraction to be the same as the supply nozzle. In the case of gaspers, a trade-off was taken to not simulate more rows, as this would be true for an infinite number of rows; however, the mock-up in KSU has only gaspers at rows 5, 6 and 7.

When the species were simulated, the molar fractions of moist air with a relative humidity (RH) assumed to be 15% were prescribed at the inlets of the supply nozzles. The supply air CO_2-concentration read by instruments was $400\ \text{ppm}$, so the applied molar fraction (X_i) at the inlets of CO_2 was set to $400\ \text{ppm}$ as well ($X_{\text{CO2,moist air}} = 0.04\%$) . The injector of the contaminant was a mixture of CO_2 ($Q_{\text{CO2}} = 5\ \text{L/min}$) and He ($Q_{\text{He}}=3.07\ \text{L/min}$). Assuming that both tanks of CO_2 and He were at the same temperature and pressure, as well that the exit pressure of the tube and the pressure where they were measured is the same as the cabin, by applying mass and energy balance their properties can be calculated. The injector speed had an average velocity of $0.2654\ \text{m/s}$ and a temperature of $15.6\ °\text{C}$. For reference, the universal gas constant used was $R_u = 8.314472\ \text{J/(mol·K)}$.

The molar fraction of water vapor was computed using the definition of RH and the Buck equation [168] for the saturated water vapor pressure. This resulted in 0.26883% of H_2O and 99.73117% of dry air. Dry air molar fractions of O_2, Ar and He were extracted from International Civil Aviation Organization (ICAO) standard atmosphere manual [169]. Using ideal gas mixtures properties and relations [170] the molar fractions of each component were obtained. The viscosity was computed using Sutherland and Wilke's formula [171]. Table 17 shows the computed properties.

Properties	Moist air	Contaminant
X_{N_2}	7.7869466×10^{-1}	0
X_{O_2}	2.0889691×10^{-1}	0
X_{H_2O}	2.6883154×10^{-3}	0
X_{Ar}	9.3148911×10^{-3}	0
X_{He}	5.2259132×10^{-6}	0.38042131
X_{CO_2}	4.0000000×10^{-4}	0.61957869
Mean Molecular Weight	$28.9365\,\mathrm{g/mol}$	$28.7903\,\mathrm{g/mol}$
Dynamic Viscosity	$1.795725 \times 10^{-5}\ \mathrm{Pa \cdot s}$	$1.576753 \times 10^{-5}\ \mathrm{Pa \cdot s}$
Density	$1.191817888\,\mathrm{kg/m^3}$	$1.185793652\,\mathrm{kg/m^3}$

Table 17. Species properties.

As for the turbulence parameters, the turbulence intensity (TI) was calculated using eq. (31) for fully developed duct flow, and the Reynolds number $\mathrm{Re_{D_h}}$ was computed using the hydraulic diameter [172]. In addition, Table 18 shows a summary of the boundary conditions used in the present study.

$$TI = 0.16\, Re_{D_h}^{-1/8} \tag{31}$$

$$\mathrm{Re_{D_h}} = \frac{\rho U D_h}{\mu} \tag{32}$$

$$TI = \frac{1}{|U|}\sqrt{\frac{2}{3}k} \tag{33}$$

	Momentum and Energy	Species Activated	
Supply Nozzle Velocity	$\vec{u} = -6.79921\,\vec{e_y}\,\mathrm{m/s}$ $D_h = 0.060325\ m, TI = 4.463\%, T = 15.6°C$	X_{N_2}	7.7869466×10^{-1}
		X_{O_2}	2.0889691×10^{-1}
		X_{H_2O}	2.6883154×10^{-3}
	With gaspers $\vec{u} = -6.45345\,\vec{e_y}\,\mathrm{m/s}$ $D_h = 0.060325\,\mathrm{m}, TI = 4.492\%, T = 15.6°C$	X_{Ar}	9.3148911×10^{-3}
		X_{He}	5.2259132×10^{-6}
		X_{CO_2}	4.0000000×10^{-4}
Outlets	Pressure outlet, backflow $T = 22°C$	Same as supply nozzle	
Manikins Walls	Heat flux $= 52.818\,\mathrm{W/m^2}$	Zero flux	
Front and back faces	Translational PBC, $dp/dz = 0\frac{Pa}{m}$, $T = 22°C$, flow direction z	Profiles fixed, species same as supply nozzle	
Injector	$\vec{u} = 0.2654\,\vec{e_y}\,\mathrm{m/s}$ $D_h = 0.0254\ m, TI = 5\%, T = 15.6°\mathrm{C}$	X_{He}	0.38042131
		X_{CO_2}	0.61957869
Other Walls	Adiabatic	Zero Flux	
Gaspers	$\lvert\vec{u}\rvert = 7.183053\,\mathrm{m/s}$ $D_h = 0.016840715\,\mathrm{m}$, $TI = 5.195\%, T = 15.6°\mathrm{C}$	Same as supply nozzle	

Table 18. Summary of boundary conditions.

4 Results and Discussion

4.1 Air Flow Simulation

Now that the 3D cabin model is well defined, a step-by-step approach is taken to simulate the airflow. First, the domain is defined as the west portion of the 6th row to assess how the flow behaves, see how it reacts to different turbulence models and boundary conditions, as well as how to build a good quality mesh. Secondly, the domain was extended to the west portion of rows 5, 6 and 7 with the chosen turbulence model Reynolds-averaged Navier-Stokes (RANS) modified realizable k-ε (r$k\varepsilon$-mod).

4.1.1 Half-row

During the first stage of the numerical simulations, several categories of turbulence models were experimented. In summary, turbulence models employing the k-ε approach performed the best overall, k-ω and SST models performed poorly in the region past the slot. The 3-equation model k-kL-ω performed qualitatively well, however, when checked in quantitative comparisons with experimental results from the probe, it exhibited spikes of velocity without physical meaning.

Before applying the modification to the turbulence model [96], it was noticed that this modification was computed in isothermal conditions for a supply nozzle flow rate about 60% of the flow rate set in KSU-767 supply nozzle ($0.6Q_{\mathrm{KSU}}$ =11.2 L/s , Q_{KSU} =19.4 L/s). Therefore, a validation of the turbulence model was needed to advance to the next phase. To accomplish this important task, the contours of velocity were compared with for different conditions: isothermal flow with 60% of the flow rate, non-isothermal flow with 60% of the flow rate, and non-isothermal flow with 100% of the flow rate.

In Figure 4-1 ($z = 4.9\mathrm{m}$) the Coanda effect at the non-isothermal condition [173] was clearly decreased by the thermal plumes from the manikins, which resulted in directing the jet more to the center of the side passengers. Hence, the flow was divided into two main vortices in the transversal plane (*XY*-plane). This is due to strong buoyancy effects from the thermal plumes of the manikins. The isothermal results were consistent with Lin 2005 [96].

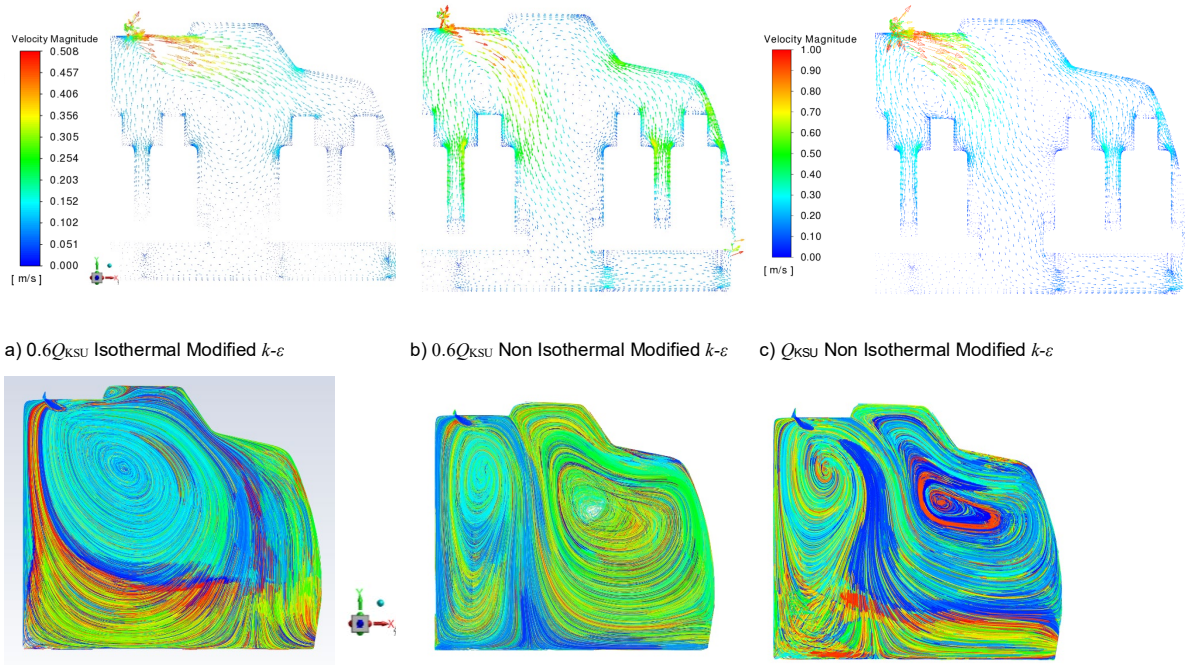

Figure 4-1. Impact of flow rate and temperature on the cabin velocity field (top) and pathlines (bottom).

It is well known that k-ε models are dissipative and the present modification allowed to decrease the dissipation. So, the surface averaged turbulent kinetic energy at the slot area was monitored. It was found that for the realizable k-ε non-modified model $TI_{slot} = 41\%$ and $k_{slot} = 0.93\ m^2/s^2$, while for the modified model, $TI_{slot} = 66\%$ and $k_{slot} = 1.9\ m^2/s^2$. As for the 3-equations transition model k-kL-ω, it was found that the flow is highly transitional, and the total fluctuating kinetic energy at the slot area was $k_{slot} = 3.8\ m^2/s^2$.

Quantitative experimental data of velocity magnitude obtained by an omnidirectional TSI Inc. probe near the slot [54] were compared with results from the simulation. The exact location of the computational probe is set here at $x = 0.225435$m, $y = 1.968027$ m and $4.171178\ m < z < 5.30515\ m$. In Figure 4-2, the velocity from the computational probe with different turbulence models is overlayed with the experimental data, and the west diffuser geometry is scaled to the z-direction.

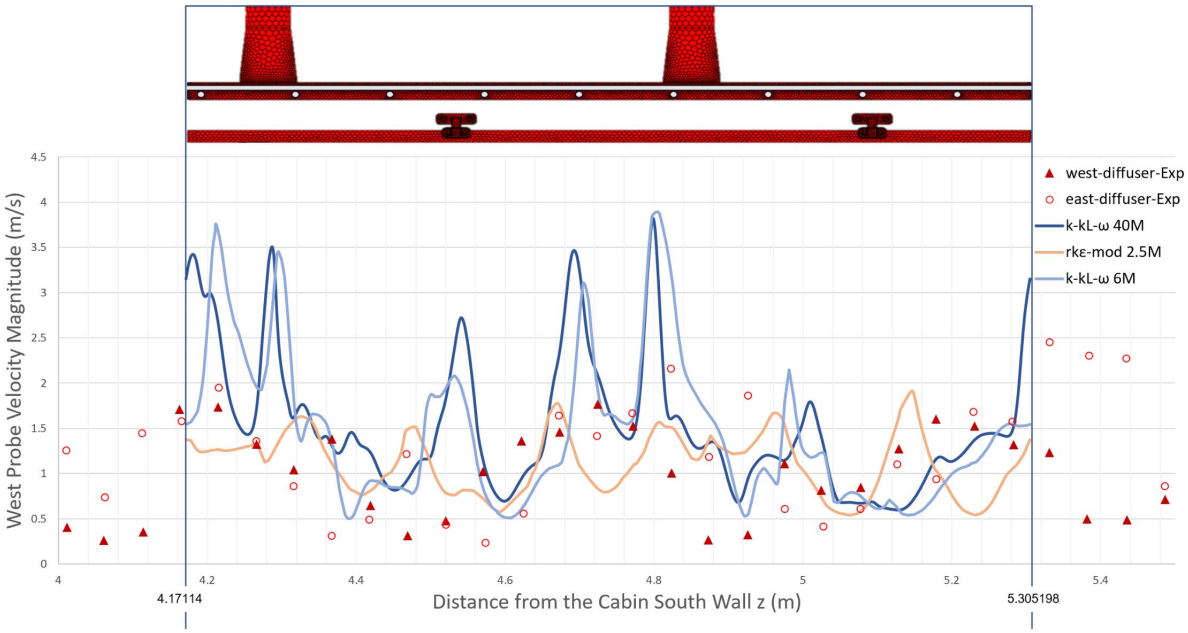

Figure 4-2. Velocity magnitude at west probe for different turbulence models.

In the slot area, the flow was rather complex as reported in the literature. In Figure 4-3, one may observe the plots of turbulent kinetic energy, velocity magnitude, turbulence intensity and static temperature at the slot. In Figure 4-4 it can be seen a detailed area of the velocity magnitude from the diffuser jet. In Figure 4-5 it can be seen that the modification applied to the k-ε model improved the accuracy of the simulation at these critical locations. The data in the plot of turbulence intensity is computed using eq. (33).

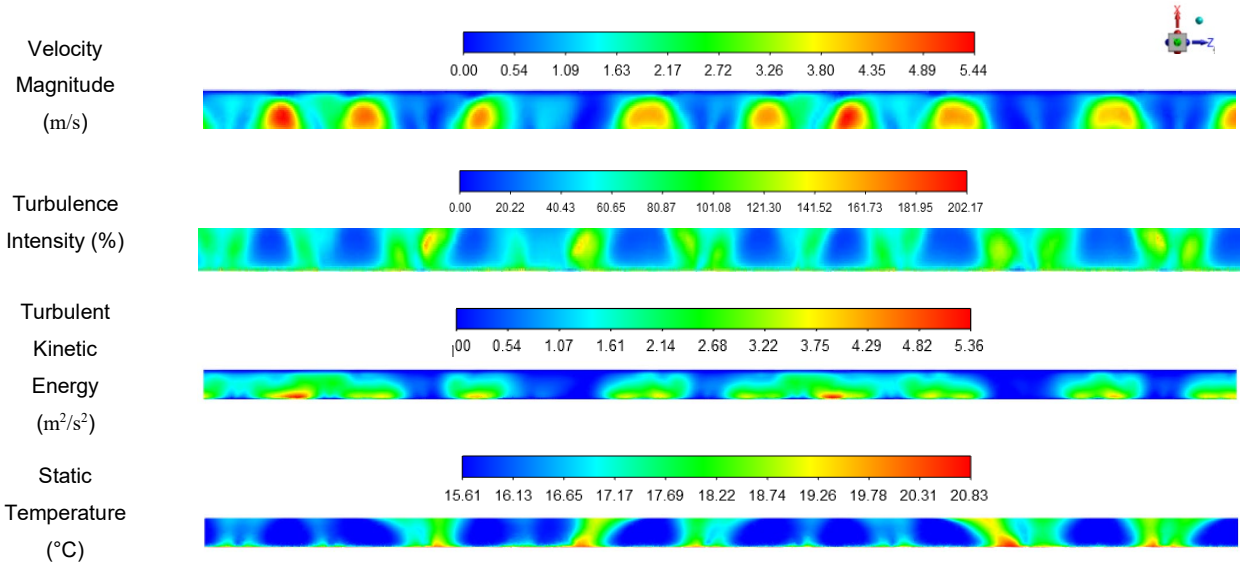

Figure 4-3. Contours of flow quantities at the slot area.

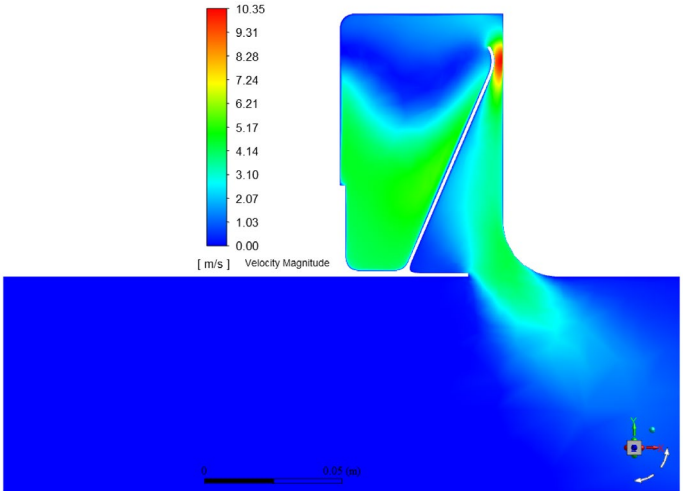

Figure 4-4. Velocity magnitude contour for the diffuser at $z = 4.783415\ m$.

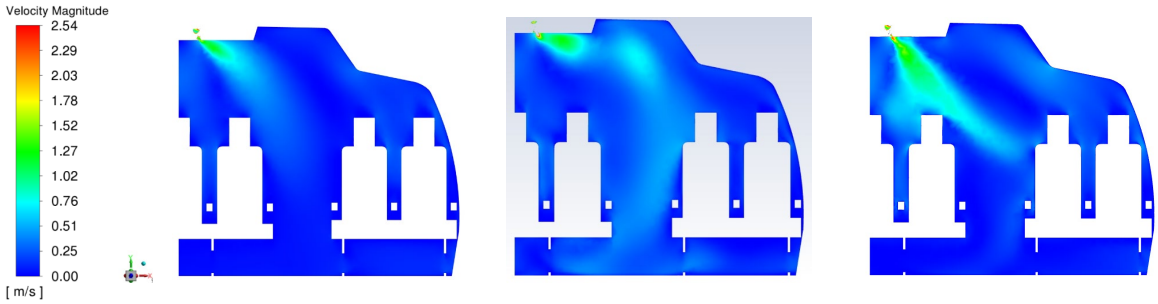

(a) k-ε realizable modified *(b) k-kL-ω* (c) k-ε realizable original

Figure 4-5. Velocity magnitude contours for different turbulence models.

4.1.2 Three-rows

Momentum and Energy

In Figure 4-6 it can be seen the results of the simulation from 3 rows when the injection at G6 was activated with species model. Despite the geometrical asymmetry in the diffuser parts, i.e., the diffuser buttons, connectors and joints not being in the same plane and the seats not being on the same plane, the flow appears to be symmetric. It is noted that in this domain, the spacer joints were not simulated. The domain could be halved, however, to simulate the injection at the center of the cabin D6, the west and east portion needed both to be simulated.

As can be seen in Figure 4-6, there is a significant longitudinal velocity on the aisles area and the flow is governed by two large vortices in the transverse plane. In the symmetry plane, the influence of the thermal plume makes the velocities reach $38\ \mathrm{cm/s}$. The injector inlet has a velocity of $26\ \mathrm{cm/s}$, however, globally the gas does not significantly disturb the flow, therefore one may assume that it behaves mostly as a tracer gas or passive contaminant.

Regarding the temperatures, when 3 rows are simulated with the injector turned on G6, the average temperature of the cabin is $22.3°\mathrm{C}$, while the average temperature of the manikins is $32.1°\mathrm{C}$. As with

Figure 4-2, experimental data was compared with the computational probe for the west and east domain in Figure 4-7.

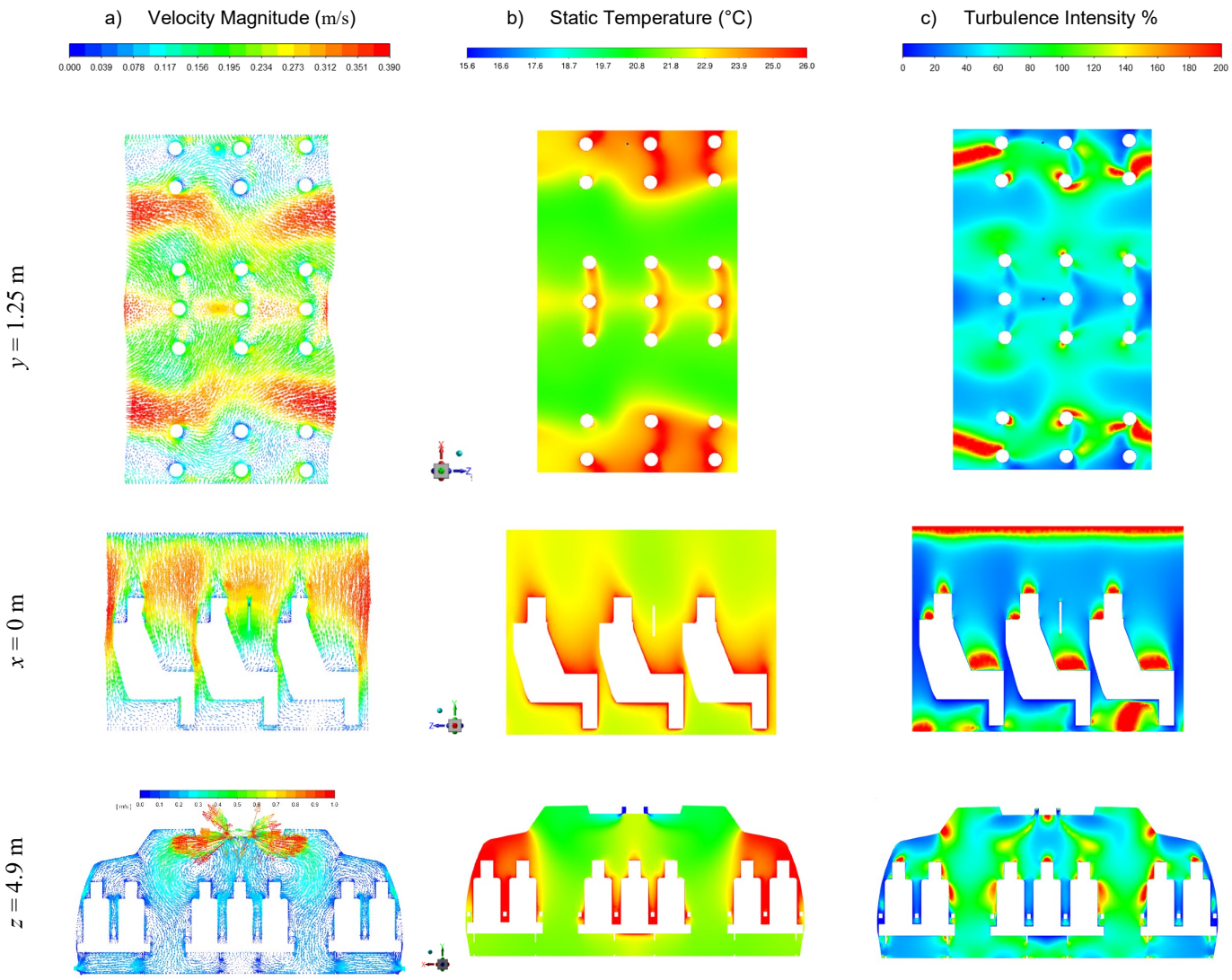

Figure 4-6. Velocity, temperature, and turbulence intensity contours for 3 rows with G6 injector.

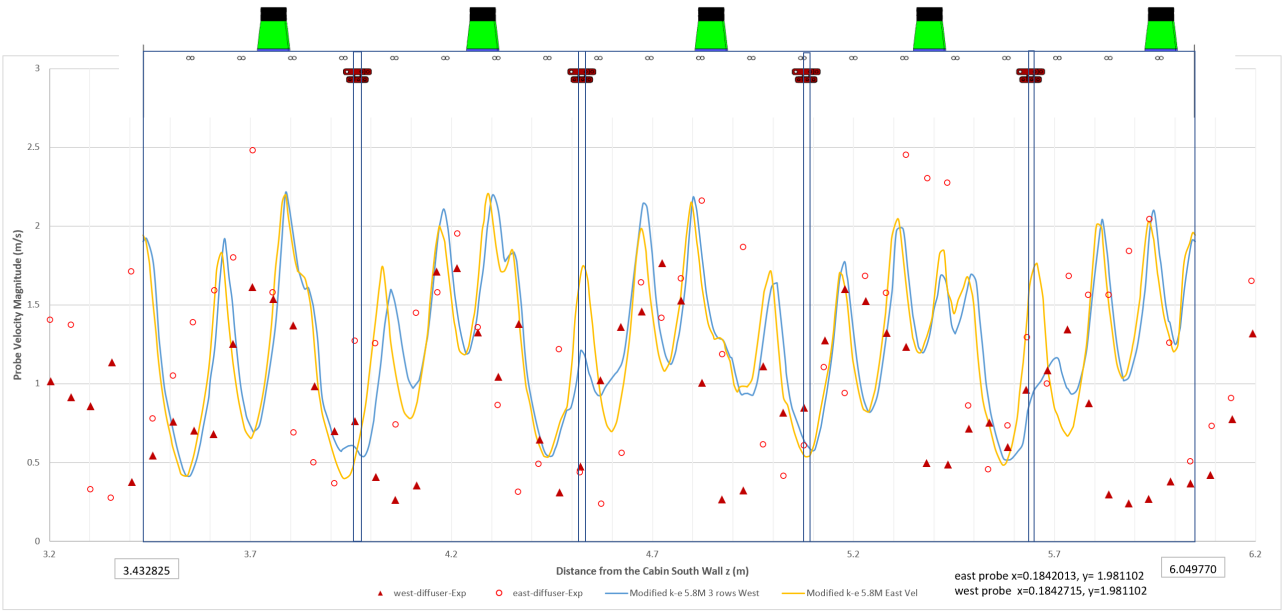

Figure 4-7. Velocity magnitude at probes through 3 rows vs experimental data.

4.2 Contaminants

The full 11-row cabin interior with the origin of the reference frame and numbers of rows and letters of columns can be seen in Figure 4-9. Gaspers are considered to be $533\ \text{mm}$ in front of the seat headrest, hence the gaspers on the 5th row are located at $z = 3.63855\ \text{m}$, on the 6th row at $z = 4.47853\ \text{m}$, and on the 7th row at $z = 5.31343\ \text{m}$ [52]. The first gasper of the 2-cluster on rows F, G correspond to $x = 1.82762\ \text{m}$, and the second has $x = 1.89938\ \text{m}$.

Figure 4-9 shows the results of the molar fraction of CO_2 in ppm overlapped with the experimental data from the literature [51]. The injector center face at D6 is at $(x, y, z) = (0.005465\ \text{m}, 1.250235\ \text{m}, 4.621249\ \text{m})$, while the injector center face at G6 is at $(x, y, z) = (2.06414\ \text{m}, 1.250234\ \text{m}, 4.61185\ \text{m})$. The distances of the points in the same line are $0.84\ \text{m}$ between each other, and the experimental results are overlayed in the pictures. Discrepancies to the experimental results are noticeable. This difference can be explained by the absence of gaspers in the simulation which would create high momentum cold jets and decrease the momentum of the thermal plume as well as, depending on the direction of gaspers, redirect the trajectory of the contaminants.

Furthermore, one limitation of this simulation is to imply periodic boundary conditions, which would create an infinite number of rows; however, the mockup cabin is composed of only 11 rows. According to the image of the trajectory of the tracer gas suggested by Shehadi [126] in Figure 2-10 b), this would create one large vortex near each end and two vortices near the center, probably caused by the influence of the physical cabin walls at the extremities. Gaspers were turned OFF in Shehadi's study[12].

[12] Shehadi, Maher. "Re: Use of gaspers in KSU". Received by Carlos Raposo ResearchGate, 26 Set. 2022.

In Figure 4-8 and Figure 4-9 the molar fraction of CO_2 is plotted in the planes that cross the center of the respective injector. Figure 4-8 c) shows the YZ plane in the center of G6, Figure 4-8 d) portrays the YZ plane in the center of D6, Figure 4-8 a) depicts the XY plane in the center of G6, and Figure 4-8 b) illustrates the XY plane of D6. Moreover, Figure 4-9 a) and b) show the plane of breathing area corresponding to $y = 1.25$ m (same as the injection).

With gaspers off, it can be seen that the thermal plumes transfer momentum to the convective transport of the contaminant CO_2. When injected at the side wall, and because of the low ceiling, the contaminant is transported to row 7, eventually putting the passengers in risk. On other hand, when injected at D6, the contaminant climbs higher, which allows it to dissipate into the back rows, storage bins and aisles. Surprisingly, it appears that passengers seating next to the source D6 are not that much affected by the contaminant due to the thermal plumes and the large vortex that pushes the air away [174]. However, when injected at the side, there is significant transverse transport explained by the presence of a small vortex caused by the flow, as seen in Figure 4-6 a).

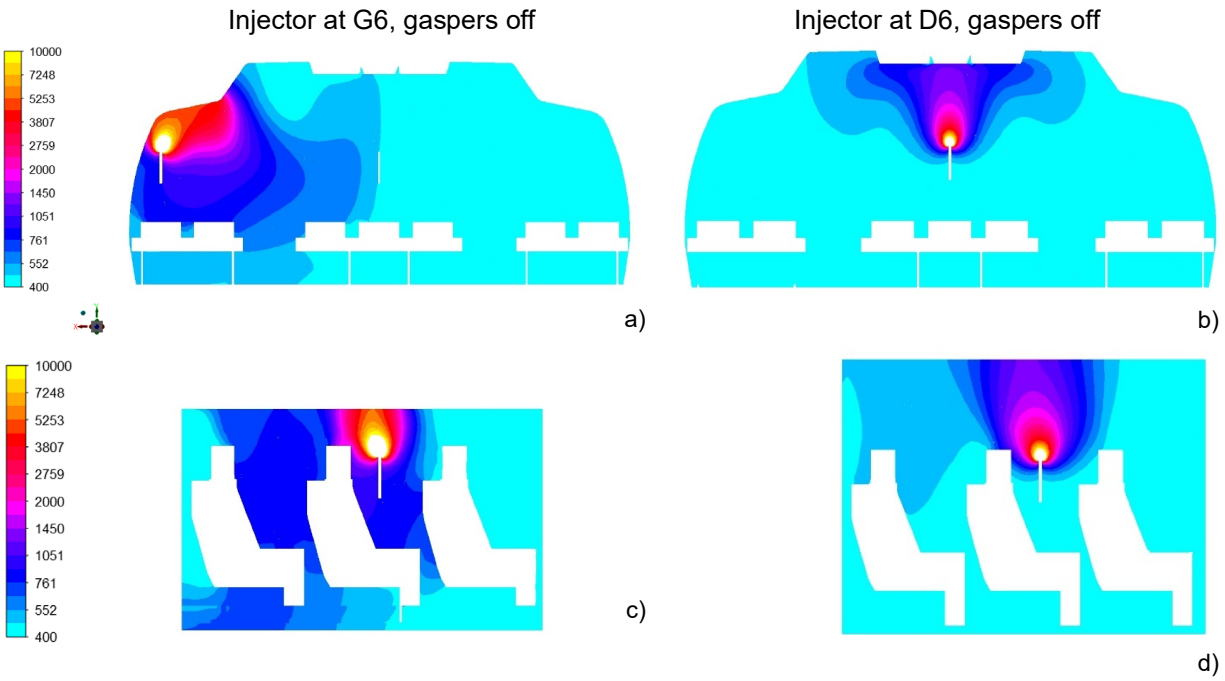

Figure 4-8 Gaspers off: molar fraction of CO_2 in ppm at front and side planes

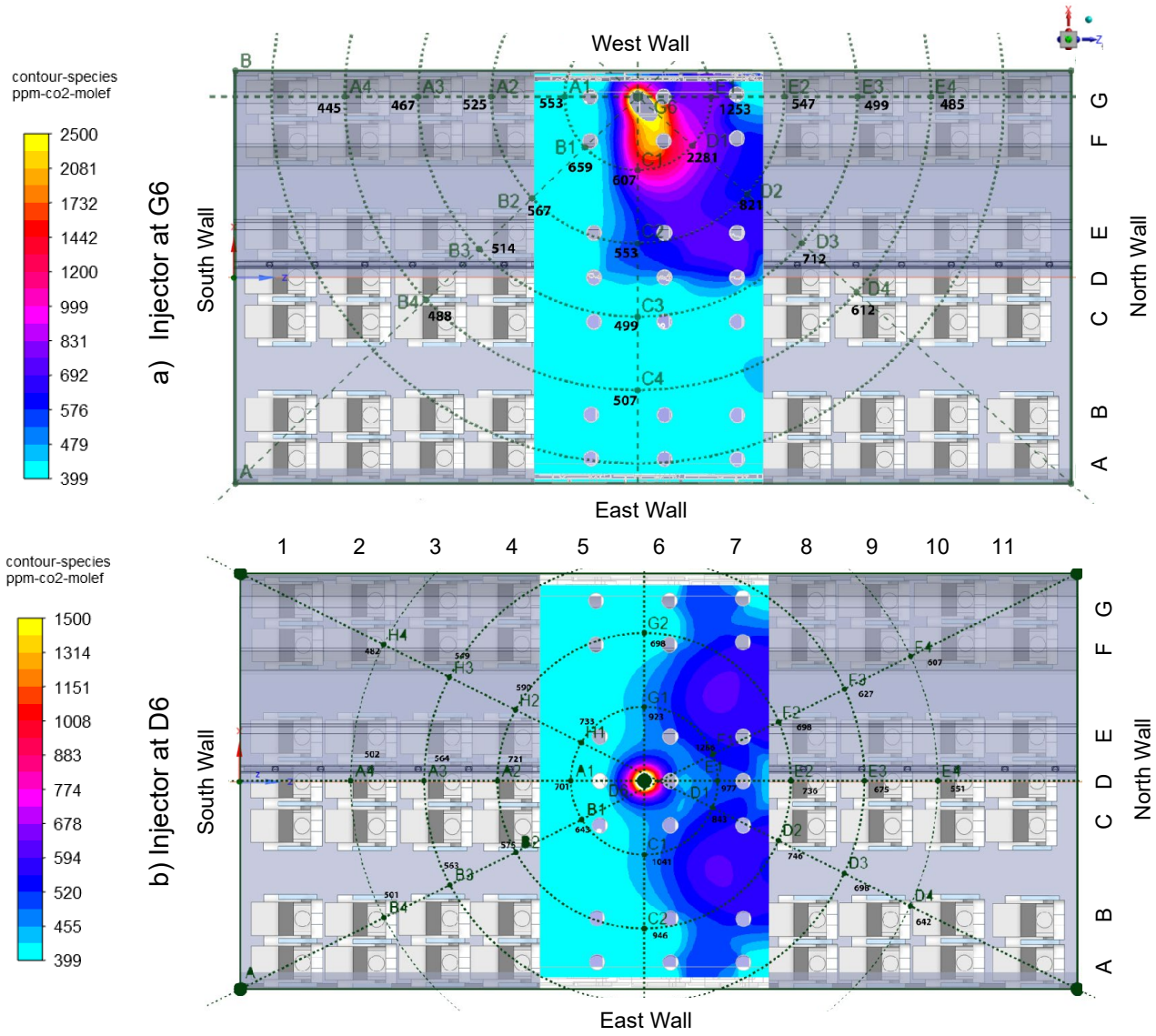

Figure 4-9. Gaspers off: Comparison of CO_2 molar fractions at breathing area injected at a) side, and b) center.

4.3 Effect of gaspers

The impact of gaspers on the continuous injection of the tracer gas was studied as well as the variation in velocity direction, using the same mesh (for each inclination), by adjusting the velocity components at the boundary conditions dialog box. The tested velocity inclinations were as follows: normal to the surface where the gaspers were in, at an inclination of $45°$ and $60°$ with the *XZ* plane. The gaspers were only tilted across the *YZ* plane, and this inclination can be observed in Figure 4-11 d) and e). Similarly to the approach followed in the previous subsection, the molar fraction of CO_2 was plotted at different planes. The side plane *YZ* is shown in Figure 4-10 a) b), and c), together with Figure 4-11 d), e) and f); the frontal plane *XY* is portrayed in Figure 4-10 d), e), and f) together with Figure 4-11 a), b), and c); the breathing area $y = 1.25$ m plane is depicted in Figure 4-12

When the gasper was tilted, there was a significant amount of momentum added to the longitudinal direction, which transported the contaminant to the back row, while the vertical velocity was not enough to overcome the buoyancy of the thermal plumes, thus allowing the contaminant to dissipate upwards but closer to the seating passengers. This can be desirable because of the counterclockwise circulation

that will act pushing the contaminant to the storage bin. However, when injected at the side of the cabin, the close proximity to the ceiling remains to be detrimental, thereby increasing the concentration of contaminant at the 7th row.

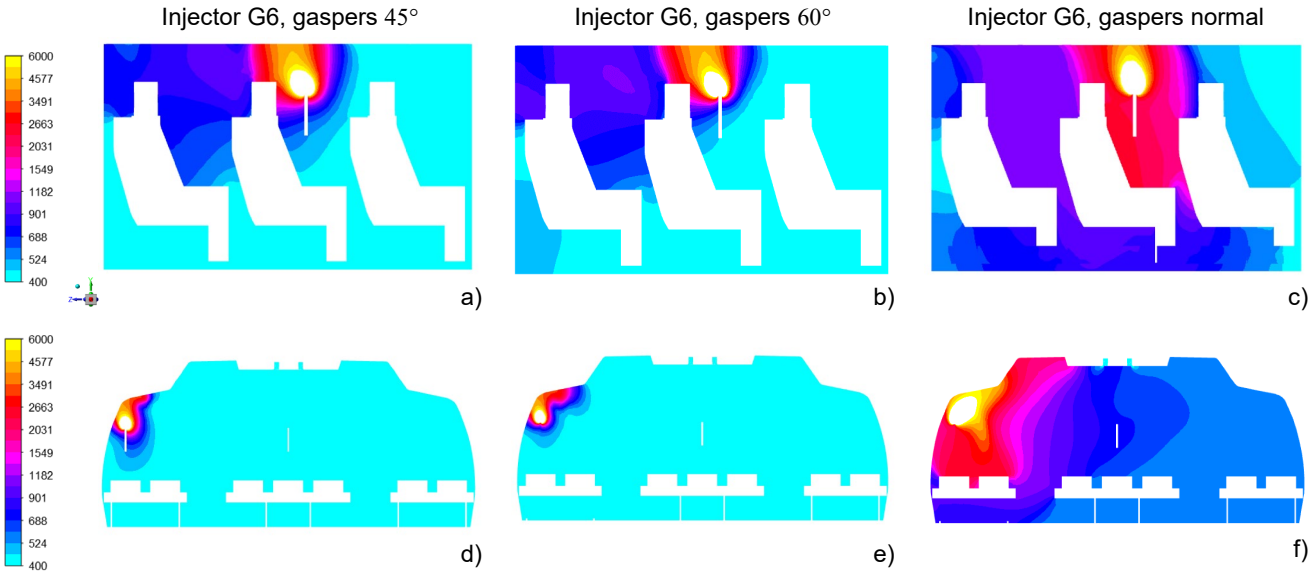

Figure 4-10. Gaspers on and injection at G6: molar fraction of CO_2 in ppm at front a)-c) and side d)-f) planes.

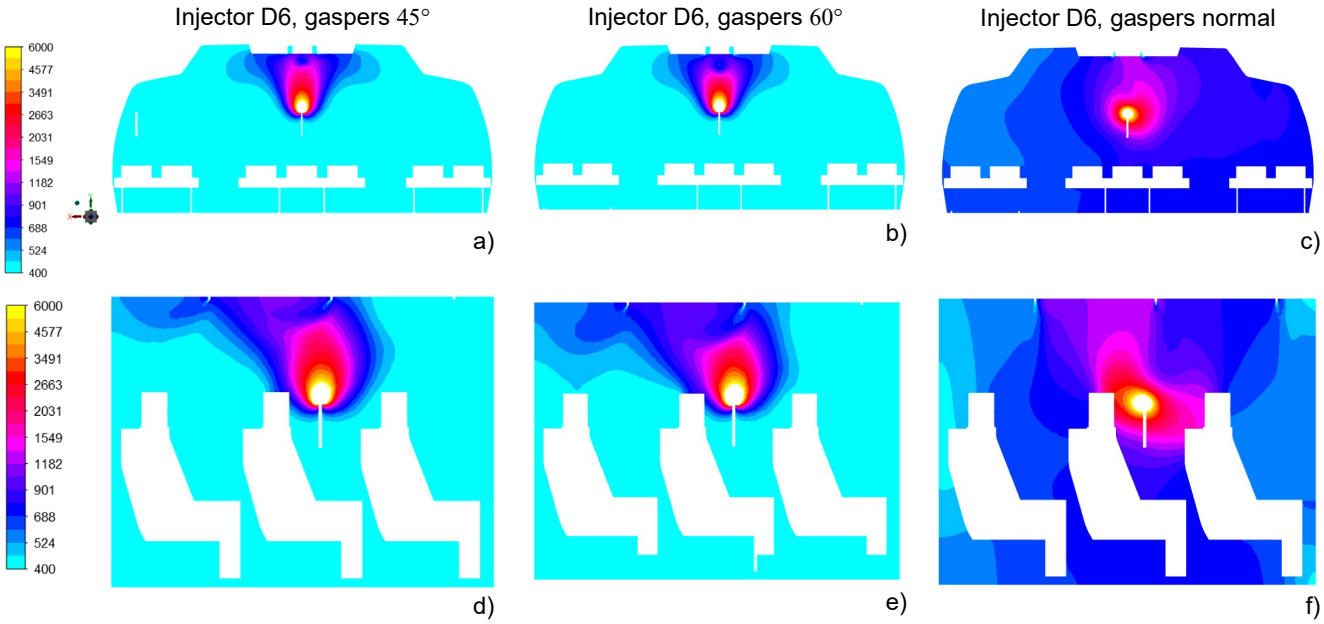

Figure 4-11. Gaspers on and injection at D6: comparison of CO_2 molar fractions for different gasper settings at front a)-c) and side d)-f) planes.

By analyzing Figure 4-12 one creates the perception that the gaspers at the baseline experiment were tilted on the side passengers and normal to the surface in the center as shown in b) and g). Finally, when gaspers are normal to the surface, the concentration of CO_2 increases significantly because the upward current caused by thermal plume and the vortex are reduced by the gaspers cold jet. Conjugating these effects, the net result is the decrease of the convection transport, which will magnify the diffusion of the contaminant. Further research should be carried out to potentially create a protocol to fix the position of gaspers at the safest position.

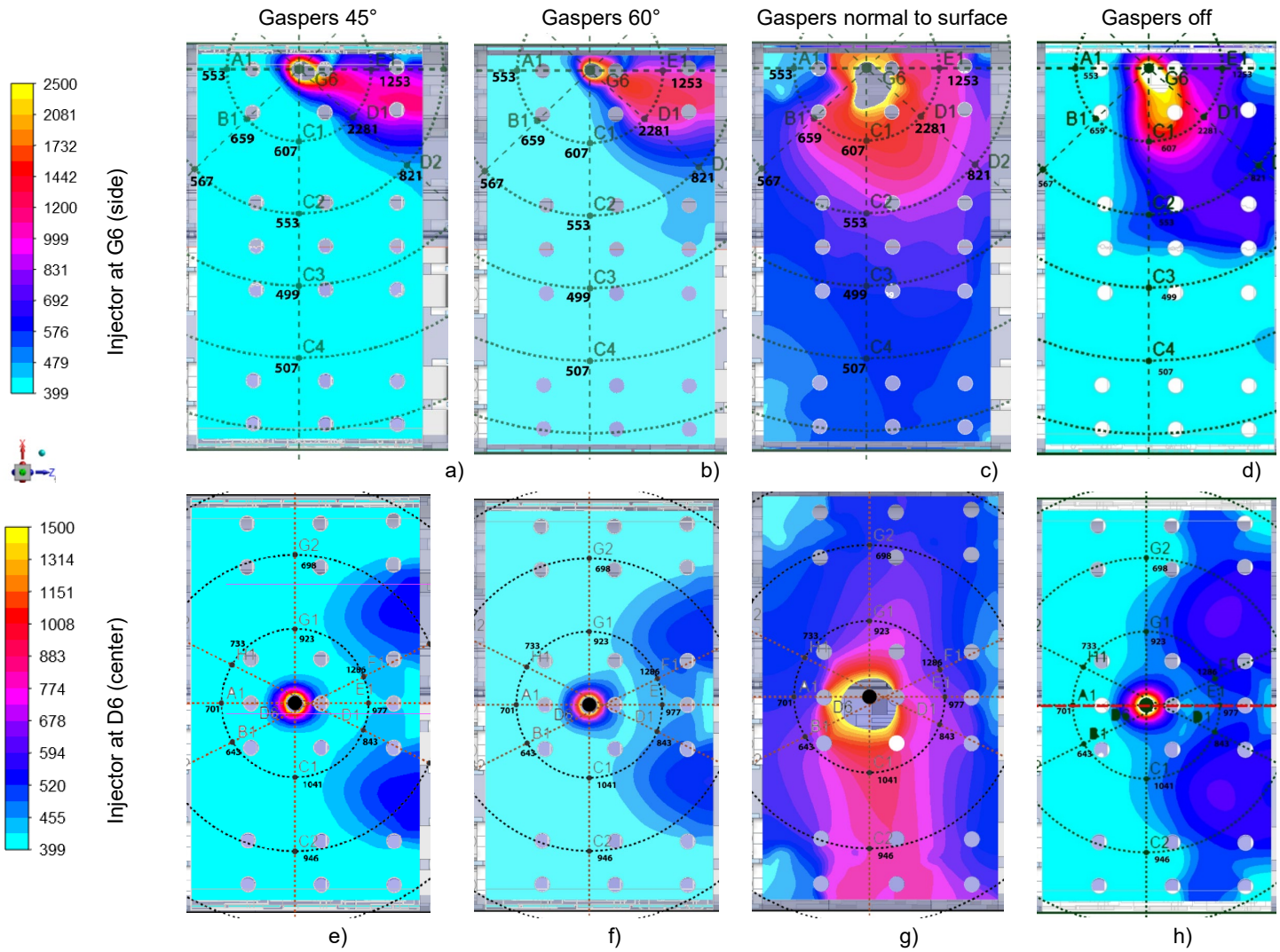

Figure 4-12. Comparison of CO_2 molar fractions for different gasper settings at the breathing area when the injector is at G6 a) to d) and at D6 e) to h).

4.4 Sensors Location

As stated in the literature review, sensors should be placed at locations with the highest concentration of contaminants. Figure 4-13 and Figure 4-14 show the 3D views of the CO_2 molar fractions at the walls in ppm for different gasper settings with injection at G6 and D6, respectively. From a) to d) the displayed surfaces are the walls containing seats and manikins, whereas e) to h) the cabin walls and outlets are overlayed. It can be seen in all figures that the CO_2 is pushed to the ceiling reaching around 5000 ppm when is injected at G6, and around 1000 ppm when injected at D6.

The second possible suitable location is at the backseat of the front seat. In this case, light aerosols would have very low concentration, however, such place might be a good candidate for larger droplets collection.

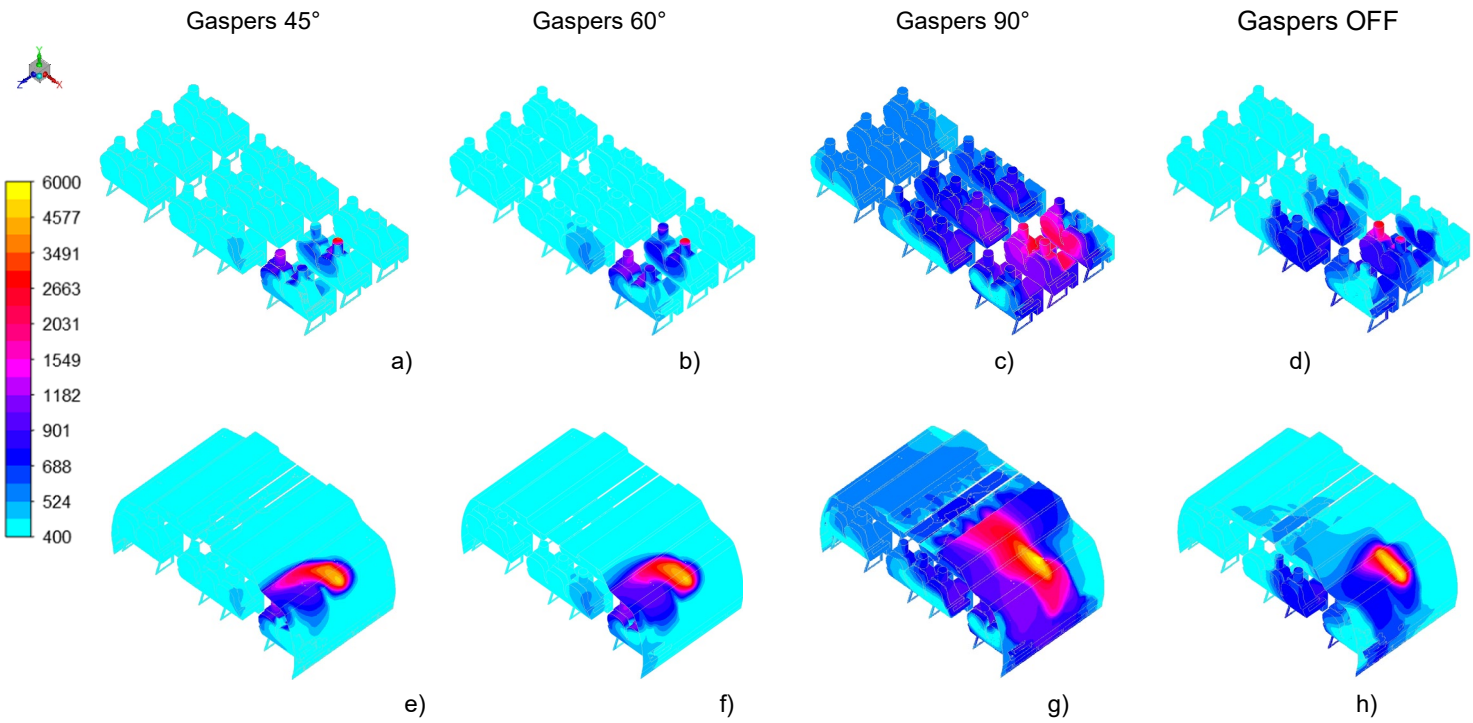

Figure 4-13. Comparison of CO_2 molar fractions for different gasper settings 3D view, injector at G6.

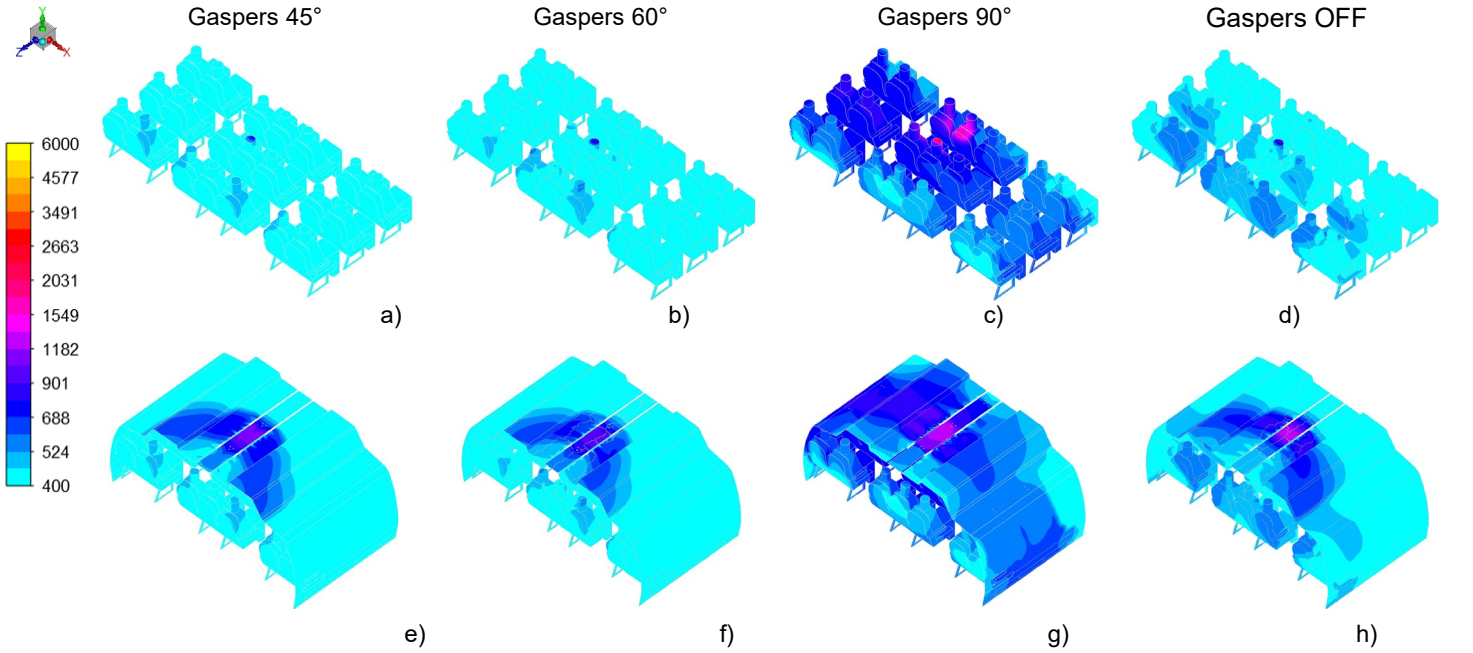

Figure 4-14. Comparison of CO_2 molar fractions for different gasper settings 3D view, injector at D6.

5 Conclusions

The present work firstly modeled the mockup 767 cabin of KSU using available geometry data.

This allowed to greatly improve the accuracy of the boundary conditions in the aircraft cabin by simulating the complex behavior of the air jets upstream the slot area using a modified RANS realizable k-ε model, which has demonstrated to produce a good agreement with available experimental data.

The model established for the air flow simulation subsequently allowed to also simulate a continuous injection source of a contaminant at the center and at the side of the cabin. In the absence of gaspers, the concentration of the contaminant is higher near the ceiling walls due to the thermal plumes.

When gaspers were added, the inclination of the gasper was crucial for determining the fate of the contaminant. By activating the gaspers normal to the ceilings, the combination of the cold jet with the thermal plume leads to a scenario closer to still air, whereas the longitudinal velocity remained small, thus leading to a decrease in longitudinal spread and increasing diffusion.

When gaspers were tilted to the manikin, there is a significant increase in longitudinal velocity without a major decrease in strength of the thermal plume. Furthermore, turning on gaspers reduced the flow rate available to the supply air. This decreased the strength of the global designed pattern, thus limiting the control the designer intended.

Using the present models, inspection of wall contamination contours suggest that the best places to install sensors would be on the ceiling right above the passenger, and in the backseat surface of the front seat.

6 Future Research

Future research should be focused on continuing to improve the accuracy of simulations by modeling the true geometry of the ventilation system. To do this the industry should be encouraged to share data with the academic community by taking the necessary precautions. Experimental researchers that have access to mockup cabins are encouraged to publish photos and dimensions of their facility at their website or social media like ResearchGate.

Using the same cabin of KSU, the new diffuser configuration could be tried, which is simpler to model and produce different airflow patterns. Then, these two configurations could be compared to analyze which one is the best in terms of overall air quality and which one exhibits lower contamination concentrations.

To better assess the fidelity of the numerical simulations, it would be very helpful to have videos showing fume particles getting out of the diffuser to see how the Coanda effect is behaving. To improve the turbulence modeling, more complex models should be tried, such as LES and DES, assuming that the required computational resources can be made available for this purpose.

To decrease the number of elements used in this simulation, thus allowing to reduce the computational demands, one could try to isolate the domain above the slot, which can be done by saving the profiles of pressure, temperature, turbulent kinetic energy and dissipation. That simulation could be run against these results and compared with it for validation.

Besides the change in the volumetric flow rate due to the CFR requirements, the change of pressure from ground to typical cruise cabin pressure will impact the properties of air and the partial pressure of its components. For precise simulations of respiratory events this would be necessary to study the partial pressure of oxygen in alveoli. Furthermore, the cabin average temperature has been reported from 17 °C to 31 °C. This will affect the thermal plumes behavior and possibly affect the contaminants. Studying this could help decide guidelines for temperature regulations.

Further research should be conducted to assess how this model runs against the experimental data of TRANSCOM report, which would require taking a Lagrangian approach to model particle transport and transient flow for respiratory events.

It would be also interesting to analyze the effect of gaspers on the respiratory events and determine if there is a configuration that could minimize the risk of airborne aerosols penetrating the breathing area.

7 Bibliography

[1] ICAO. Effects of Novel Coronavirus (COVID-19) on Civil Aviation: Economic Impact Analysis. *Economic Development.* https://www.icao.int/sustainability/Documents/COVID-19/ICAO_Coronavirus_Econ_Impact.pdf (2022).

[2] IATA. Cabin Air & Low Risk of On Board Transmission. https://www.iata.org/en/youandiata/travelers/health/low-risk-transmission/.

[3] Raposo, C. L. S. & Sousa, J. M. M. Computational Study of Airflow and Dispersion of Airborne Pathogens inside an Aircraft Cabin. In *33rd Congress of the International Council of the Aeronautical Sciences* (2022). https://doi.org/10.5281/zenodo.7086739.

[4] Hunt, E. H., Reid, D. H., Space, D. R. & Tilton, F. E. Commercial Airliner Environmental Control System - Engineering Aspects of Cabin Air Quality. In *Aerospace Medical Association annual meeting* 1–8 (1995). At https://web.archive.org/web/20110629010243/http:/www.boeing.com/commercial/cabinair/ecs.pdf

[5] ASHRAE. *Air Quality within Commercial Aircraft Standard 161*. (2018).

[6] National Research Council. *The Airliner Cabin Environment and the Health of Passengers and Crew*. (National Academies Press, 2002). https://doi.org/10.17226/10238.

[7] ASHRAE. *Air Quality Within Commercial Aircraft Guideline 28*. (2021).

[8] Michaelis, Susan. Health and Flight Safety Implications from Exposure to Contaminated Air in Aircraft (PhD Thesis). (The University of New South Wales, 2010). At https://doi.org/10.26190/unsworks/23524

[9] Michaelis, Susan. Implementation of the requirements for the provision of clean air in crew and passenger compartments using the aircraft bleed air system (MSc. Thesis). (Cranfield University, 2016).

[10] Scholz, D. Routes of Aircraft Cabin Air Contamination from Engine Oil, Hydraulic and Deicing Fluid. *INCAS Bull.* **14**, 153–170 (2022) At https://doi.org/10.13111/2066-8201.2022.14.1.13.

[11] Scholz, D. *Aircraft Cabin Ventilation in the Corona Pandemic – Legend and Truth*. *Hamburg Aerospace Lecture Series* HAW Hamburg (2021). https://doi.org/10.5281/zenodo.5356569.

[12] Hunt, E. H. & Space, D. R. The Airplane Cabin Environment – Issues Pertaining to Flight Attendant Comfort. In *International In-Flight Service Management Organization Conference* 1–12 (1994). At https://web.archive.org/web/20011205062027/http://www.boeing.com/commercial/cabinair/ventilation.pdf

[13] Davis, A. C., Zee, M., Clark, A. D., *et al.* Computational Fluid Dynamics Modeling of Cough Transport in an Aircraft Cabin. *Sci. Rep.* **11**, (2021) At https://doi.org/10.1038/s41598-021-02663-8.

[14] Airbus. Keep Trust in Air Travel. (2020) https://www.iata.org/contentassets/a1a361594bb440b1b7ebb632355373d1/airbus-trust-airtravel.pdf

[15] Zhai, Z. J., Zhang, Z., Zhang, W. & Chen, Q. Y. Evaluation of Various Turbulence Models in Predicting Airflow and Turbulence in Enclosed Environments by CFD: Part 1—Summary of Prevalent Turbulence Models. *HVAC R Res.* **13**, 853–870 (2007) At https://doi.org/10.1080/10789669.2007.10391459.

[16] Elmaghraby, H. A., Chiang, Y. W. & Aliabadi, A. A. Ventilation strategies and air quality management in passenger aircraft cabins: A review of experimental approaches and numerical simulations. *Sci. Technol. Built Environ.* **24**, 160–175 (2018) At https://doi.org/10.1080/23744731.2017.1387463.

[17] Zhang, T. T., Li, P., Zhao, Y. & Wang, S. Various air distribution modes on commercial airplanes. Part 1: Experimental measurement. *HVAC R Res.* **19**, 268–282 (2013) At https://doi.org/10.1080/10789669.2013.765241.

[18] Hinds, W. C. *Aerosol technology : properties, behavior, and measurement of airborne particles*. (John Wiley & Sons, Inc., 1999).

[19] Tu, J., Inthavong, K. & Ahmadi, G. *Computational Fluid and Particle Dynamics in the Human Respiratory System*. (Springer Netherlands, 2013). https://doi.org/10.1007/978-94-007-4488-2.

[20] Office of the Federal Register & National Archives and Records Administration. 40 CFR 51.100 Definitions. In *Code of Federal Regulations* 179–185 (2021).

[21] Environmental Protection Agency. Technical Overview of Volatile Organic Compounds. (2022).https://www.epa.gov/indoor-air-quality-iaq/technical-overview-volatile-organic-compounds

[22] Schuchardt, S., Bitsch, A., Koch, W. & Rosenberger, W. *Preliminary Cabin Air Quality Measurement Campaign*. *EASA* (2014). At https://www.easa.europa.eu/en/downloads/22219/en

[23] ASHRAE. Indoor environmental health. In *2021 ASHRAE Handbook - Fundamentals* (ed. Kennedy, H. E.) (2021).

[24] Mangili, A. & Gendreau, M. A. Transmission of infectious diseases during commercial air travel. *Lancet* **365**, 989–996 (2005) At https://doi.org/10.1016/S0140-6736(05)71089-8.

[25] Moser, M. R., Bender, T. R., Margolis, H. S., *et al.* An Outbreak of Influenza aboard a Commercial airliner. *Am. J. Epidemiol.* **110**, 1–6 (1979) At https://doi.org/10.1093/oxfordjournals.aje.a112781.

[26] Olsen, S. J., Chang, H.-L., Cheung, T. Y.-Y., *et al.* Transmission of the Severe Acute Respiratory Syndrome on Aircraft. *N. Engl. J. Med.* **349**, 2416–2422 (2003) At https://doi.org/10.1056/NEJMoa031349.

[27] Flaherty, G. T., Hamer, D. H. & Chen, L. H. Travel in the Time of COVID: A Review of International Travel Health in a Global Pandemic. *Curr. Infect. Dis. Rep.* **24**, 129–145 (2022) At https://doi.org/10.1007/s11908-022-00784-3.

[28] National Academies of Sciences Engineering and Medicine. *Infectious Disease Mitigation in Airports and on Aircraft*. *Infectious Disease Mitigation in Airports and on Aircraft* (National Academies Press, 2013). https://doi.org/10.17226/22512.

[29] Cao, X., Zevitas, C. D., Spengler, J. D., *et al.* The on-board carbon dioxide concentrations and ventilation performance in passenger cabins of US domestic flights. *Indoor Built Environ.* **28**, 761–771 (2019) At https://doi.org/10.1177/1420326X18793997.

[30] Rabaan, A. A., Al-Ahmed, S. H., Al-Malkey, M. K., *et al.* Airborne transmission of SARS-CoV-2 is the dominant route of transmission: Droplets and aerosols. *Infez. Med.* **29**, 10–19 (2021) At https://doi.org/10779/rcsi.19139831.v2 .

[31] National Academies of Sciences Engineering and Medicine. *Flying in the COVID-19 Era : Science-based Risk Assessments and Mitigation Strategies on the Ground and in the Air : Proceedings of a Workshop (2022)*. (The National Academies Press, 2022). https://doi.org/10.17226/26426.

[32] Shehadi, M. F. Air Quality and Airflow Characteristic Studies for Passenger Aircraft Cabins. In *Indoor Environment and Health* (IntechOpen, 2019). https://doi.org/10.5772/intechopen.87307.

[33] Liu, W., Mazumdar, S., Zhang, Z., *et al.* State-of-the-art methods for studying air distributions in commercial airliner cabins. *Build. Environ.* **47**, 5–12 (2012) At https://doi.org/10.1016/j.buildenv.2011.07.005.

[34] Li, J., Cao, X., Liu, J., Wang, C. & Zhang, Y. Global airflow field distribution in a cabin mock-up measured via large-scale 2D-PIV. *Build. Environ.* **93**, 234–244 (2015) At https://doi.org/10.1016/j.buildenv.2015.06.030.

[35] Pan, Y., Lin, C.-H., Wei, D. & Chen, C. Influence of surface roughness on particle deposition distribution around multi-slot cabin supply air nozzles of commercial airplanes. *Build. Environ.* **176**, 106870 (2020) At https://doi.org/10.1016/j.buildenv.2020.106870.

[36] Liu, M., Chang, D., Liu, J., *et al.* Experimental investigation of air distribution in an airliner cabin mockup with displacement ventilation. *Build. Environ.* **191**, 107577 (2021) At https://doi.org/10.1016/j.buildenv.2020.107577.

[37] You, R., Chen, J., Shi, Z., *et al.* Experimental and numerical study of airflow distribution in an aircraft cabin mock-up with a gasper on. *J. Build. Perform. Simul.* **9**, 555–566 (2016) At https://doi.org/10.1080/19401493.2015.1126762.

[38] You, R., Chen, J., Lin, C.-H., Wei, D. & Chen, Q. Y. Investigating the impact of gaspers on cabin air quality in commercial airliners with a hybrid turbulence model. *Build. Environ.* **111**, 110–122 (2017) At https://doi.org/10.1016/j.buildenv.2016.10.018.

[39] You, Ruoyu. Investigating Airflow Distribution and Contaminant Transport in Commercial Aircraft Cabins (PhD Thesis). (Purdue University, 2018). At https://docs.lib.purdue.edu/open_access_dissertations/2110

[40] Wang, C., Liu, J. & Zhang, Y. Accurate experimental measurements of flow boundary conditions for numerical simulations in an aircraft cabin mockup. In *13th International Conference on Indoor Air Quality and Climate 2014* 803–810 (2014). At https://www.researchgate.net/publication/287628124

[41] Cao, X., Liu, J., Pei, J., *et al.* 2D-PIV measurement of aircraft cabin air distribution with a high spatial resolution. *Build. Environ.* **82**, 9–19 (2014) At https://doi.org/10.1016/j.buildenv.2014.07.027.

[42] Li, M., Zhao, B., Tu, J. & Yan, Y. Study on the carbon dioxide lockup phenomenon in aircraft cabin by computational fluid dynamics. *Build. Simul.* **8**, 431–441 (2015) At https://doi.org/10.1007/s12273-015-0217-8.

[43] You, R., Zhang, Y., Zhao, X., *et al.* An innovative personalized displacement ventilation system for airliner cabins. *Build. Environ.* **137**, 41–50 (2018) At https://doi.org/10.1016/j.buildenv.2018.03.057.

[44] Li, M., Yan, Y., Zhao, B., *et al.* Assessment of turbulence models and air supply opening models for CFD modelling of airflow and gaseous contaminant distributions in aircraft cabins. *Indoor Built Environ.* **27**, 606–621 (2018) At https://doi.org/10.1177/1420326X16688049.

[45] Wang, C., Zhang, J., Chen, H. & Liu, J. Experimental study of thermo-fluid boundary conditions, airflow and temperature distributions in a single aisle aircraft cabin mockup. *Indoor Built Environ.* **30**, 1185–1199 (2020) At https://doi.org/10.1177/1420326X20932271.

[46] Zhao, Y., Liu, Z., Li, X., Zhao, M. & Liu, Y. A modified turbulence model for simulating airflow aircraft cabin environment with mixed convection. *Build. Simul.* **13**, 665–675 (2020) At https://doi.org/10.1007/s12273-020-0609-2.

[47] Li, X., Zhang, T. (Tim), Fan, M., *et al.* Experimental evaluation of particle exposure at different seats in a single-aisle aircraft cabin. *Build. Environ.* **202**, 108049 (2021) At https://doi.org/10.1016/j.buildenv.2021.108049.

[48] Cao, Q., Liu, M., Li, X., *et al.* Influencing factors in the simulation of airflow and particle transportation in aircraft cabins by CFD. *Build. Environ.* **207**, (2022) At https://doi.org/10.1016/j.buildenv.2021.108413.

[49] Mo, Hailong. Experimental and Computational Study of Interaction of Airflow Inside Aircraft Cabin with Human Body (PhD Thesis). (Kansas State University, 2002).

[50] Patel, Jignesh A. Experimental investigation of ventilation effectiveness in an airliner cabin mockup (MSc. Thesis). (Kansas State University, 2017). At http://hdl.handle.net/2097/35528

[51] Mahmoud, Seif. Experimental Analysis of aerosol dispersion and containment solutions in aircraft cabins (PhD Thesis). (Kansas State University, 2021). At https://hdl.handle.net/2097/41398

[52] Anderson, Michael D. Effect of gaspers on airflow patterns and the transmission of airborne contaminants within an aircraft cabin environment (MSc. Thesis). (Kansas State University, 2012). At http://hdl.handle.net/2097/14988

[53] Shehadi, Maher F. Experimental investigation of optimal particulate sensor location in an aircraft cabin (MSc. Thesis). (Kansas State University, 2010). At http://hdl.handle.net/2097/3877

[54] Ebrahimi, K., Hosni, M. H. & Zheng, Z. C. Computational Study of Turbulent Airflow in a Full-Scale Aircraft Cabin Mockup - Part 1: Determination of Boundary Conditions at the Outlet of Air Diffusers. In *ASME 2013 Fluids Engineering Division Summer Meeting* vol. 1 A (2013). At https://doi.org/10.1115/FEDSM2013-16564

[55] Beneke, Jeremy M. Small Diameter Particle Dispersion in a Commercial Aircraft Cabin (MSc. Thesis). (Kansas State University, 2010). At http://hdl.handle.net/2097/4150

[56] Sun, Y., Zhang, Y., Wang, A., Topmiller, J. L. & Bennett, J. S. Experimental characterization of airflows in aircraft cabins, Part I: Experimental system and measurement procedure. *ASHRAE Trans.* **111**, 45–52 (2005) At https://www.researchgate.net/publication/279541260

[57] Sun, Y., Zhang, Y., Wang, A., Topmiller, J. L. & Bennett, J. S. Experimental characterization of airflows in aircraft cabins, Part II: Results and Research Recommendations. *ASHRAE Trans.* **111**, 53–59 (2005) At https://www.researchgate.net/publication/279907783

[58] Wang, A., Zhang, Y. & Sun, Y. Streak recognition for a three-dimensional volumetric particle tracking velocimetry system. *ASHRAE Trans.* **111**, 476–484 (2005) At https://www.researchgate.net/publication/279543674

[59] Wang, A., Zhang, Y., Topmiller, J. L., Bennett, J. S. & Dunn, K. H. Tracer study of airborne transmission in an aircraft cabin mock-up. *ASHRAE Trans.* **112**, 697–705 (2006) At https://www.researchgate.net/publication/287721570

[60] Wang, Aijun. Quantifying air distribution, ventilation effectiveness and airborne pollutant transport in an aircraft cabin mockup (PhD Thesis). (University of Illinois, 2006). At http://hdl.handle.net/2142/86064

[61] Wang, A., Zhang, Y., Sun, Y. & Wang, X. Experimental study of ventilation effectiveness and air velocity distribution in an aircraft cabin mockup. *Build. Environ.* **43**, 337–343 (2008) At https://doi.org/10.1016/j.buildenv.2006.02.024.

[62] Yan, Wei. Development of Hybrid Particle Tracking Algorithms and their Applications in Airflow Measurement within an Aircraft Cabin Mock-Up (PhD Thesis). (University of Illinois, 2010). At http://hdl.handle.net/2142/18317

[63] Bennett, J. S., Jones, B. W., Hosni, M. H., *et al.* Airborne exposure patterns from a passenger source in aircraft cabins. *HVAC R Res.* **19**, 962–973 (2013) At https://doi.org/10.1080/10789669.2013.838990.

[64] Zukowska, D., Strøm-Tejsen, P., Jama, A. & Wyon, D. P. Correlation between subjective assessments of local thermal discomfort and thermal manikin measurements in a simulated aircraft cabin. In *International Conference on Energy Efficient Technologies in Indoor Environment* 1–12 (2005). At https://www.researchgate.net/publication/242284527

[65] Strøm-Tejsen, P., Wyon, D. P., Lagercrantz, L. & Fang, L. Passenger evaluation of the optimum balance between fresh air supply and humidity from 7-h exposures in a simulated aircraft cabin. *Indoor Air* **17**, 92–108 (2007) At https://doi.org/10.1111/j.1600-0668.2006.00458.x.

[66] Sze To, G. N., Wan, M. P., Chao, C. Y. H., Fang, L. & Melikov, A. Experimental Study of Dispersion and Deposition of Expiratory Aerosols in Aircraft Cabins and Impact on Infectious Disease Transmission. *Aerosol Sci. Technol.* **43**, 466–485 (2009) At https://doi.org/10.1080/02786820902736658.

[67] Wan, M. P., Sze To, G. N., Chao, C. Y. H., Fang, L. & Melikov, A. Modeling the Fate of Expiratory Aerosols and the Associated Infection Risk in an Aircraft Cabin Environment. *Aerosol Sci. Technol.* **43**, 322–343 (2009) At https://doi.org/10.1080/02786820802641461.

[68] Zhang, T. T., Chen, Q. Y. & Lin, C.-H. Optimal sensor placement for airborne contaminant detection in an aircraft cabin. *HVAC R Res.* **13**, 683–696 (2007) At https://doi.org/10.1080/10789669.2007.10390980.

[69] Zhang, Tengfei. Detection and Mitigation of Contaminant Transport in Commercial Aircraft Cabins (PhD Thesis). (Purdue University, 2007). At https://docs.lib.purdue.edu/dissertations/AAI3287235/

[70] Zhang, Z., Chen, X., Mazumdar, S., Zhang, T. T. & Chen, Q. Y. Experimental and numerical investigation of airflow and contaminant transport in an airliner cabin mockup. *Build. Environ.* **44**, 85–94 (2009) At https://doi.org/10.1016/j.buildenv.2008.01.012.

[71] Zhang, T. T., Li, P. & Wang, S. A personal air distribution system with air terminals embedded in chair armrests on commercial airplanes. *Build. Environ.* **47**, 89–99 (2012) At https://doi.org/10.1016/j.buildenv.2011.04.035.

[72] Poussou, Stephane B. Experimental Investigation of Airborne contaminant Transport by a Human Wake Moving in a Ventilated Aircraft Cabin (PhD Thesis). (Purdue University, 2008). At https://docs.lib.purdue.edu/dissertations/AAI3373218/

[73] Mazumdar, Sagnik. Transmission of Airborne Contaminants of Airliner Cabins (PhD Thesis). (Purdue University, 2009). At https://docs.lib.purdue.edu/dissertations/AAI3403133/

[74] Dygert, Ryan K. Mitigation of cross-contamination in an aircraft cabin through the use of localized exhaust (PhD Thesis). (Syracuse University, 2010). At https://surface.syr.edu/mae_etd/55

[75] Garner, R. P., Wong, K. L., Ericson, S. C., Baker, A. J. & Orzechowski, J. A. *CFD Validation for Contaminant Transport in Aircraft Cabin Ventilation Flow Fields*. DOT/FAA/AM-04/7 FAA Civil Aerospace Medical Institute (2004). At https://www.researchgate.net/publication/235110873

[76] Baker, A. J., Ericson, S. C., Orzechowski, J. A., Wong, K. L. & Garner, R. P. *Validation for CFD Prediction of Mass Transport in an Aircraft Passenger Cabin*. DOT/FAA/AM-06/27 Office of Aerospace Medicine FAA (2006). At https://www.researchgate.net/publication/238088961

[77] Volavý, F., Fišer, J. & Nöske, I. Prediction of air temperature in the aircraft cabin under different operational conditions. *EPJ Web Conf.* **45**, 1–6 (2013) At https://doi.org/10.1051/epjconf/20134501096.

[78] Norrefeldt, V., Mayer, F., Herbig, B., *et al.* Effect of increased cabin recirculation airflow fraction on relative humidity, CO2 and TVOC. *Aerospace* **8**, 1–16 (2021) At https://doi.org/10.3390/aerospace8010015.

[79] Dechow, M., Sohn, H. & Steinhanses, J. Concentrations of selected contaminants in cabin air of Airbus aircrafts. *Chemosphere* **35**, 21–31 (1997) At https://doi.org/10.1016/S0045-6535(97)00135-5.

[80] Bosbach, J., Heider, A., Dehne, T., *et al.* Evaluation of Cabin Displacement Ventilation under Flight Conditions. In *28th International Congress of the Aeronautical Sciences ICAS2012* 1–10 (2012). At https://www.researchgate.net/publication/225007686

[81] Dehne, T. & Bosbach, J. Comparison of surface temperatures and cooling rates for different ventilation concepts in an A320 aircraft cabin under flight conditions. *Roomvent 2014 13th SCANVAC Int. Conf. Air Distrib. Rooms* (2014) At https://www.researchgate.net/publication/265554415.

[82] Du, X., Li, B., Liu, H., *et al.* Effect of nozzle air supply temperature and volume flowrate on the jet flow from a typical ventilation nozzle in aircraft cabins. *Indoor Built Environ.* **27**, 499–511 (2018) At https://doi.org/10.1177/1420326X16676881.

[83] Fang, Z., Liu, H., Li, B., *et al.* Experimental investigation of personal air supply nozzle use in aircraft cabins. *Appl. Ergon.* **47**, 193–202 (2015) At https://doi.org/10.1016/j.apergo.2014.09.011.

[84] Bosbach, J., Kühn, M., Rütten, M. & Wagner, C. Mixed Convection in a Full Scale Aircraft Cabin Mock-Up. In *25th Congress of the International Council of the Aeronautical Sciences 2006* vol. 6 3723–3731 (2006). At https://www.researchgate.net/publication/225018640

[85] Bosbach, J., Pennecot, J., Wagner, C., *et al.* Experimental and numerical simulations of turbulent ventilation in aircraft cabins. *Energy* **31**, 694–705 (2006) At https://doi.org/10.1016/j.energy.2005.04.015.

[86] Günther, G., Bosbach, J., Pennecot, J., *et al.* Experimental and numerical simulations of idealized aircraft cabin flows. *Aerosp. Sci. Technol.* **10**, 563–573 (2006) At https://doi.org/10.1016/j.ast.2006.02.003.

[87] Chen, W., Liu, J., Li, F., *et al.* Ventilation similarity of an aircraft cabin mockup with a real MD-82 commercial airliner. *Build. Environ.* **111**, 80–90 (2017) At https://doi.org/10.1016/j.buildenv.2016.10.017.

[88] Liu, W., Wen, J., Chao, J., *et al.* Accurate and high-resolution boundary conditions and flow fields in the first-class cabin of an MD-82 commercial airliner. *Atmos. Environ.* **56**, 33–44 (2012) At https://doi.org/10.1016/j.atmosenv.2012.03.039.

[89] Liu, W., Wen, J., Lin, C.-H., *et al.* Evaluation of various categories of turbulence models for predicting air distribution in an airliner cabin. *Build. Environ.* **65**, 118–131 (2013) At https://doi.org/10.1016/j.buildenv.2013.03.018.

[90] Cao, Q., Chen, C., Liu, S., *et al.* Prediction of particle deposition around the cabin air supply nozzles of commercial airplanes using measured in-cabin particle emission rates. *Indoor Air* **28**, 852–865 (2018) At https://doi.org/10.1111/ina.12489.

[91] You, R., Liu, W., Chen, J., *et al.* Predicting airflow distribution and contaminant transport in aircraft cabins with a simplified gasper model. *J. Build. Perform. Simul.* **9**, 699–708 (2016) At https://doi.org/10.1080/19401493.2016.1196730.

[92] Ebrahimi, K., Zheng, Z. C. & Hosni, M. H. LES and RANS Simulation of Turbulent Airflow and Tracer Gas Injection in a Generic Aircraft Cabin Model. In *ASME 2010 3rd Joint US-European Fluids Engineering Summer Meeting: Volume 1, Symposia – Parts A, B, and C* vol. 1 227–240 (ASMEDC, 2010). At https://www.researchgate.net/publication/260165305

[93] Ebrahimi, Khosrow. Numerical Simulation of turbulent airflow, tracer gas diffusion, and particle dispersion in a mockup aircraft cabin (PhD Thesis). (Kansas State University, 2012). At http://hdl.handle.net/2097/13609

[94] Padilla, Angelina M. Experimental Analysis of Particulate Movement in a Large Eddy Simulation Chamber (MSc. Thesis). (Kansas State University, 2008). At http://hdl.handle.net/2097/786

[95] Lebbin, Paul A. Experimental and Numerical Analysis of Air, Tracer gas, and particulate movement in a large eddy simulation chamber (PhD Thesis). (Kansas State University, 2006).

[96] Lin, C.-H., Dunn, K. H., Horstman, R. H., *et al.* Numerical Simulation of Airflow and Airborne Pathogen Transport in Aircraft Cabins - Part I: Numerical Simulation of the Flow Field. *ASHRAE Trans.* **111**, 755–764 (2005)

[97] Research Facilities Navigator. Centre for Air Travel Research (CATR). (2022).https://navigator.innovation.ca/en/facility/national-research-council-canada/centre-air-travel-research-catr

[98] Lange, P., Dehne, T., Schmeling, D., Dannhauer, A. & Gores, I. Realistic flight conditions on ground: new research facility for cabin ventilation. *CEAS Aeronaut. J.* (2022) At https://doi.org/10.1007/s13272-022-00594-2.

[99] Nene, R. R., Moran, B. D., Roberson, D. R. & Braaten, N. T. *Clean Airplane Program – Live Virus Validation Testing*. Boeing (2020). At https://www.boeing.com/confident-travel/downloads/Boeing_Clean_Airplane_Program_Live_Virus_Validation_Testing.pdf

[100] Müller, R. H. G., Scherer, T., Rötger, T., Schaumann, O. & Markwart, M. Large Body Aircraft Cabin A/C Flow Measurement by Helium Bubble Tracking. *J. Flow Vis. Image Process.* **4**, 295–306 (1997) At https://doi.org/10.1615/JFlowVisImageProc.v4.i3.90.

[101] Spicer, C. W., Murphy, M. J., Holdren, M. W., *et al. Relate air quality and other factors to comfort and health symptoms reported by passengers and crew on commercial transport aircraft (Part I)*. RP-1262 Part 1 ASHRAE (2004). At https://www.researchgate.net/publication/267221849

[102] Gupta, Jitendra K. Respiratory Exhalation/Inhalation Models and Prediction of Airborne Infection Risk in an Aircraft Cabin (PhD Thesis). (Purdue University, 2010). At https://docs.lib.purdue.edu/dissertations/AAI3449758/

[103] Lin, C.-H., Horstman, R. H., Ahlers, M. F., *et al.* Numerical Simulation of Airflow and Airborne Pathogen Transport in Aircraft Cabins - Part II: Numerical simulation of Airborne Pathogen Transport. *ASHRAE Trans.* **111**, 764–768 (2005) At https://www.researchgate.net/publication/279704592.

[104] Chen, Q. Y. & Zhang, Z. Prediction of particle transport in enclosed environment. *China Particuology* **3**, 364–372 (2005) At https://doi.org/10.1016/s1672-2515(07)60216-4.

[105] Zhang, T. T. & Chen, Q. Y. Novel air distribution systems for commercial aircraft cabins. *Build. Environ.* **42**, 1675–1684 (2007) At https://doi.org/10.1016/j.buildenv.2006.02.014.

[106] Gao, N. P. & Niu, J. L. Personalized Ventilation for Commercial Aircraft Cabins. *J. Aircr.* **45**, 508–512 (2008) At https://doi.org/10.2514/1.30272.

[107] Zhang, T. T., Yin, S. & Wang, S. An under-aisle air distribution system facilitating humidification of commercial aircraft cabins. *Build. Environ.* **45**, 907–915 (2010) At https://doi.org/10.1016/j.buildenv.2009.09.010.

[108] Yan, W., Zhang, Y., Sun, Y. & Li, D. Experimental and CFD study of unsteady airborne pollutant transport within an aircraft cabin mock-up. *Build. Environ.* **44**, 34–43 (2009) At https://doi.org/10.1016/j.buildenv.2008.01.010.

[109] Gupta, J. K., Lin, C.-H. & Chen, Q. Y. Transport of expiratory droplets in an aircraft cabin. *Indoor Air* **21**, 3–11 (2011) At https://doi.org/10.1111/j.1600-0668.2010.00676.x.

[110] Isukapalli, S. S., Mazumdar, S., George, P., *et al.* Computational fluid dynamics modeling of transport and deposition of pesticides in an aircraft cabin. *Atmos. Environ.* **68**, 198–207 (2013) At https://doi.org/10.1016/j.atmosenv.2012.11.019.

[111] Cao, X., Li, J., Liu, J. & Yang, W. 2D-PIV measurement of isothermal air jets from a multi-slot diffuser in aircraft cabin environment. *Build. Environ.* **99**, 44–58 (2016) At https://doi.org/10.1016/j.buildenv.2016.01.018.

[112] Pan, Y., Lin, C.-H., Wei, D., Dong, Z. & Chen, C. Computer-aided design of a new cabin supply air nozzle in commercial airplanes for reducing particle deposition. *Build. Environ.* **186**, 107324 (2020) At https://doi.org/10.1016/j.buildenv.2020.107324.

[113] Topp, C., Hesselholt, P., Trier, M. R. & Nielsen, P. V. Influence of geometry of thermal manikins on room airflow. In *Healthy Buildings 2003, the 7th ISIAQ International Conference* vol. 2 339–344 (2003). At http://homes.civil.aau.dk/pvn/cfd-benchmarks/csp_literature/Before_2004/Topp_C_et_al_2003B.pdf

[114] Yan, W., Yang, X. & Shan, M. How to simplify computer simulated persons (CSPs) for modeling personal microenvironments: Comparison and case studies. *ASHRAE Trans.* **115 PART 1**, 473–483 (2009) At https://www.researchgate.net/publication/287702564.

[115] Yan, Y., Li, X. & Tu, J. Effects of manikin model simplification on CFD predictions of thermal flow field around human bodies. *Indoor Built Environ.* **26**, 1185–1197 (2017) At https://doi.org/10.1177/1420326X16653500.

[116] Li, J., Cao, X., Liu, J., Mohanarangam, K. & Yang, W. PIV measurement of human thermal convection flow in a simplified vehicle cabin. *Build. Environ.* **144**, 305–315 (2018) At https://doi.org/10.1016/j.buildenv.2018.08.031.

[117] Murota, K., Kang, Y., Hyodo, S., *et al.* Hygro-thermo-chemical transfer analysis of clothing microclimate using three-dimensional digital clothing model and computer-simulated person. *Indoor Built Environ.* **0**, 1–18 (2022) At https://doi.org/10.1177/1420326X211059449.

[118] Fanger, P. O. *Thermal Comfort: Analysis and Applications in Environmental Engineering*. (Copenhagen: Danish Technical Press, 1970).

[119] Kuga, K., Wargocki, P. & Ito, K. Breathing zone and exhaled air re-inhalation rate under transient conditions assessed with a computer-simulated person. *Indoor Air* **32**, 1–21 (2022) At https://doi.org/10.1111/ina.13003.

[120] Wu, C. & Ahmed, N. A. A novel mode of air supply for aircraft cabin ventilation. *Build. Environ.* **56**, 47–56 (2012) At https://doi.org/10.1016/j.buildenv.2012.02.025.

[121] Wu, C. & Ahmed, N. A. Numerical Study of Transient Aircraft Cabin Flowfield with Unsteady Air Supply. *J. Aircr.* **48**, 1994–2001 (2011) At https://doi.org/10.2514/1.C031415.

[122] Zhang, Z., Zhang, W., Zhai, Z. J. & Chen, Q. Y. Evaluation of various turbulence models in predicting airflow and turbulence in enclosed environments by CFD: Part 2—comparison with experimental data from literature. *HVAC R Res.* **13**, 871–886 (2007) At https://doi.org/10.1080/10789669.2007.10391460.

[123] Zhang, T. T., Li, P., Zhao, Y. & Wang, S. Various air distribution modes on commercial airplanes - Part 2: Computational fluid dynamics modeling and validation. *HVAC R Res.* **19**, 457–470 (2013) At https://doi.org/10.1080/10789669.2013.789368.

[124] Trupka, Andrew T. Tracer Gas Mapping of a Beverage Cart Wake in a Twin Aisle Aircraft Cabin (MSc. Thesis). (Kansas State University, 2011). At http://hdl.handle.net/2097/8853

[125] Madden, Michael L. The Effects of Passenger Loading and Ventilation Air on Airflow Patterns within an Aircraft Cabin (MSc. Thesis). (Kansas State University, 2015). At http://hdl.handle.net/2097/19107

[126] Shehadi, M. F., Hosni, M. H. & Jones, B. W. Airflow Distribution in the Longitudinal Plan of a Boeing 767 Mockup Cabin. In *ASME International Mechanical Engineering Congress and Exposition, Proceedings (IMECE)* vol. 7 (2014). At https://www.researchgate.net/publication/273968615

[127] Shehadi, Maher F. Airflow Distribution and Turbulence Analysis in the Longitudinal Direction of a Boeing 767 Mockup Cabin (PhD Thesis). (Kansas State University, 2015). At http://hdl.handle.net/2097/19023

[128] Shehadi, M. F. Heat Convective Effects on Turbulence and Airflow inside an B767 Aircraft Cabin. *Fluids* **4**, 167 (2019) At https://doi.org/10.3390/fluids4030167.

[129] Keshavarz, A., Jones, B. W., Hosni, M. H. & Beneke, J. M. Experimental measurements for gaseous transport within an aircraft cabin. *Build. Environ.* **89**, 327–335 (2015) At https://doi.org/10.1016/j.buildenv.2015.03.011.

[130] Darrah, I., Bennett, J. S., Jones, B. W. & Hosni, M. H. Infectious passenger isolation system for aircraft. *ASHRAE Trans.* **125**, 288–296 (2019) At https://www.ashrae.org/file%20library/technical%20resources/covid-19/kc021.pdf.

[131] Mahmoud, S., Neu, D., Menchaka, K., *et al.* Transport and Containment of Infectious Disease Expelled by Coughing in an Aircraft Cabin. *ASHRAE Trans.* **126**, 375–383 (2020) At https://www.researchgate.net/publication/340741967.

[132] Office of the Federal Register & National Archives and Records Administration. 14 CFR 25 - AIRWORTHINESS STANDARDS: TRANSPORT CATEGORY AIRPLANES. In *Code of Federal Regulations* 195–470 (Federal Aviation Administration, 2021).

[133] Chen, R., Fang, L., Liu, J., *et al.* Cabin air quality on non-smoking commercial flights: A review of published data on airborne pollutants. *Indoor Air* **31**, 926–957 (2021) At https://doi.org/10.1111/ina.12831.

[134] Chen, R., Fang, L., Liu, J., *et al.* Author Correction: Cabin air quality on non-smoking commercial flights: A review of published data on airborne pollutants. *Indoor Air* **32**, 1–5 (2022) At https://doi.org/10.1111/ina.12977.

[135] Sumner, A. L. & James, R. R. *Relate air quality and other factors to comfort and health related symptoms reported by passengers and crew on commercial transport aircraft (Part 2)*. 1262-RP Part 2 (2018).

[136] Silcott, D. B., Kinahan, S. M., Santarpia, J. L., *et al. TRANSCOM/AMC Commercial Aircraft Cabin Aerosol Dispersion Tests*. (2020). At https://www.ustranscom.mil/cmd/docs/TRANSCOM Report Final.pdf

[137] Kinahan, S. M., Silcott, D. B., Silcott, B. E., *et al.* Aerosol tracer testing in Boeing 767 and 777 aircraft to simulate exposure potential of infectious aerosol such as SARS-CoV-2. *PLoS One* 1–19 (2021) At https://doi.org/10.1371/journal.pone.0246916

[138] Mazumdar, S. & Chen, Q. Y. Influence of cabin conditions on placement and response of contaminant detection sensors in a commercial aircraft. *J. Environ. Monit.* **10**, 71–81 (2008) At https://doi.org/10.1039/b713187a.

[139] Mazumdar, S., Poussou, S. B., Lin, C.-H., *et al.* Impact of scaling and body movement on contaminant transport in airliner cabins. *Atmos. Environ.* **45**, 6019–6028 (2011) At https://doi.org/10.1016/j.atmosenv.2011.07.049.

[140] Buck, T. & Isambert, E. *Workshop on future Cabin Air Quality Research - Workshop results & Stakeholder recommendation*. *Workshop on future Cabin Air Quality Research*. EASA (2020). At https://www.easa.europa.eu/en/downloads/110619/en

[141] ASTM. *Standard Guide for Selecting Instruments and Methods for Measuring Air Quality in Aircraft Cabins (D6399-18)*. (2018) https://doi.org/10.1520/D6399-18

[142] Overfelt, R. A., Jones, B. W., Loo, S. M., *et al. Sensors and Prognostics to Mitigate Bleed Air Contamination Events 2012 Progress Report*. *Airliner Cabin Environmental Research (ACER)* (2012). At https://www.faa.gov/data_research/research/med_humanfacs/cer/media/SensorsPrognostics.pdf

[143] Bergin, S., Baalbergen, E., Greene, G., *et al. On-board air quality : Literature review and methodological survey*. *Future Sky Safety* (2016). At https://www.futuresky-safety.eu/wp-content/uploads/2016/11/FSS_P7_Cranfield_D7.6_v2.0.pdf

[144] Kos, J., Greene, G., Jentink, H. W., *et al. On-board air quality – Final report on the effect of new materials*. *Future Sky Safety* (2018). At https://www.futuresky-safety.eu/wp-content/uploads/2015/05/FSS_P7_NLR_D7.14_v2.0.pdf

[145] Houtzager, M., Heslinga, D., Spek, F., *et al. FACTS D7 Final Report*. (2020). At https://facts.aero/images/Status/FACTS-D7-Final_Report.pdf

[146] Bhardwaj, J., Hong, S., Jang, J., *et al.* Recent advancements in the measurement of pathogenic airborne viruses. *J. Hazard. Mater.* **420**, (2021) At https://doi.org/10.1016/j.jhazmat.2021.126574.

[147] Mainelis, G. Bioaerosol sampling: Classical approaches, advances, and perspectives. *Aerosol Sci. Technol.* **54**, 496–519 (2020) At https://doi.org/10.1080/02786826.2019.1671950.

[148] Breshears, L. E., Nguyen, B. T., Robles, S. M., Wu, L. & Yoon, J. Biosensor detection of airborne respiratory viruses such as SARS-CoV-2. *SLAS Technol.* **27**, 4–17 (2022) At https://doi.org/10.1016/j.slast.2021.12.004.

[149] Xiong, H., Ye, X., Li, Y., *et al.* Efficient Microfluidic-Based Air Sampling/Monitoring Platform for Detection of Aerosol SARS-CoV-2 On-site. *Anal. Chem.* **93**, 4270–4276 (2021) At https://doi.org/10.1021/acs.analchem.0c05154.

[150] Chen, H. & Yao, M. A high-flow portable biological aerosol trap (HighBioTrap) for rapid microbial detection. *J. Aerosol Sci.* **117**, 212–223 (2018) At https://doi.org/10.1016/j.jaerosci.2017.11.012.

[151] Hong, S., Bhardwaj, J., Han, C.-H. & Jang, J. Gentle Sampling of Submicrometer Airborne Virus Particles using a Personal Electrostatic Particle Concentrator. *Environ. Sci. Technol.* **50**, 12365–12372 (2016) At https://doi.org/10.1021/acs.est.6b03464.

[152] Usachev, E. V., Agranovski, E., Usacheva, O. V. & Agranovski, I. E. Multiplexed Surface Plasmon Resonance based real time viral aerosol detection. *J. Aerosol Sci.* **90**, 136–143 (2015) At https://doi.org/10.1016/j.jaerosci.2015.08.009.

[153] Hwang, G. M., DiCarlo, A. A. & Lin, G. C. An analysis on the detection of biological contaminants aboard aircraft. *PLoS One* **6**, (2011) At https://doi.org/10.1371/journal.pone.0014520.

[154] Shehadi, M. F., Hosni, M. H. & Jones, B. W. Experimental investigation of optimal particulate sensor location in an aircraft cabin. In *ASME Fluids Engineering Division (Publication) FEDSM* vol. 1 1–10 (2010). At https://www.researchgate.net/publication/267645077

[155] Korves, T. M., Johnson, D., Jones, B. W., *et al.* Detection of respiratory viruses on air filters from aircraft. *Lett. Appl. Microbiol.* **53**, 306–312 (2011) At https://doi.org/10.1111/j.1472-765X.2011.03107.x.

[156] Korves, T. M., Piceno, Y. M., Tom, L. M., *et al.* Bacterial communities in commercial aircraft high-efficiency particulate air (HEPA) filters assessed by PhyloChip analysis. *Indoor Air* **23**, 50–61 (2013) At https://doi.org/10.1111/j.1600-0668.2012.00787.x.

[157] Boeing. *767 Airplane Characteristics for Airport Planning*. *D6-58328* (2012). At https://www.boeing.com/resources/boeingdotcom/commercial/airports/acaps/767.pdf

[158] Simmons, G. & Worden, L. Advancements in Overhead Stowage Bin Article Retention. *Aero Magazine* (2001). At https://www.boeing.com/commercial/aeromagazine/aero_15/overhead.pdf

[159] Saranga, D. Boeing 767-300ER. https://www.the-blueprints.com/blueprints/modernplanes/boeing/76409/view/boeing_767-300er/.

[160] Roskam, J. *Airplane Design Part III: Layout Design of Cockpit, Fuselage, Wing and Empennage: Cutaways and Inboard Profiles*. (DARcorporation, 2002).

[161] Moukalled, F., Mangani, L. & Darwish, M. *The Finite Volume Method in Computational Fluid Dynamics*. vol. 113 (Springer International Publishing, 2016).

[162] ANSYS, I. *ANSYS Fluent Theory Guide*. (2021).

[163] Chen, Q. Y. & Wang, M. *Modeling Low Velocity Large Scale Fluctuating Flows in Ventilated Spaces at Transitional Reynolds Numbers*. *ASHRAE Report* (2009).

[164] CFD Online. Two equation turbulence models. https://www.cfd-online.com/Wiki/Two_equation_models.

[165] Shih, T.-H., Liou, W. W., Shabbir, A., Yang, Z. & Zhu, J. A New k-ϵ Eddy Viscosity Model for High Reynolds Number Turbulent Flows. *Comput. Fluids* **24**, 227–238 (1995) At https://doi.org/10.1016/0045-7930(94)00032-T.

[166] FreeMapTools. Elevation Finder. https://www.freemaptools.com/elevation-finder.htm.

[167] National Geodetic Survey. Surface Gravity Prediction. https://geodesy.noaa.gov/cgi-bin/grav_pdx.prl.

[168] Buck Research Instruments. Appendix 1: Humidity Conversion Equations. In *MODEL CR-1A HYGROMETER WITH AUTOFILL OPERATING MANUAL* (2012). At https://www.hygrometers.com/wp-content/uploads/CR-1A-users-manual-2009-12.pdf

[169] ICAO. *Manual of the ICAO Standard Atmosphere*. Doc 7488/3 (1993).

[170] Moran, M. J., Shapiro, H. N., Boettner, D. D. & Bailey, M. B. *Fundamentals of Engineering Thermodynamics*. (Wiley, 2018).

[171] Wilke, C. R. A viscosity equation for gas mixtures. *J. Chem. Phys.* **18**, 517–519 (1950) At https://doi.org/10.1063/1.1747673.

[172] CFD Online. Turbulence Intensity. https://www.cfd-online.com/Wiki/Turbulence_intensity.

[173] de Tilly, A. & Sousa, J. M. M. An experimental study of heat transfer in a two-dimensional T-junction operating at a low momentum flux ratio. *Int. J. Heat Mass Transf.* **51**, 941–947 (2008) At https://doi.org/10.1016/j.ijheatmasstransfer.2007.10.012.

[174] Melo, M. J., Sousa, J. M. M., Costa, M. & Levy, Y. Flow and Combustion Characteristics of a Low-NOx Combustor Model for Gas Turbines. *J. Propuls. Power* **27**, 1212–1217 (2011) At https://doi.org/10.2514/1.56286.

[175] Bureau International des Poids et Mesures. *The International System of Units (SI)*. (BIPM, 2019). At https://www.bipm.org/documents/20126/41483022/SI-Brochure-9-EN.pdf

[176] Hilsenrath, J., Beckett, C. W., Benedict, W. S., *et al. Tables of Thermal Properties of Gases*. vol. 564 (National Bureau of Standards, 1955). At https://nvlpubs.nist.gov/nistpubs/Legacy/circ/nbscircular564.pdf

[177] NIST. NIST Guide to the SI , Footnotes. (2022). https://www.nist.gov/pml/special-publication-811/nist-guide-si-footnotes#f22

8 Appendix

8.1 Geometry Details

All dimensions are in inches unless specified otherwise.

8.1.1 Seats Mounting

Figure 8-1 and Figure 8-2 show the position of the seat mounting locations. Table 19 has the dimensions of the mentioned figures organized by row. The seats layout information was taken directly from [54]. It is noted here that some seats collide with the cabin wall: 11A, 10G; 7G and 4G.

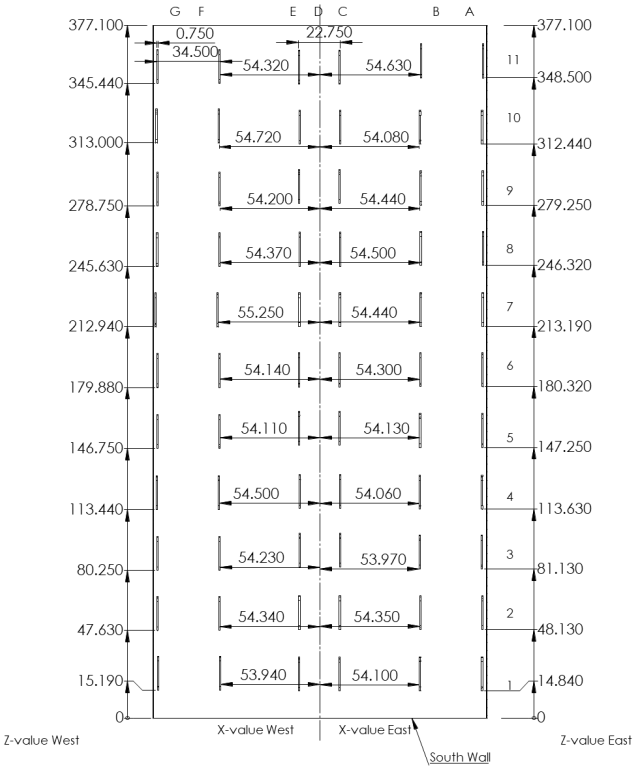

Figure 8-2. West and east seats mounting points.

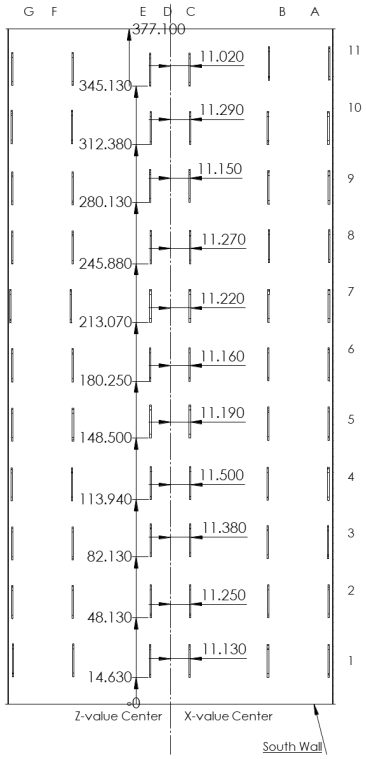

Figure 8-1. Center seats mounting points.

Row	Z-Value East	X-value East	Z-value Center	X-value Center	Z-value West	X-value West
1	14.840	54.100	14.630	11.130	15.190	53.940
2	48.130	54.350	48.130	11.250	47.630	54.340
3	81.130	53.970	82.130	11.380	80.250	54.230
4	113.630	54.060	113.940	11.500	113.440	54.500
5	147.250	54.130	148.500	11.190	146.750	54.110
6	180.320	54.300	180.250	11.160	179.880	54.140
7	213.190	54.440	213.070	11.220	212.940	55.250
8	246.320	54.500	245.880	11.270	245.630	54.370
9	279.250	54.440	280.130	11.150	278.750	54.200
10	312.440	54.080	312.380	11.290	313.000	54.720
11	348.500	54.630	345.130	11.020	345.440	54.320

Table 19. Seats mounting points coordinates. Dimensions in inches.

8.1.2 Layout of buttons, connectors, end caps and supply hoses.

In Figure 8-3, the start of the axis in the Typical Diffuser section is at the start of the diffuser section, i.e., right after the end cap. Table 21 and Table 20 have the z coordinates, i.e., the distance to the south wall of the centerline of the circular supply hoses and the front of the connectors respectively. Figure 8-4 shows the end caps and diffuser sections dimensions in inches. Figure 8-5 (east) and Figure 8-6 (west) show the locations of the supply hoses and connectors as shown in Table 21 and Table 20 as well as the spacer buttons locations. In these figures, the start of the origin of the measurement axis z' of the spacer buttons is z=0.1875 inches. This is to directly compare with the reference document. Therefore Table 22 has the extracted coordinates of the button's centerline from the figure in this different axis z=z'+0.1875 inches, for example, button east 2 center is at z= 6.938 in. Additionally, due to the end cap locations, spacer buttons east 1 and both west and east buttons number 27, 54 and 77 were removed for not being consistent with other dimensions. The spacer buttons and connectors locations were taken from a ppt provided by KSU[13].

Supply Hoses

	East	West
1	16.1000	16.1000
2	36.6000	36.6000
3	59.0000	59.0000
4	80.4000	80.4000
5	103.1000	103.1000
6	121.6000	121.6000
7	147.8375	148.0000
8	168.3375	168.5000
9	190.7375	190.9000
10	212.1375	212.3000
11	234.8375	235.0000
12	253.3375	253.5000
13	279.6375	279.9000
14	300.1375	300.4000
15	322.5375	322.8000
16	343.9375	344.2000
17	366.6375	366.9000

Table 21. Supply Hoses z-coordinates in inches.

Connectors

	East	West
1	22.000	22.750
2	44.000	44.750
3	66.000	66.750
4	88.000	88.750
5	110.000	110.750
6	154.750	155.380
7	176.750	177.380
8	198.750	199.380
9	220.750	221.380
10	242.750	243.380
11	287.380	288.000
12	309.380	310.000
13	331.380	332.000
14	353.380	354.000

Table 20. Connectors z-coordinates in inches.

[13] Jones, Byron. "Re: Covid 19 Boeing 767 Data Research". Received by Carlos Raposo, 14 Jan. 2021.

Spacer Buttons z'=z-0.1875

#	East	West	#	East	West	#	East	West
1	□1.75	2.130	**26**	126.750	127.130	**51**	249.380	249.750
2	6.750	7.130	**27**	□131.75	□132.13	**52**	254.380	254.750
3	11.750	12.130	**28**	134.380	134.750	**53**	259.380	259.750
4	16.750	17.130	**29**	139.380	139.750	**54**	□264.38	□264.75
5	21.750	22.130	**30**	144.380	144.750	**55**	267.000	267.380
6	26.750	27.130	**31**	149.380	149.750	**56**	272.000	272.380
7	31.750	32.130	**32**	154.380	154.750	**57**	277.000	277.380
8	36.750	37.130	**33**	159.380	159.750	**58**	282.000	282.380
9	41.750	42.130	**34**	164.380	164.750	**59**	287.000	287.380
10	46.750	47.130	**35**	169.380	169.750	**60**	292.000	292.380
11	51.750	52.130	**36**	174.380	174.750	**61**	297.000	297.380
12	56.750	57.130	**37**	179.380	179.750	**62**	302.000	302.380
13	61.750	62.130	**38**	184.380	184.750	**63**	307.000	307.380
14	66.750	67.130	**39**	189.380	189.750	**64**	312.000	312.380
15	71.750	72.130	**40**	194.380	194.750	**65**	317.000	317.380
16	76.750	77.130	**41**	199.380	199.750	**66**	322.000	322.380
17	81.750	82.130	**42**	204.380	204.750	**67**	327.000	327.380
18	86.750	87.130	**43**	209.380	209.750	**68**	332.000	332.380
19	91.750	92.130	**44**	214.380	214.750	**69**	337.000	337.380
20	96.750	97.130	**45**	219.380	219.750	**70**	342.000	342.380
21	101.750	102.130	**46**	224.380	224.750	**71**	347.000	347.380
22	106.750	107.130	**47**	229.380	229.750	**72**	352.000	352.380
23	111.750	112.130	**48**	234.380	234.750	**73**	357.000	357.380
24	116.750	117.130	**49**	239.380	239.750	**74**	362.000	362.380
25	121.750	122.130	**50**	244.380	244.750	**75**	367.000	367.380
	□ – removed					**76**	372.000	372.380
						77	□377.38	□377.38

Table 22. Spacer buttons z' coordinates in inches.

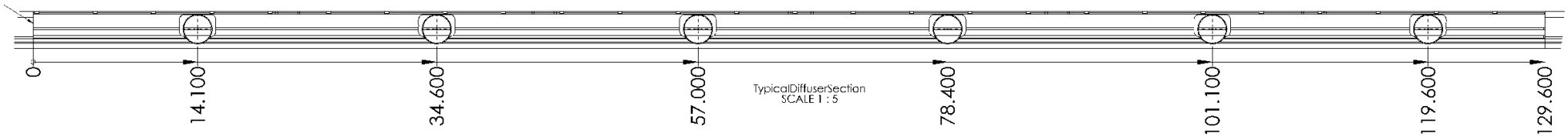

Figure 8-3. 2D Drawing of Typical Diffuser Section. Supply hose locations. Dimensions in inches.

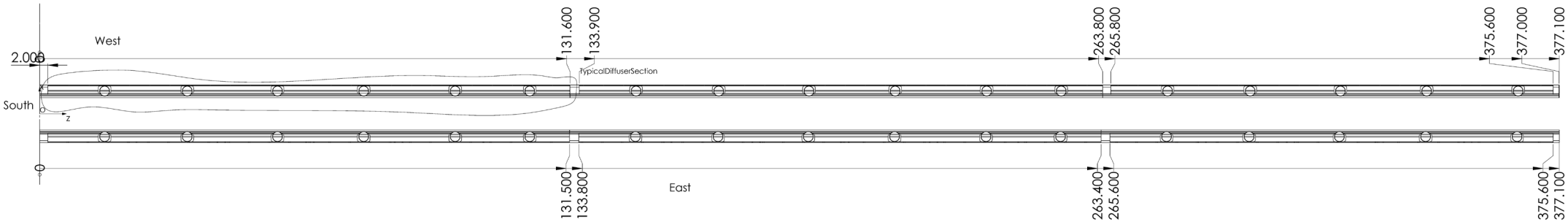

Figure 8-4. 2D Drawing of west and east diffuser sections. End cap locations. Dimensions in inches.

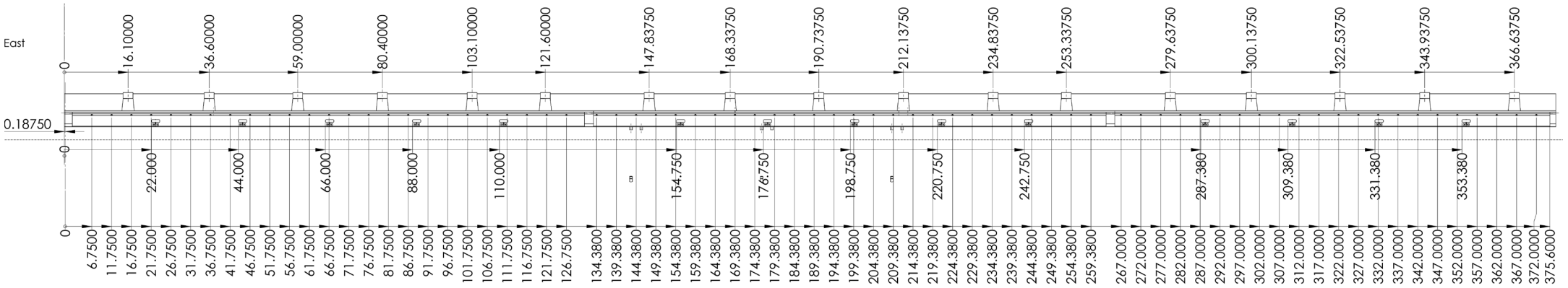

Figure 8-5. 2D Drawing of East section. Spacer buttons, connectors, and supply hose locations. Dimensions in inches.

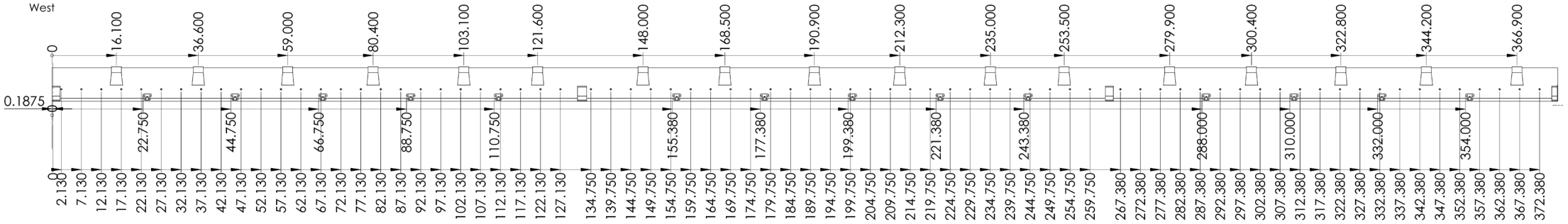

Figure 8-6. 2D Drawing of West section. Spacer buttons, connectors, and supply hose locations. Dimensions in inches.

8.2 Source Term UDF

```
#include "udf.h"

#define Ck3 0.23

DEFINE_SOURCE(udfsourcek,c,t,dS,eqn)

{

real x[ND_ND];

real con, source;

real rho =C_R(c,t);

real diss =C_D(c,t);

C_CENTROID(x,c,t);

con = Ck3*rho;

source = con*diss;

return source;

}
```

8.3 Air Properties Calculation

The cabin environment is subjected to multiple altitudes, which will affect the air properties. Based on the figure with cabin pressure schedule of Boeing 767 available in [12] the graph was fitted to a polynomial function with good accuracy ($R^2 = 0.9998$) where h_c is the cabin pressure altitude and h_A is the airplane pressure altitude, both in thousands of feet. Using this data, the maximum cabin altitude 8000 ft is reached at the airplane altitude of 42340 ft.

$$h_c = 6.456702 \times 10^{-5} h_A^3 - 3.392976 \times 10^{-4} h_A^2 + 9.053746 \times 10^{-2} h_A^1 - 0.1258169 \ (\text{ft} \times 10^3) \quad (34)$$

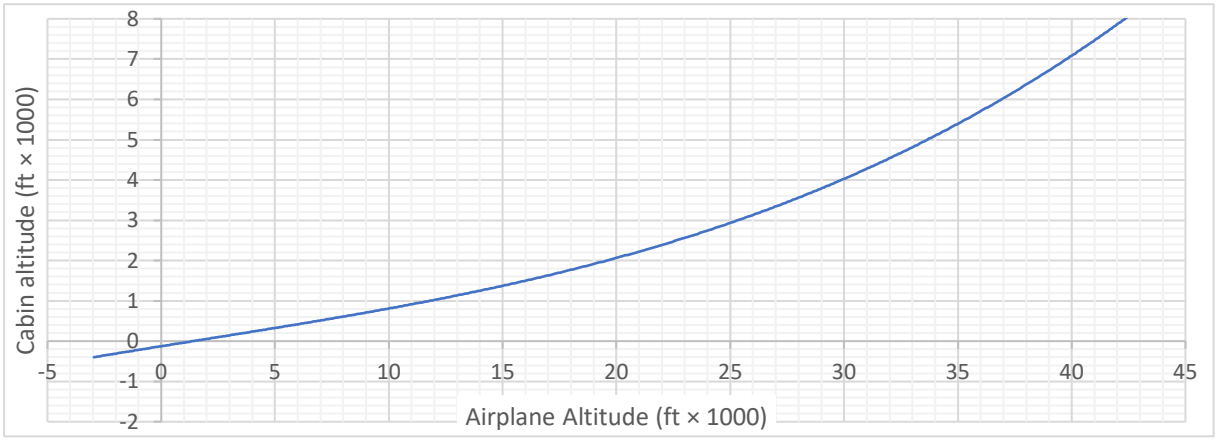

Figure 8-7. Boeing 767 Cabin Pressure Schedule in thousands of feet

Let us assume, at cruise level, the maximum cabin pressure height (geopotential height) is 8000 ft. at the airplane altitude of 42000 ft. Therefore, we need to know the air properties at sea level and at geopotential height of 8000 ft. The manual of ICAO [169] was used, below the used expressions and constants are represented.

The SI system was recently changed in 2019 [175]. The Avogadro number and Boltzmann constants are now exact and the universal gas constant is derived by the product of them.

Avogadro number	$N_A = 6.02214076 \times 10^{23}\ \mathrm{mol}^{-1}$	
Boltzmann Constant	$k_B = 1.380649 \times 10^{-23}\ \mathrm{J/K}$	
Universal Gas Constant	$R_u = N_A \cdot k_B = 8.31446261815324\ \mathrm{J\,K^{-1}mol^{-1}}$	(35)

Using the standard sea level values (T_0= 288.15 K, ρ_0=1.225 kg/m^3, p_0=101325 Pa) and the ideal gas law, we can compute the specific constant of dry air at those conditions its mean molar mass. To compare with the old value (using previous universal gas constant R_u=8.314320 J mol^{-1} K^{-1}) of dry air molar mass ($M_{0,\,old}$=28.964420 g/mol) the relative error is just 0.002%. The values used to compute the dry air constant remain unchanged, therefore most of the values will remain unchanged. However, expressions that use either the universal gas constant, Boltzmann constant and Avogadro number will slightly change eq. (58) and (60).

Ideal Gas Law	$p = \rho R T$	(36)
Dry air gas constant	$R_{air} = \frac{p_0}{\rho_0 T_0} = \frac{1013255}{1.225 \times 288.15} = 287.052874\ \mathrm{J\,kg^{-1}K^{-1}}$	(37)
Mean Molar Mass of dry air	$M_0 = \frac{R_u}{R_{air}} = 28.964916794\ \mathrm{g/mol}$	(38)
Relative error of molar mass	$\frac{M_0^{old} - M_0^{2019}}{M_0^{2019}} = 0.002\%$	(39)

Finally, when thermal calculations we need the value of specific heat capacity for dry air, which changes with temperature and pressure. Using the table 2.3 from NBS 564 [176] we can interpolate the values of C_p/R for a pressure altitude of 8000ft ($p_{8000\mathrm{ft}}$ = 75262.361 Pa) between 0.7 atm and 1 atm as shown in Table 23. In the cabin environment we can just fix the temperature range from 190 K to 350 K. Figure 8-8 shows the 2D plot result.

Temperature K	Pressure = 0.7 atm	*0.7428*	1
190	1005.5	1005.7	1006.9
200	1005.3	1005.4	1006.5
210	1005.0	1005.2	1006.1
220	1004.8	1005.0	1005.8
230	1004.7	1004.9	1005.6
240	1004.7	1004.8	1005.5
250	1004.8	1004.9	1005.5
260	1004.8	1004.9	1005.5
270	1005.0	1005.1	1005.6
280	1005.2	1005.3	1005.8
290	1005.5	1005.6	1006.0
300	1005.9	1006.0	1006.4
310	1006.4	1006.4	1006.8
320	1006.9	1006.9	1007.3
330	1007.5	1007.6	1007.9
340	1008.2	1008.2	1008.5
350	1008.9	1009.0	1009.3

Table 23. C_p of dry air from 190-350 K , at pressures of 0.7, 0.7428 and 1 atm.

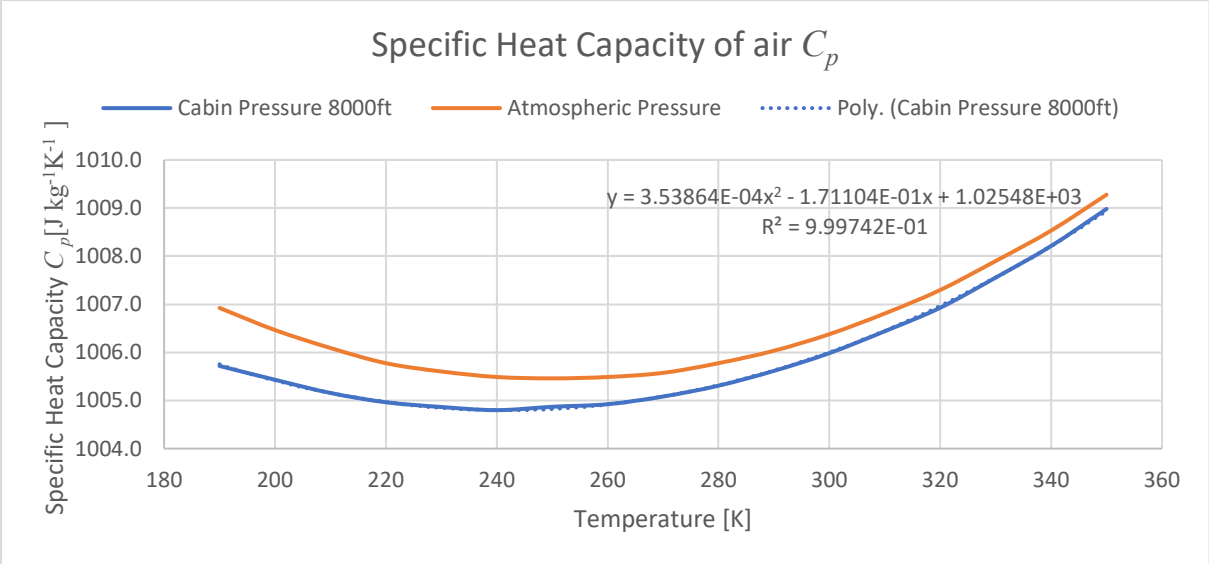

Figure 8-8. 2D Plot of C_p of dry air vs Temperature at 1 atm and cabin pressure of 8000 ft.

Then, we can fit a linear relationship between the range of 280 K and 320 K, for a constant pressure of 75262.361 Pa. For reference polynomial expressions were fitted for C_p at atmospheric pressure valid between 190 and 350 K shown in Table 24 . For 23.5°C or 296.65 K, at 1 atm C_p of air is 1006.26 J kg^{-1}K^{-1} and at 75262.361 Pa C_p of air is 1005.92 J kg^{-1}K^{-1}. For 288.15 K and 1 atm, C_p of air is 1005.98 J kg^{-1}K^{-1}.

Valid Range (K)	Pressure (atm)	Air Specific Heat in function of Temperature ($\mathbf{J\,kg^{-1}K^{-1}}$)	
280-320, R^2=0.9913	0.743	$C_p = 4.0639207 \times 10^{-2}T + 9.9386365 \times 10^{2}$	(40)
190-350, R^2=0.9998	1	$C_p = 3.9199455 \times 10^{-4}T^2 - 1.9680378 \times 10^{-1}T + 1.030142 \times 10^{3}$	(41)

190-350, R^2=0.9997	0.743	$C_p = 3.5386412 \times 10^{-4}T^2 - 1.7110400 \times 10^{-1}T + 1.0254836 \times 10^{3}$	(42)
190-350, R^2=0.9990	0.1681	$C_p = 2.8129737 \times 10^{-4}T^2 - 1.2024711 \times 10^{-1}T + 1.0159171 \times 10^{3}$	(43)

Table 24. Air Specific Heat in function of Temperature polynomial equations.

For reference, Table 25 was made with the coefficients valid in the range of 190 K to 350 K for the calculation of specific air capacity in a polynomial form, eq. (44):

$$\frac{C_p}{R_{air}} = c_5T^5 + c_4T^4 + c_3T^3 + c_2T^2 + c_1T^1 + b \tag{44}$$

Pressure [Pa]	c_5	c_4	c_3	c_2	c_1	b	R^2
1013.25	0	0	0	8.9474×10^{-7}	-3.6198×10^{-4}	3.5289	0.99877
10132.5	0	0	0	9.4969×10^{-7}	-3.9764×10^{-4}	3.5351	0.99894
17035.05	0	0	0	9.7995×10^{-7}	-4.1890×10^{-4}	3.5391	0.99902
40530.0	0	0	0	1.0829×10^{-6}	-4.9129×10^{-4}	3.5527	0.99924
70927.50	0	0	0	1.2107×10^{-6}	-5.8118×10^{-4}	3.5698	0.99967
75262.36	0	0	0	1.2327×10^{-6}	-5.9607×10^{-4}	3.5725	0.99974
101325	0	0	0	1.3656×10^{-6}	-6.8560×10^{-4}	3.5887	0.99982
405300	0	0	0	2.8480×10^{-6}	-1.7053×10^{-3}	3.7764	0.99264
709275	0	0	0	4.5187×10^{-6}	-2.8400×10^{-3}	3.9818	0.99259
1013250	0	0	-3.2052×10^{-8}	3.2320×10^{-5}	-1.0951×10^{-2}	4.7969	0.99947
4053000	0	2.6961×10^{-9}	-3.2330×10^{-6}	1.4616×10^{-3}	-2.9714×10^{-1}	2.6775×10^{1}	0.99975
7092750	-1.0620×10^{-10}	1.5408×10^{-7}	-8.9208×10^{-5}	2.5803×10^{-2}	−3.7393	2.2199×10^{2}	0.99986
10132500	-1.8797×10^{-10}	2.7331×10^{-7}	-1.5856×10^{-4}	4.5946×10^{-2}	−6.6651	3.9265×10^{2}	0.99986

Table 25. Coefficients of C_p/R of dry air for pressures from 1013.25 Pa to 10132500 Pa.

g_0	9.80665	m/s^2	a_0	340.294	m/s
M_0	$28.9649168 \times 10^{-3}$	kg/mol	H_{p_0}	8434.5	m
N_A	$6.02214076 \times 10^{23}$	mol^{-1}	l_0	6.6334×10^{-8}	m
p_0	101325	Pa	n_0	2.5469×10^{25}	m^{-3}
R_u	8.31446261815324	$J/(K \cdot mol)$	$\bar{v}_{p0}$	458.94	m/s
R	287.052874247	$J/(K \cdot kg)$	γ_0	12.013	N/m^3
S	110.4	K	ν_0	1.4607×10^{-5}	m^2/s
T_i	273.15	K	λ_0	2.53259×10^{-2}	$W/(m \cdot K)$
T_0	288.15	K	μ_0	1.7894×10^{-5}	$Pa \cdot s$
t_i	0	°C	Z_0	6.9187×10^{9}	s^{-1}
t_0	15	°C	C_p	1005.98	$J/(kg \cdot K)$
β_s	1.4580×10^{-6}	$kg/(m \cdot s \cdot K^{1/2})$	r	6356766	m
κ	1.4	adim			
ρ_0	1.225	kg/m^3			
σ	3.650×10^{-10}	m			

Table 26. Used constants in ICAO manual with updated values.

The atmosphere is divided in layers based on the temperature gradient. The expressions are based on the lower limits of the concerned layer of pressure p_b, temperature T and vertical temperature gradient β. Using the expressions (47)-(49) Table 27 was generated and double checked with reference document. Table 26 shows the final result of the original table from ICAO manual with updated values.

Geopotential altitude	Temperature	Temperature Gradient	Pressure at boundary
$\mathbf{H_b}$ (m)	T_b (K)	β (K/m)	p_b(Pa)
−5000	320.65	-6.50×10^{-3}	1.77687×10^{5}
0	288.15	-6.50×10^{-3}	1.01325×10^{5}
11000	216.65	0	2.26320×10^{4}
20000	216.65	1.00×10^{-3}	5.47488×10^{3}
32000	228.65	2.80×10^{-3}	8.68016×10^{2}
47000	270.65	0	1.10906×10^{2}
51000	270.65	-2.80×10^{-3}	6.69385×10^{1}
71000	214.65	-2.00×10^{-3}	3.95639×10^{0}
80000	196.65		8.86272×10^{-1}

Table 27. Lower limits values at different layers of atmosphere.

The relation between geometric altitude h and geopotential altitude H is computed using the nominal earth radius r in eq. (45). The gravity acceleration g at given altitude can then be computed using the standard acceleration g_0 in eq. (46).

$$h = \frac{rH}{r - H} \tag{45}$$

$$g = g_0 \left(\frac{r}{r + h}\right)^2 \tag{46}$$

Then the following properties can be computed using the eq. (47)-(62).

Temperature	$T = T_b + \beta(H - H_b)$	(47)
Pressure for $\beta = 0$	$p = p_b \exp\left[-\frac{g_0}{RT}(H - H_b)\right], for\ \beta = 0$	(48)
Pressure for $\beta \neq 0$	$p = p_b \left[1 + \frac{\beta}{T_b}(H - H_b)\right]^{-\frac{g_0}{\beta R}}, for\ \beta \neq 0$	(49)
Density	$\rho = \frac{p}{RT}$	(50)
Specific Weight	$\gamma = \rho g$	(51)
Pressure scale height	$H_p = \frac{RT}{g}$	(52)
Mean free path	$l = \frac{1}{\sqrt{2}\pi\sigma^2 n}$	(53)
Speed of sound	$a = \sqrt{\kappa RT}$	(54)
Dynamic Viscosity	$\mu = \frac{\beta_s T^{3/2}}{T + S}$	(55)

Kinematic Viscosity	$\nu = \frac{\mu}{\rho}$	(56)
Thermal conductivity	$\lambda = \frac{2.64638 \times 10^{-3} \cdot T^{3/2}}{T + (245.4 \times 10^{-(12/T)})}$	(57)
Number density (number of neutral air particles per volume)	$n = \frac{N_a p}{R_u T}$	(58)
Mean particle speed (arithmetic average of air-particle speeds)	$\bar{v}_p = \left(\frac{8}{\pi} RT\right)^{1/2}$	(59)
Collision frequency (mean particle speed divided by mean free path)	$Z = 4\sigma^2 N_a \left(\frac{\pi}{R_u M_0}\right)^{1/2} \frac{p}{\sqrt{T}}$	(60)
Thermal diffusivity	$\alpha = \frac{\lambda}{C_p \times \kappa}$	(61)
Prandtl number	$\mathrm{Pr} = \frac{\nu}{\alpha}$	(62)

Based on these expressions, the pressure p is computed from the temperature T taking into account the different layers. The pressure scale height H_p is computed from gravity acceleration g and temperature T. The speed of sound, mean particle speed, thermal conductivity, thermal diffusivity, and dynamic viscosity are computed from temperature. The temperature and pressure are used to compute collision frequency, number density, mean free path, density. Kinematic viscosity is computed from dynamic viscosity and density; Prandtl number from thermal diffusivity and kinematic viscosity; specific weight is computed from density and gravity acceleration.

The thermal conductivity expression from ICAO manual is the conversion from the expression table 1-C from NBS 564 [176] in the form of

$$\lambda = a_{\mathrm{th}} \sqrt{T} \Big/ \left(1 + \frac{b_{\mathrm{th}} \times 10^{-c_{\mathrm{th}}/T}}{T}\right) \tag{63}$$

with $a_{\mathrm{th}} = 0.6325 \times 10^{-5}\ \mathrm{cal\ cm^{-1} s^{-1} K^{1/2}}, b_{\mathrm{th}} = 245.4\ \mathrm{K}, c_{\mathrm{th}} = 12\ \mathrm{K}$ in units of $\mathrm{cal\ cm^{-1} s^{-1} K^{-1}}$. In the NBS 564 it is stated that cal represents the thermochemical calorie ($\mathrm{cal_{th}}$), which is exactly equal to $4.184\ \mathrm{J}$ [177], instead of the international table calorie ($\mathrm{cal_{IT}}$) equal to $4.1868\ \mathrm{J}$. Thus, the coefficient is $a_{\mathrm{th}} = 2.64638 \times 10^{-3}\ \mathrm{W\ m^{-1} K^{1/2}}$ instead of 2.648151×10^{-3}as used in ICAO manual this is a small relative error of 0.067%. This expression is an empirical formula valid for $1\ \mathrm{atm}$.

$$a_{\mathrm{th}} = 0.6325 \times 10^{-5} \frac{\mathrm{cal}}{\mathrm{cm\ s}} \mathrm{K^{1/2}} \times 4.184 \frac{\mathrm{J}}{\mathrm{cal_{th}}} \times \frac{1}{10^{-2}} \frac{\mathrm{cm}}{\mathrm{m}} \frac{1}{\mathrm{s}} \mathrm{K^{1/2}} = 2.64638 \times 10^{-3} \mathrm{W\ m^{-1} K^{1/2}} \tag{64}$$

For reference the air properties at the geopotential heights of 0, 8000 and $42000\ \mathrm{ft}$ are in Table 28 computed using the expressions above, and with the C_p computed for each pressure and temperature using eq. (40) - (43). Notice these are the properties of the outside air going to the engine.

H (ft)	0.00 ft (ground)	8000 (cabin)	42000 (cruise)
H (m)	0	2438.4	12801.6
T (K)	288.150	272.300	216.650
p (Pa)	101325	75262.36	17035.05
ρ (kg/m^3)	1.225000	0.962870	0.273920
g (m/s^2)	9.806650	9.799128	9.767191
a (m/s)	340.2940	330.8027	295.0695
μ (Pa · s)	1.78938×10^{-5}	1.71187×10^{-5}	1.42161×10^{-5}
ν (m^2/s)	1.46072×10^{-5}	1.77788×10^{-5}	5.18988×10^{-5}
λ (W/(m · K))	2.53259×10^{-2}	2.40702×10^{-2}	1.95046×10^{-2}
H_p(m)	8434.51	7976.69	6367.24
γ (N/m^3)	12.01315	9.435286	2.675429
n (m^{-3})	2.5469165×10^{25}	2.0019180×10^{25}	5.6951125×10^{24}
$\bar{v}_p$ (m/s)	458.945	446.144	397.952
Z (s^{-1})	6.918718×10^{9}	5.286546×10^{9}	1.341477×10^{9}
l (m)	6.633377×10^{-8}	8.4392359×10^{-8}	2.9665187×10^{-7}
C_p (J/kg · K)	1005.98	1005.13	1003.07
α (m^2/s)	2.055128×10^{-5}	2.487079×10^{-5}	7.098771×10^{-5}
Pr	0.7107675	0.7148483	0.7310963

Table 28. Dry air properties at 0, 8000 and 42000 ft.

The properties of cabin air should be computed using the mean temperature of the cabin air and the pressure of the cabin (maximum pressure altitude is 8000 ft). As mentioned before, the Boeing 767 reaches an altitude of 42000 ft (assumed to be geopotential altitude) a gravity acceleration of 9.767191 m/s^2.

Furthermore, as previous stated, the average of temperature measured in airplane is reported to be 23.5 °C (Table 8). This value is in line with values reported in Table 11. Let us also consider a maximum of 31°C and a minimum of 17°C. Then the properties were computed at airplane altitude and cabin altitude of 42000 ft and 8000 ft in Table 29 and at ground in Table 30.

Values computed at airplane altitude of 42000ft and cabin altitude 8000ft				Expression
H (ft)	8000.00			Cabin Pressure altitude
g (m/s^2)	9.7671914			From Airplane altitude
p (Pa)	75262.36064			From Cabin altitude
T_{air} (°C)	17	23.5	31	Input
ρ (kg/m^3)	0.903635661	0.883835789	0.862041384	(50)
a (m/s)	341.4729097	345.2765981	349.6140506	(54)
μ (Pa · s)	1.79901×10^{-5}	1.83011×10^{-5}	1.86557×10^{-5}	(55)
ν (m^2/s)	1.99086×10^{-5}	2.07064×10^{-5}	2.16413×10^{-5}	(56)

$\boldsymbol{\lambda}$ (W/(m · K))	2.54829×10^{-2}	2.59913×10^{-2}	2.65738×10^{-2}	(57)
$\boldsymbol{H_p}$(m)	8527.363463	8718.395214	8938.816465	(52)
$\boldsymbol{\gamma}$ (N/m^3)	8.825982494	8.632593362	8.419723231	(51)
$\boldsymbol{n}$ (m^{-3})	1.87876×10^{25}	1.8376×10^{25}	1.79228×10^{25}	(58)
$\boldsymbol{\bar{v}_p}$ (m/s)	460.534632	465.6645565	471.5143532	(59)
$\boldsymbol{Z}$ (s^{-1})	5.12135×10^{9}	5.06494×10^{9}	5.00210×10^{9}	(60)
$\boldsymbol{l}$ (m)	8.99244×10^{-8}	9.19389×10^{-8}	9.42633×10^{-8}	(53)
$\boldsymbol{C_p}$ (J/(kg · K))	1005.6286	1005.8661	1006.1773	(42)
$\boldsymbol{\alpha}$ (m^2/s)	2.80426×10^{-5}	2.92359×10^{-5}	3.06373×10^{-5}	(61)
Pr	0.7099415	0.70825359	0.70637173	(62)

Table 29. Cabin Air properties at a pressure altitude of 8000 ft with different temperatures and airplane altitude of 42000 ft.

Values computed at ground				Expression
H (ft)	0			Cabin Pressure altitude
$\boldsymbol{g}$ (m/s^2)	9.80665			From Airplane altitude
$\boldsymbol{p}$ ($\boldsymbol{Pa}$)	101325			From Cabin altitude
$\boldsymbol{T_{air}}$ (°C)	17	23.5	31	Input
$\boldsymbol{\rho}$ (kg/m^3)	1.2165561	1.1898997	1.1605581	(50)
$\boldsymbol{a}$ (m/s)	341.4729	345.2766	349.6141	(54)
$\boldsymbol{\mu}$ (Pa · s)	1.79901×10^{-5}	1.83011×10^{-5}	1.86557×10^{-5}	(55)
$\boldsymbol{\nu}$ (m^2/s)	1.47878×10^{-5}	1.53803×10^{-5}	1.60748×10^{-5}	(56)
$\boldsymbol{\lambda}$ (W/(m · K))	2.54829×10^{-2}	2.59913×10^{-2}	2.65738×10^{-2}	(57)
$\boldsymbol{H_p}$(m)	8493.052	8683.315	8902.850	(52)
$\boldsymbol{\gamma}$ (N/m^3)	11.93034	11.66893	11.38119	(51)
$\boldsymbol{n}$ (m^{-3})	2.5293606×10^{25}	2.4739389×10^{25}	2.4129344×10^{25}	(58)
$\boldsymbol{\bar{v}_p}$ (m/s)	460.535	465.665	471.514	(59)
$\boldsymbol{Z}$ (s^{-1})	6.8948314×10^{9}	6.8188755×10^{9}	6.7342778×10^{9}	(60)
$\boldsymbol{l}$ (m)	6.679418×10^{-8}	6.829052×10^{-8}	7.001706×10^{-8}	(53)
$\boldsymbol{C_p}$ (J/(kg · K))	1006.04027	1006.25619	1006.54649	(42)
$\boldsymbol{\alpha}$ (m^2/s)	2.082103×10^{-5}	2.170745×10^{-5}	2.274850×10^{-5}	(61)
Pr	0.7102321	0.7085283	0.7066309	(62)

Table 30. Cabin Air properties at a pressure altitude 0 ft with different temperatures and airplane altitude of 0 ft.

We are now in conditions to compute the minimum volumetric flow rate required per person.

According to CFR 25.831 and CFR 25.841 [132] the minimum mass flow of fresh air per person is 0.55 lb/min. The conversion factor for [177] 1 avoirdupois pound is equal to 0.45359237 kg. Therefore, this number will change with pressure, temperature, and the ratio of recirculated air (ratio). Using eq. (66)

Table 31 was filled with values of the total minimum volumetric flow rate with different recirculation ratios, pressure and temperatures.

$$Q_{Total} = \frac{\dot{m}_{fresh}}{\rho_{air}} \frac{1}{(1 - \text{ratio})} \tag{65}$$

$$Q_{Total}^{pax} = \frac{0.55}{\rho_{air}} \frac{1}{(1 - \text{ratio})} \times \frac{0.45359237}{60} \times 1000\,\text{L/s per pax} \tag{66}$$

	0 ft, p=101325 Pa				8000 ft, p=75262.36 Pa			
Ratio	***T*= 17°C**	**23.5°C**	**25°C**	**31°C**	**17°C**	**23.5°C**	**25°C**	**31°C**
0.75	13.671	13.977	14.048	14.331	18.405	18.818	18.913	19.293
0.50	6.836	6.989	7.024	7.165	9.203	9.409	9.456	9.647
0.25	4.557	4.659	4.683	4.777	6.135	6.273	6.304	6.431
0	3.418	3.494	3.512	3.583	4.601	4.704	4.728	4.823

Table 31. Minimum volumetric flow rate required by CFR 25.831 in L/s per person in different conditions.

8.4 Additional Calculations

The Reynolds number can be computed in the nozzle area and in the slot area. As stated in 8.3 the dynamic viscosity is computed using Sutherland's Formula (55) $\mu = \beta_s \frac{T^{1.5}}{T+\mathrm{S}}$ Which, for dry air, $\beta_s = 1.458 \times 10^{-5}, \mathrm{S} = 110.4\ \mathrm{K}$. Considering a supply temperature of 288.71 K, then $\mu_{air} = 1.792 \times 10^{-5} \mathrm{Pa \cdot s}$.

The density is computed using the ideal gas law $\rho = \frac{p}{RT}$. The specific gas constant is calculated by (38) $R = R_u/M$. Fluent universal gas constant is $8.314472\ \mathrm{J\ K^{-1}\ mol^{-1}}$ and using $M_{air} = 28.96495\ \mathrm{g/mol}$, $R_{air} = 287.053\ \mathrm{J\ K^{-1}\ kg^{-1}}$.

The cabin pressure is 98882.53 Pa, then the density of air is $\rho_{air} = \frac{98882.53}{287.053 \times 288.71} = 1.193\ \mathrm{kg/m^3}$.The kinematic viscosity of air is (56) $\nu = \rho/\mu$, then $\nu_{air} = 1.50197 \times 10^{-5}\ \mathrm{m^2/s}$.

For the nozzle area with a diameter of 60.325 mm:

$$\mathrm{Re_{inlet}} = \frac{UD}{\nu} = \frac{6.79921 \times 0.060325}{1.50197 \times 10^{-5}} = 27308$$

For the slot area, assuming that there is negligible flowrate longitudinal the average velocity can be computed by dividing the flow rate by the slot area. For the 3 rows cabin used in 3.2.1 the slot longitudinal length is $6049.752 - 3432.85 = 2616.9$ mm, while the slot width is 1.25 inches = 31.75 mm.

There are 2 ways of computing the Reynolds number. Using the hydraulic diameter or the slot width as the characteristic length: $D_h = \frac{4A}{P}$. $D_h = 4 \times \frac{2616.9 \times 31.75 \times 10^{-6}}{2 \times (2616.9 + 31.75) \times 10^{-3}} = 62.74$ mm

The total Q in the 3 rows is $Q_{3rows} = Q_{nozzle} \times 10\ \mathrm{nozzles} = \frac{Q_{total}}{34} \times 10 = \frac{660.73 \times 10}{34} = 194.332\ \mathrm{L/s}$

$$U_{avg\ slot} = \frac{Q_{3\ rows}}{A_{2\ slots}} = \frac{194.332 \times 10^{-3}}{2 \times 2616.9 \times 31.75 \times 10^{-6}} = 1.1694\ \mathrm{m/s}$$

Assuming the same air conditions as before, using the hydraulic diameter,

$$Re_{slot} = \frac{U_{avg\ slot} \times D_h}{\nu_{air}} = \frac{1.1694 \times 62.74 \times 10^{-3}}{1.50197 \times 10^{-5}} = 4885$$

Or using the characteristic length as the slot width:

$$Re_{slot} = \frac{U_{avg\ slot} \times L_{slot}}{\nu_{air}} = 2472$$

In a post processing, the average dynamic viscosities were retrieved from the simulations.

	Kinematic Viscosity (Pa · s)	Characteristic length (mm)	Velocity Magnitude (m/s)	Reynolds
Cabin	1.5713×10^{-5} .		With gasper | no gasper	
Slot	1.5212×10^{-5}	$L_c = L_{width} = 31.75$	1.169 | 0.974	2440 | 2033
Inlet	1.5072×10^{-5}	$L_c = D_{inlet} = 60.325$	6.799 | 6.453	27213 | 25828
Gasper	1.5072×10^{-5}	$L_c = D_{gasper} = 16.841$	7.18305	8026
Injector	1.2070×10^{-5}	$L_c = D_{injector} = 25.4$	0.2654	557

Model	Institute		W (m)	H (m)	L (m)	Rows (Thermal)	Slot Dimensions	Slot Airflow Rate	Resources
Boeing 737	Purdue University	PU-737	1.750	2.200	0.900	H-1 (75W)	20 mm ×900 (MV) + G	9.03 L/s per pax 18.4°C Re(jet)=1927	[37], [38], [39]
	Tianjin University	TJ1-737	3.25	2.150	5.85	7 (75W)	3.5 mm × 50 mm (766 slots 57°) (MV)	9.4L/s per pax 20°C Re(slot)=1277	[40] [41] [42] [43] [44], [45] [46]
	Tianjin University (2021)	TJ2-737	3.530	2.155	5.852	7 (30°C)	40 mm ceiling; 65 mm lower (685 or 750) length (DV)	9.5L/s per pax 22°C Re(jet)=2586	[36] [47], [48]
	Kansas State University	KSU-737	3.4036	2.1336	4.826	5 (100W)	43mm × 3.81m (single slot) (MV)	6.84L/s per pax 10.5°C Re(jet)=3788	[49], [50], [51]
Boeing 767 *Real diffusers	**Kansas State University ***	KSU-767	4.720	2.100	9.578	11 100W	31.75 mm (MV)	8.58L/s per pax, 15.6°C Re(jet)=2358	[52], [53], [54], [51], [55]
	Illinois University *	IU-767	4.700	2.098	4.324	5 (50W)	Assumed same as KSU	8.35L/s per pax, 7.2°C Re(jet)=2416	[56], [57], [58], [59], [60], [61], [62], [63]
	Technical University of Denmark *	DTU-767	4.900	2.096	3.200	3 (60W)	Assumed same as KSU	9.52L/s per pax, 21.5°C Re(jet)=2056	[64], [65], [66], [67]
	Purdue University	PU-767	4.900	2.100	4.320	4 (83W)	25 mm (MV)	8.21L/s per pax, 19.3°C Re(jet)=1823	[68], [69], [70]
	Dalian University of Technology	DUT-767	4.600	2.100	5.920	7 (75W)	25.4 mm width (MV); DV; PV	10L/s per pax, 19.5°C Re(jet)=2698	[71]; [17]
Boeing 767 scaled	Purdue University	PU-767s	0.451	0.2255	2.4384	30			[72],[73]
Boeing 777	Syracuse University	SU-777	3.000	2.470	2.000	H-2	92 × 470 (MV+PV) 254×470 outlet		[74]
Boeing 747	Aircraft Environment Research Facility in CAMI	AERF-747	6.500	2.410	56.4	All			[75]. [76]
Airbus 310	FTF at Fraunhofer Institute	FTF-310	*5.287*	*2.330*	*N/A*				[77], [78], [79]
Airbus 320	German Aerospace Center (DLR)	DLR-320	*3.630*	*2.130*	*N/A*	11			[80], [81]
	Chongqing University	CU-320	4.000	2.350	4.850	3			[82], [83], [83].
Airbus 380	German Aerospace Center (DLR)	DLR-380	5.100	2.200	6.000	5	50 mm × 3430 mm		[84]
A380 section	German Aerospace Center (DLR)	DLR-380s	2.000	1.350	3.430		22 mm × 3 mm (per slot)		[85], [86]
MD-82	Tianjin University	TJ-MD82	2.910	3.280	2.040		53 mm / 26.5 mm (width)		[87], [88], [89], [90], [91]
Half Generic	Kansas State University	KSU-GEN	2.134	2.134	2.134	H			[92], [93], [94], [95], [96]
			Other installations (new or owned by manufacturer)						
Generic	Flexible Cabin Laboratory at CATR	CATR-FCL							[97]
Boeing 737	Fuselage Laboratory at CATR	CATR-FL							[97]
Boeing 787	Boeing Company	AIC-B787							[99]
Airbus 340	Airbus Company	A340							[72], [100]
Generic	Modulares Kabinen Mock-Up Göttingen in (DLR)	DLR-MKG	6.25	2.7	9.96	10			[98]
H-Half; AIC – Aircraft Integration Center. FTF – Flight Test Facility. CAMI – Civil Aerospace Medical Institute									

Table 32. Facilities with different aircraft cabin mock-up including details.